Variations in Iceland-Scotland Overflow Water during the Penultimate Interglacial

by

Jamie Dianne Taylor

Master's thesis in geology
Concentration: Marine geology and paleoclimatology

Department of Earth Science

University of Bergen

December 2018

ABSTRACT

There is a growing body of evidence suggesting that the density and speed of the Nordic Seas overflows experienced significant changes on both centennial and multi-millennial time scales throughout the penultimate interglacial period. However, the exact nature and magnitude of this variability remains poorly constrained. Iceland-Scotland Overflow Water (ISOW), which constitutes the eastern branch of the overflows, forms as a result of the cooling and subsequent sinking of salty, near-surface waters in the Nordic Seas. This cold, dense water mass flows southward as a deep boundary current forming the lower limb of the Atlantic Meridional Overturning Circulation (AMOC). It is balanced by the inflow of warm, salty surface waters originating in the tropics. Climate models forecast significant decreases in AMOC by the end of the century due to changes in evaporation and precipitation patterns in a warmer climate. These projections suggest a strong sensitivity of deep water currents to warming or freshening, but have large uncertainties. Thus, it is unclear how sensitive ocean circulation is to potential future changes. Information about ocean circulation in the past provides real world constraints for understanding ocean sensitivity to warmer-than-present conditions.

Here I reconstruct relative changes in the near-bottom flow strength of ISOW using mean sortable silt ($\overline{SS}$) from a high sedimentation rate site (53°03.40'N, 33°31.78'W; water depth 3024 m), which is located under the direct path of ISOW on the extreme southern end of the Gardar Drift. I pair this new high-resolution sedimentological record with existing geochemical data ($\delta^{13}C$) for Site U1304 in order to test the hypothesis that overturning circulation experienced significant, rapid changes during the peak of the last interglacial (LIG) (128-116 kyr BP). My $\overline{SS}$ results demonstrate significant millennial scale flow variability throughout the LIG, with a persistent pattern of abrupt, centennial scale variability superimposed over the longer-term trends. The transient, centennial scale oscillations experience maximum magnitude variability during the period of highest flow speed, suggesting that the main axis of ISOW was proximal to the site at this time. Compared to $\overline{SS}$, $\delta^{13}C$ shows persistent, centennial scale variability superimposed over relatively stable and high values. This long-term stability in bottom water chemistry suggests that ISOW remained the dominant water mass over the site in spite of the significant variability in flow vigor that occurred throughout the LIG. The clearest feature in the LIG bottom flow record is a gradual acceleration starting at ~124 kyr BP followed by an abrupt deceleration at ~120 kyr BP. This trend is broadly consistent in both timing and magnitude to similar trends observed at nearby sites, and have been postulated to be linked to increases (acceleration) and decreases (deceleration) in convection intensity. Taken together, my observations confirm the notion that LIG deep circulation varied significantly on millennial time-scales, and reveal that circulation also oscillated on shorter (centennial) timescales. Circulation variability through a period of warmer-than-present climate confirms model results suggesting that the deepest branches of AMOC remain sensitive to buoyancy changes in Nordic Seas source regions in a warm(er) climate.

ACKNOWLEDGEMENTS

I would like to express my sincere gratitude to my advisors without whose direction and support this project wouldn't have been possible. To Dr. Ulysses Ninnemann, thank you for your insight and patient guidance back to the point when I went astray. To Dr. Eirik Galaasen, thank you for sharing your time and experience in the lab. And thank you most especially for doing all the wet sieving so I didn't have to. And to finally, to Dr. Helga (Kikki) Kleiven, thank you for that final read through, and for sparing me the mortification of all those misspelled names.

I would also like to take moment to acknowledge the love and support of my family. To my children who had to learn to fold their own laundry while I learned to cook silica out of mud. Thank you for your patience. I'm still very sorry for all the frozen pizza nights. To my husband who said nine years ago, "Of course it's not too late. Go back and do it now." Thank you for always pushing me forward, in spite of my very strong instinct to stand still. And a very special thanks to my husband's left eye for exploding when it did. Those extra three weeks made all the difference in the world. And finally, to my mother who came an awful long way to keep my ovens clean. Thank you for doing it first, for showing me that it really is possible to be a mom and student at the same time. I hope I've been half the role model to my girls that you were to me.

Jamie Dianne Taylor
Halhjem, December 11, 2018

Table of Contents

1. INTRODUCTION

This thesis project was undertaken as an integral part of the Thresholds for destabilizing thermohaline circulation and ocean carbon cycling in a warmer world (THRESHOLDS) project. It was supervised by Professor Dr. Ulysses S. Ninnemann, from the Department of Earth Science and the Bjerknes Center for Climate Research (BCCR) at the University of Bergen (UoB), and co-supervised by Researcher Dr. Eirik Galaasen, and Associate Professor Dr. Helga (Kikki) Kleiven, also from the Department of Earth Science and BCCR at UoB.

1.1 THRESHOLDS Project

THRESHOLDS is an international, multidisciplinary research project which has as its primary goal to constrain the natural variability of thermohaline circulation (THC) under warm climate conditions. Using both sediment archives and modeling tools, project participants are seeking answers to such fundamental question as:

- How stable is North Atlantic Deep Water (NADW) formation during warm climate states?
- Do large centennial-scale anomalies in deep ocean chemistry and circulation occur during interglacial conditions?
- What is the relationship between climate and deep ocean carbon cycle anomalies? And what boundary conditions or forcing mechanisms trigger them?
- And, to what extent can past THC variability be used to understand and predict future THC behavior?

The results of my thesis research will contribute to the THRESHOLDS project by adding to the growing body of proxy data needed to constrain the natural variability of individual components of NADW (in this case, Iceland-Scotland Overflow Water), and to determine the role these separate components play in ocean overturning stability in a warm climate.

1.2 Motivation and objectives

Although the current (interglacial) mode of ocean circulation is seemingly stable on millennial timescales, recent analysis of high-resolution proxy records has uncovered large, centennial- to decadal-scale reductions in circulation, with significant reorganizations of oceanic carbon distribution ($\delta^{13}C$), punctuating an otherwise stable, vigorous style of interglacial overturning.

Prominent disruptions in interglacial circulation have been found in the early part of the current interglacial (Ellison et al., 2006; Kleiven et al., 2008), and during the early and late part of the last interglacial (Oppo et al. 1997, 2006; Hodell et al. 2009; Sanchez Goni et al., 2012; Galaasen et al. 2014). These large fluctuations are associated in the sediment record with increased meltwater flux and ice rafted debris suggesting a strong NADW sensitivity to freshwater flux from melting and/or calving ice sheets. However, smaller, more rapid disruptions are also evident throughout the warmest intervals of the interglacial records, hinting at the possibility that North Atlantic convection is fundamentally more unstable in a warm climate state than previously thought (Irvalı et al., 2016). Delimiting this natural variability of NADW formation in an interglacial climate is a critical first step to constraining, and ultimately predicting the system's possible response to future warming.

The last interglacial (LIG) period (132-115 kyr BP) corresponds to Marine Isotope Stage (MIS) 5e in marine sediment cores (Shackleton, et al. 2002; 2003). In terrestrial ice records, the LIG equates roughly to the Eemian interglacial, although palynological analysis on Mediterranean tree pollen found in marine sediments has revealed the base of the Eemian (~126 kyr BP) to be considerably younger than the base of MIS 5e (Shackleton et al., 2003). Marine isotopic stages and substages were originally identified based on variations in benthic foraminiferal $\delta^{18}O$ values. Thus, the LIG maximum (128-116 kyr BP) is defined as the period of lowest benthic $\delta^{18}O$, and corresponds to the interglacial sea-level high stand. The LIG is frequently targeted and studied as a plausible analogue for the future climate state under anthropogenic radiative forcing because it was the last time in Earth's history that average global temperatures were 2-3°C warmer than today and sea level was between 6 to 9 m higher due, in part, to reduced Greenland Ice Sheet volume (Otto-Bliesner et al., 2006).

The specific aim of my thesis is to test the hypothesis that overturning circulation experienced rapid changes during the peak of the last interglacial period (128-116 kyr BP). To do this, I will generate a high-resolution, mean sortable silt ($\overline{SS}$) record of the interval spanning MIS 5e from the International Ocean Discovery Program (IODP) core Site U1304. This site monitors downstream, deep water outflow from the eastern branch of the Nordic Seas overflows (Fig 3.1) where known high sedimentation rates facilitate the reconstruction of a high-resolution paleoclimate records (Hodell et al., 2009). Sortable silt is defined as that fraction (10-63μm) of the terrigenous grains in a marine sediment deposit whose differential, down core size can be

attributed to the fluctuating speed of the depositing current (McCave et al., 1995; McCave, 2008). Thus the $\overline{SS}$ record I produce should reflect temporal variations in the relative speed of the deep boundary current over the core site. I will also pair my new $\overline{SS}$ record with existing geochemical data from the same core (Hodell et al., 2009) in order to present a new multi-proxy record that will further constrain flow speed changes over the site with details of concurrent water mass variability. Because observed changes in flow speed at a given site could reflect variations in both the speed of the depositing current and/or the relative depth of the current (Thornally et al. 2013a), it would be difficult to draw reliable conclusions from a single $\overline{SS}$ record. Therefore, as part of my discussion, I will also compare my $\overline{SS}$ record to similar $\overline{SS}$ records from nearby sites, as well as to complementary geochemical and climate proxies (primarily $\delta^{13}C$ and IRD) available in the published literature. In this way, I hope to provide a more detailed understanding of the temporal and spatial evolution of bottom flow over Site U1304, and in the northeastern North Atlantic generally, during the LIG.

2. BACKGROUND

Any investigation into the relative stability of deep water formation in the past must begin with a discussion of the processes and mechanisms driving modern modes of ocean circulation and deep water formation. To that end, in this chapter I will present an overview of global overturning circulation: what it encompasses, what maintains it, and what conditions threaten or disturb its stability. I will also briefly summarize the current consensus regarding the role of these processes in shaping MIS 5e climate evolution.

2.1 Global overturning circulation

Global ocean circulation has been colloquially described as a 'Great Conveyor Belt' (Broecker, 1991) which constantly moves and mixes warm, surface water from the Pacific Ocean, through the Indian Ocean, then into the Atlantic Ocean where it eventually cools and sinks, returning to the Pacific Ocean as a cold, bottom current via the deep Atlantic and Antarctic interior basins (Fig. 2.1). One full circuit of this conveyor belt takes approximately 1000 years (Rahmstorf, 2002; 2006). This conceptual model of ocean circulation is, of course, highly over-simplified. In reality, global ocean circulation is a complex network of interconnected gyres and overturning cells whose locations and geometries are determined not only by geographical features such as the positions of the continents, the shape and orientation of the ocean basins, and the presence of significant bathymetric features such as mid-ocean ridges and overflows sills (see Chapter 3). But also, by the distribution and magnitude of the pressure and temperature gradients that set water masses in motion. Nevertheless, the conveyor belt model persists because it is a useful tool for visualizing the two most fundamental aspects of modern ocean circulation. Namely, the aforementioned warm surface currents moving generally towards the deep-water formation regions in the Atlantic high latitudes, and the cold, deep return currents carrying newly ventilated water back to the Pacific basin at depth.

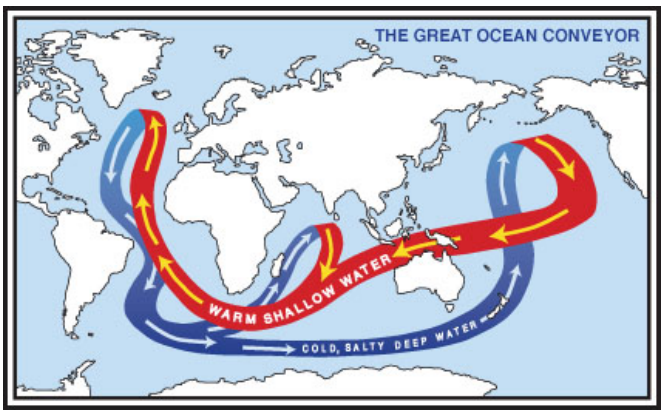

Figure 2.1. Highly simplified cartoon illustrating the Great Ocean Conveyor. Warm surface currents (red) carry water to the Atlantic where it cools and sinks, then returns to the Pacific at depth (blue) (Adapted from Broecker, 1991).

This conveyor-like pattern of circulation is more formally referred to in the literature by several closely related, but not precisely interchangeable names. Meridional Overturning Circulation (MOC) describes the north-south volume transport of water masses as a function of depth and latitude (Delworth, 2008). MOC is often depicted as a zonally integrated streamfunction with a core of maximum velocity flow moving meridionally at intermediate depths, while near-surface and bottom water masses move in the opposite direction above and below this core (e.g. Fig 2.2). Atlantic Meridional Overturning Circulation (AMOC) refers to circulation within the Atlantic Basin specifically, but the terms AMOC and MOC are often used interchangeably and generally to refer to circulation in the meridional, vertical plane. AMOC consists of two primary branches: a north flowing surface branch which carries warm, saline waters towards the poles in the upper 500 m of the ocean, and a south-flowing deep branch which conducts cold, dense water back to the lower latitudes. It is this southward flowing deep-water mass that is known as North Atlantic Deep Water (NADW). In the modern ocean, its maximum flow is concentrated at about 2500 m depth (Dickson & Brown, 1994; Delworth et al., 2008).

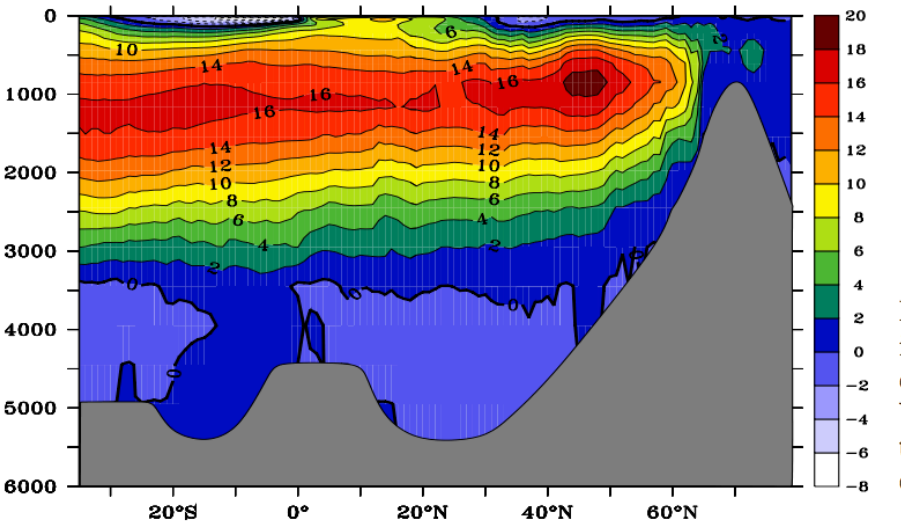

Figure 2.2. Example of modern MOC streamfunction in Sverdrup (1 Sv = 10^6 m^3/s) in the Atlantic. The NADW cell is clearly visible centered between 1000-3500 m depth. The surface layer in the upper 500 m and the near bottom layer of Antarctic Bottom Water move in the opposite direction highlighting the fundamental pattern of ocean circulation (Adapted by Rahmstorf 2006 based on data collected by Köhl et al. 2006).

AMOC and MOC are descriptive terms that do not infer any information about the driving forces behind ocean circulation. The complementary term Thermohaline Circulation (THC), on the other hand, does imply a specific driving mechanism. THC describes buoyancy driven circulation which arises from the advection of heat and salt to the high latitudes via surface currents, and their subsequent sinking into the interior ocean when surface waters become colder and denser than the underlying water mass (Rahmstorf, 2006). The sinking water mass

creates a vertical pressure gradient which pushes bottom water ahead of it, and pulls surface water in to fill the void behind it, thus initiating an overturning circulation cell. It has been observed, however, that sustained THC requires more than just a source of cold, dense sinking water. Steady-state, deep circulation requires some process or processes which can supply the system with the energy needed to maintain circulation against inevitable dissipation (Kuhlbrodt et al., 2007; Delworth et al., 2008). Two such processes have been suggested: the turbulent mixing of heat into the abyssal ocean, and wind-driven upwelling in the Southern Ocean. Figure 2.3 summarizes the key components of AMOC and its driving mechanisms.

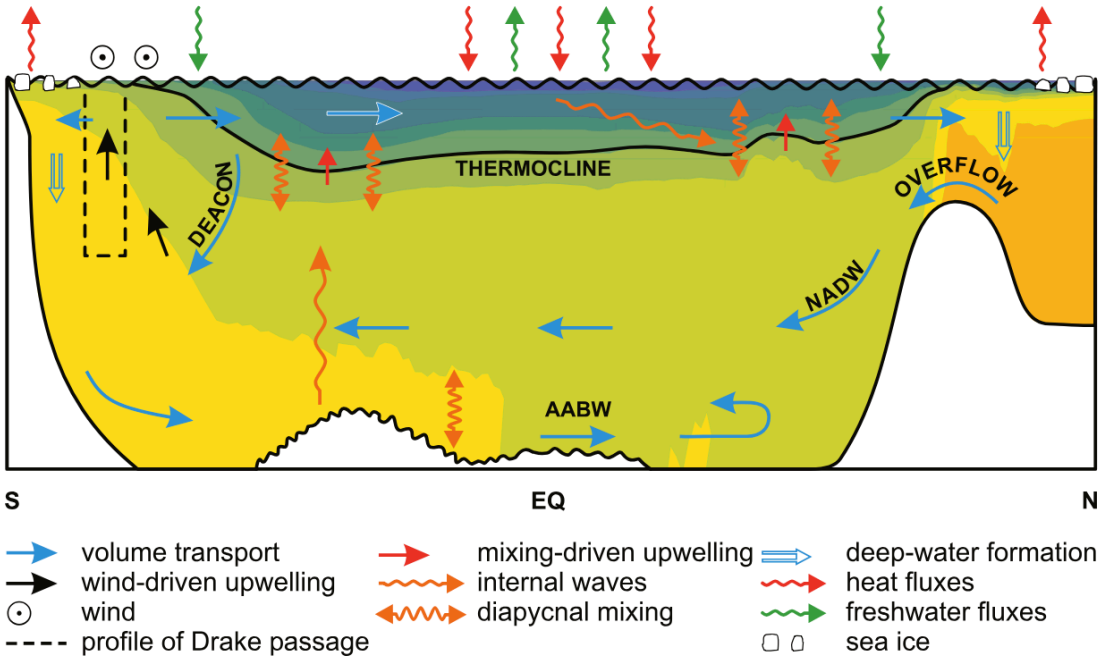

Figure 2.3. Idealized meridional profile of the Atlantic basin summarizing the primary components driving AMOC (blue arrows). The color shading indicates averaged density profiles with the highest densities (orange) centered under high latitude, deep water formation regions in both hemispheres, and the lightest densities (blue) contained in the warm surface layer. Dense water from the high latitudes displace warmer, lighter abyssal water (green) as it sinks and moves equatorward. Overturning circulation is maintained by diffusive heat transfer in the mid- and low-latitudes (orange wavy arrows) which warms abyssal water promoting slow upwelling, and by strong westerly winds in the Southern Ocean causing Ekman divergence and deep upwelling (black arrows) into the Antarctic Circumpolar Current (dashed lines) (Kuhlbrodt et al., 2007).

Mixing Energy

In a series of classic tank experiments conducted in 1908, Johan Sandström showed that in order for the newly formed deep water to always be denser than the water already filling the abyssal ocean, some mechanism must be working to constantly reduce the density of bottom water. Otherwise the entire basin would eventually fill with cold, dense water and circulation would simply stop (Kuhlbrodt et al., 2007). Sandström's Theorem suggests that the slow

diffusion of heat through turbulent mixing of the ocean's interior is the mechanism that steadily reduces the density of deep waters such that they can rise and continually be replaced by colder, denser water from above. The ultimate energy source for this turbulent mixing comes from the acceleration of water by winds and tidal forces which generate internal waves. The small-scale turbulence produced as these internal waves dissipate, mixes heat downward into the deep ocean (Rahmstorf, 2006; Kulbrodt et al., 2007). Abyssal waters warmed in this way gradually gain enough buoyancy to expand, and rise to the surface to replace dense, sinking waters.

Wind-driven Energy

The second mechanism driving sustained overturning circulation ultimately arises from wind-driven Ekman divergence in the Southern Ocean. Because there are no meridional obstacles in the bathymetry surrounding Antarctica (Kuhlbrodt et al. 2007), Southern Ocean waters flow in a strong, deep, east flowing current—the Antarctic Circumpolar Current (ACC)—which encircles the entire continent without any deflecting gyres or western boundary currents as are common in other ocean basins (Chapter 3.3). Due to the rotation of the Earth, wind stress causes a net northward volume transport of surface water below 50°S (i.e. Ekman transport) (Delworth et al., 2008). Ordinarily, shallow waters would fill the void left behind by the northward flowing Ekman layer, but because there are no gyres in the Southern Ocean, the compensating inflows come from deeper meridional flowing waters drawn from below the sill depth of the Drake Passage (~2500 m). Since the cold, dense south-flowing branch of AMOC is centered at about this depth (Fig. 2.1.2), the compensating inflow is drawn from there. Thus, an interhemispheric meridional overturning loop is closed by the sinking of dense water in the high northern latitudes, which is pumped southward over the equator, and upwelled into the ACC where it rapidly cools and sinks again, flowing northward either as Antarctic Bottom Water (AABW) or Antarctic Intermediate Water (AAIW).

The distinction between the two driving processes (mixing vs. wind-driven) is important because they imply different sensitivities to changes in surface forcing (Kuhlbrodt et al. 2007). Wind-driven upwelling, for example, would be particularly sensitive to changes in the strength and/or position of the westerly wind-belt surrounding Antarctica. A strongly stratified water column, on the other hand, would require more turbulent energy to mix heat across density gradients in order to promote buoyancy in the abyssal ocean, and thereby maintain vigorous circulation. In either case, these processes are only valid in describing long-term ocean

circulation. Because of the intermittent nature of convection events (next section), buoyancy losses at the ocean's surface versus buoyancy gain in the ocean interior take multiple millennia to reach steady-state equilibrium. The convection perturbations that are the focus of this thesis are short-lived and do not necessarily disturb this broader equilibrium. But they nonetheless have important consequences for interior ventilation and chemical distribution within the water masses.

2.2 The significance of deep water formation to AMOC strength

The upwelling processes discussed above have one critical feature in common: high latitude deep water formation. The poleward advection of heat and salt, and the subsequent conversion of warm, salty surface water into cold, dense deep water initiates overturning circulation, while turbulent mixing and wind-driven upwelling work to maintain it. It is important to note, however, that it is the magnitude of the surface buoyancy fluxes—that is, the scale of the density gradient between the surface and deep water masses—that determines the depth, extent, and vigor of the overturning cell (Kuhlbrodt et al., 2007; Delworth et al., 2008). For this reason, the significance of the surface conditions in the deep water formation regions to overall AMOC vigor cannot be over stated.

Deep water formation occurs by a number of processes including open ocean convection, intense deepening of the winter mixed layer, and brine rejection during ice formation over shallow shelf regions (Kuhlbrodt et al. 2007). In the modern ocean, the conditions necessary for vigorous deep water formation to occur only exist in a handful of locations in the Atlantic high latitudes (Fig. 2.4). The specific conditions required are high surface salinity, and weak stratification due to intense wintertime heat loss to the atmosphere (Marshall & Schott, 1999). There is some evidence that in the recent geologic past that deep convection occurred in the North Pacific. Currently, however, salinity levels are too low in the Pacific basin for surface waters to densify enough to sink below the main thermocline (Broecker, 1991; Clark et al. 2002).

Open ocean deep convection has been observed in the Labrador and Greenland Seas (Marshall & Schott, 1999). Open ocean convection occurs when a large area of surface water (50-100 km^2) is 'preconditioned' in the early winter season; stratification begins to erode and buoyancy is lost due to heat exchange with the atmosphere. An actual convection event occurs when a

strong winter storm system causes rapid, intense local heat loss, and a localized plume or 'chimney' within the preconditioned area violently mixes downward. These convecting plumes can reach depths of 2000-3000 m and are generally less than 1 km wide (Marshall & Schott, 1999). In the Labrador Sea, open ocean convection events are intermittent, showing strong interannual to decadal variability in frequency and vigor. In addition, they appear to be particularly sensitive to enhanced freshwater forcing due to Greenland Ice Sheet melt. One model study concluded that the loss or reduction of convection in the Labrador Sea due to enhanced freshwater supply could reduce overall AMOC strength by as much as 30% (Yu et al., 2016). Open ocean convection in the Greenland Sea, on the other hand, results in deep water too deep to overflow the sills along the Greenland-Scotland Ridge (GSR) (see Chapter 3.2), so variability in convection in this region is expected to have a smaller impact on AMOC (Aagaard et al., 1985; Delworth et al., 2008).

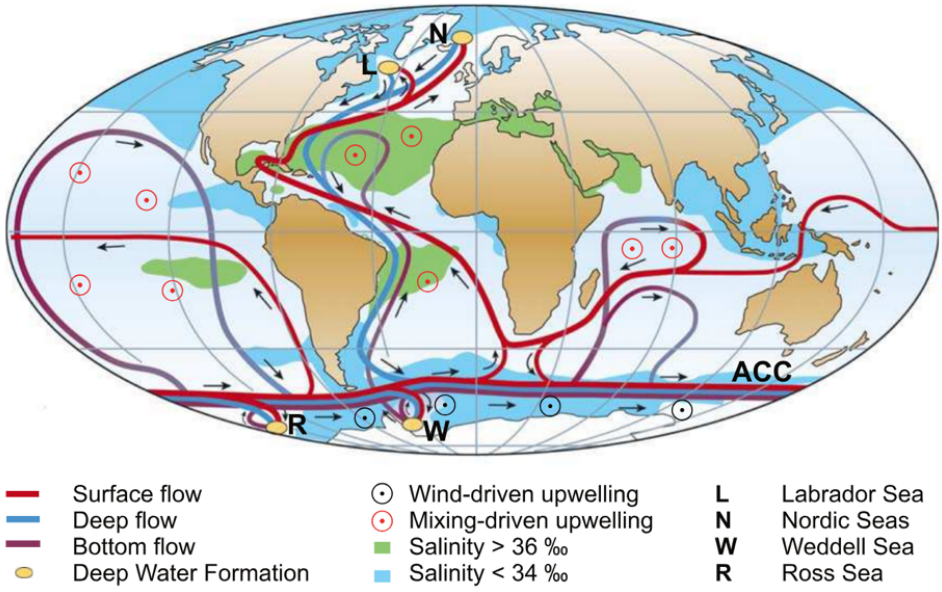

Figure 2.4. A simplified illustration of global overturning circulation highlighting areas of mixing-driven vs. wind-driven upwelling (red and black circles), as well as deep water formation regions (yellow ovals). In the Atlantic, surface waters flow through highly saline waters in the subtropics where evaporation is greater than precipitation (green), and sink when they reach the Nordic and Labrador Seas. There are no such high saline waters in the Pacific, and so no corresponding convection regions in the North Pacific where surface waters become cold and dense enough to sink (Rahmstorf, 2002).

In the Nordic Seas, the depth of the sills along the GSR lie between ~400-800 m below sea level (mbsl) (Fig. 3.2), therefore buoyancy loss down to this depth is sufficient for dense waters to overflow the sills and join the AMOC circuit (Kuhlbrodt et al., 2007). Such intermediate waters are formed by turbulent deepening of the winter mixed layer. A process which occurs

regularly in the region due to strong heat loss of highly saline Atlantic inflow waters. Convection in the Southern Ocean, on the other hand, occurs mainly over the Antarctic continental shelf in the Weddell and Ross Seas (Fig 2.4). Wintertime sea ice formation and brine rejection leaves a dense, super-saline layer of surface water, and polynyas (large, open patches in the sea ice) allow for intense heat loss out of this layer. The resulting mass of extremely cold, dense water (AABW) flows down the continental slope, entraining significant amounts of ambient water as it goes, and fills the abyssal Atlantic below NADW.

2.2.1 Freshwater forcing and AMOC bistability

Freshwater fluxes play a critical role in the stability of high latitude convection regimes. The primary reason for this is the relatively low impact that thermal expansion has on seawater stratification at low temperatures. In the equation of state, an analytical tool used to calculate seawater density as a function of salinity, temperature, and pressure ($\rho = \rho\ (T, S, p)$), the ratio of coefficients describing salinity and temperature is about 30:1 for seawater at 0°C, and 10:1 for seawater at +2°C (Aagaard and Carmack, 1989). Thus, the haline coefficient is so dominant that even small additional fluxes of freshwater will have a large impact on density stratification and the water column's ability to convectively overturn. While temperature variability, even below freezing, will have little effect.

Furthermore, THC is a fundamentally non-linear system which can be characterized by a simple positive feedback: the salt advection feedback, whereby the addition of anomalous freshwater fluxes can have drastic consequences for continued circulation. There is a net surplus of freshwater in the Arctic due to excess run-off and precipitation relative to evaporation at high latitudes (Kuhlbrodt et al., 2007). Under steady-state conditions, this freshwater is compensated for by the influx of highly saline surface waters which have experienced excess evaporation in the tropics and sub-tropics. This northward advection of salt keeps surface waters in the subpolar deep water formation region relatively dense and salty despite high fluxes of freshwater from the hydrologic cycle (net precipitation). Highly saline waters enhance vigorous convection of deep water masses, which, in turn, pulls more saline surface waters north to replace sinking water masses. Thus, convection itself is a key aspect to overturning stability. As long as convection is robust, the incoming freshwater will be continuously mixed with more saline waters, and prevented from pooling at the surface. In this way, surface density is kept high enough to allow for continuous overturning. However, if an anomalous flux of excess

freshwater stabilizes the water column, and too much time passes between convection events, surface waters will grow fresher and fresher until, even at increasingly colder temperatures, they can no longer lose enough buoyancy to sink, effectively halting overturning circulation.

This sensitivity to freshwater in the system leads to a theorized bistability of circulation under current climate conditions (Rahmstorf, 2006; Kohlbrodt et al., 2007). Bistability was first described by Stommel (1961), and has since been reproduced and confirmed by multiple climate models, and is thus considered by climate modelers to be a robust feature of THC. Figure 2.5 shows a schematic stability diagram which features the two stable equilibrium states of THC. There is essentially an "on" and an "off" state. That is, equilibrium with and without active overturning circulation.

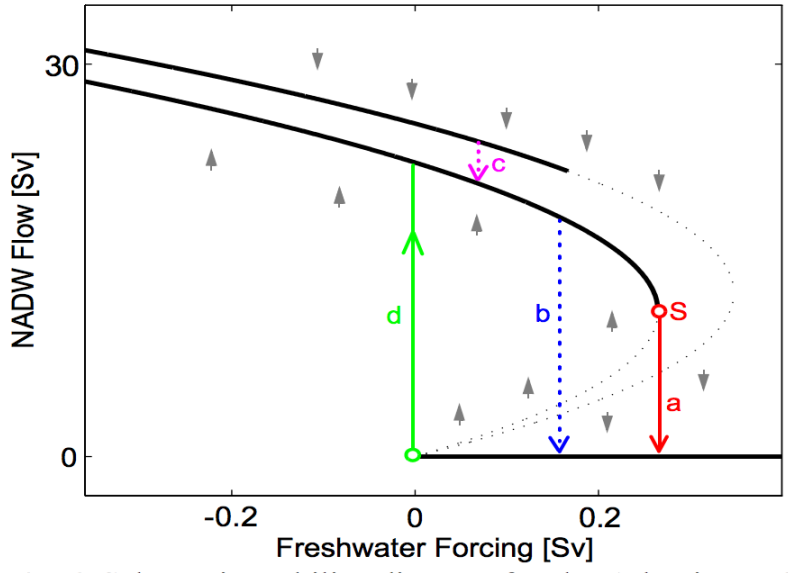

Figure 2.5. Schematic stability diagram showing stable equilibrium states for AMOC in the current climate. See text for description (Kuhlbrodt et al. 2007; adapted from Rahmstorf, 2006).

In the diagram (Fig. 2.5), the strength of overturning circulation (NADW flow) is a function of freshwater flux into the system. The solid black lines indicate the stable equilibrium states. There are two lines showing the system in equilibrium with NADW "on" because the curve has been calculated to show active convection in more than one location. Transition (c) indicates that switches between convection locations are possible. Point S is the critical threshold at which the flux of freshwater is great enough to turn NADW formation to the "off" position, and the equilibrium state switches. The three other possible transitions seen in the diagram are, (a) an advective spindown when salt transport ceases after overturning stops, (b) a polar halocline

catastrophe scenario where a massive influx caps the convection location with a freshwater lid which abruptly halts overturning, and (d) the re-activation of convection after the freshwater forcing has stopped and salinity has returned to normal.

In summary, the cooling of water masses at high latitudes, and the input of freshwater from the hydrological cycle have opposing effects on the density structure of the water column. Cold temperatures are central to the densification of saline surface waters, while unusual fluxes of freshwater decrease salinity, drastically increase buoyancy, and hamper deep convection. Thus, salinity is the crucial factor and primary cause of nonlinear behavior of THC, and anomalous influxes of freshwater appear to be the triggers that switch THC from its "on" to its "off" mode.

So far, this chapter has focused on processes which govern long-term, orbital-scale ocean stability and steady-state equilibrium circulation. However, the particular focus of this thesis is on more transient convection anomalies that occurred within the broader context of a seemingly stable interglacial (warm) climate. For that reason, I turn the focus now to what is currently known about centennial- to decadal-scale AMOC variability and its relation to abrupt climate change.

2.3 AMOC and abrupt climate change

The world ocean is a crucial component of the climate system. Its vast heat capacity and circulation system allow solar energy to be absorbed in the lower latitudes where radiation is strongest, and then be redistributed to high latitude regions where solar radiation is relatively weak. For example, it has been calculated that 1.3 ± 0.1 PW (1 PW = 10^{15} W) of latent heat are transferred poleward in the Atlantic by tropical and subtropical surface currents, and released to the atmosphere over the subpolar ocean mostly in the form of water vapor (Rahmstorf, 2002). This process raises the average air temperature of coastal regions in the North Atlantic by as much as 10°C relative to inland regions of the same latitude. In addition to this temperature moderating effect of heat redistribution, the ocean further influences the Earth's energy budget through its sea-ice cover (albedo effects) and through its long-term storage of carbon (i.e. the so-called 'biological pump'). However, since a comprehensive examination of the ocean's overall place in the climate system is beyond the scope of this thesis, I will elaborate here only on the apparent role of overturning circulation in modulating abrupt climate change.

In order to reconstruct past ocean circulation, paleoceanographers rely primarily on the marine sediment archive and the various biogeochemical and physical proxies preserved there. Reconstructing abrupt climate events from deep marine sediments is particularly challenging because low abyssal sedimentation rates, bioturbation, and the difficulty of accurate dating, easily mask high frequency variability of the climate signal. However, by focusing research and coring efforts on areas like the Eirik and Gardar Drifts (Fig 3.1) which have high sedimentation rates and monitor crucial, deep return flows, researchers have had increasing success at resolving AMOC variability down to the centennial or even decadal (Boessenkool et al., 2007; Mjell et al., 2015; 2016) timescales.

Decades of research and multiple time slice compilations of independent marine and ice core proxies have established a prevailing paradigm of overturning circulation which holds that at different times AMOC has existed in three different steady-state circulation modes (Rahmstorf, 2002; Kuhlbrodt et al., 2007; Lynch-Stieglitz, 2017). These three modes: a warm (interstadial) circulation mode, a cold (stadial) circulation mode, and an off (Heinrich) circulation mode, are schematically illustrated in Figure 2.6. The warm circulation mode (Fig. 2.6a) is characterized by the modern state of ocean circulation with vigorous deep water formation in the Nordic and Labrador Seas, and a strong, deep AMOC return branch filling the deep North Atlantic down to ~3500 m depth. The cold circulation mode (Fig. 2.6b) is most typified by conditions during the last glacial maximum (LGM) when the location of deep water formation appears to have shifted south of the GSR into the Icelandic basin (Oppo & Lehman, 1993) causing the return branch of AMOC to shoal to ~2000 m depth, thus allowing southern sourced waters (SSW) to reach further north and fill the abyssal North Atlantic. The off mode (Fig. 2.6c), as implied by the earlier discussion of AMOC bistability (Fig. 2.5), is triggered by anomalously large inputs of freshwater delivered to the North Atlantic during Heinrich events. While in the off mode, deep water formation effectively ceases, and the abyssal North Atlantic fills with SSW. Although true ocean circulation at any given time is likely to be considerably more nuanced than this conceptual model can capture, it does provide a useful frame work in which to contextualize our understanding of the relationship between abrupt climate change and AMOC variability.

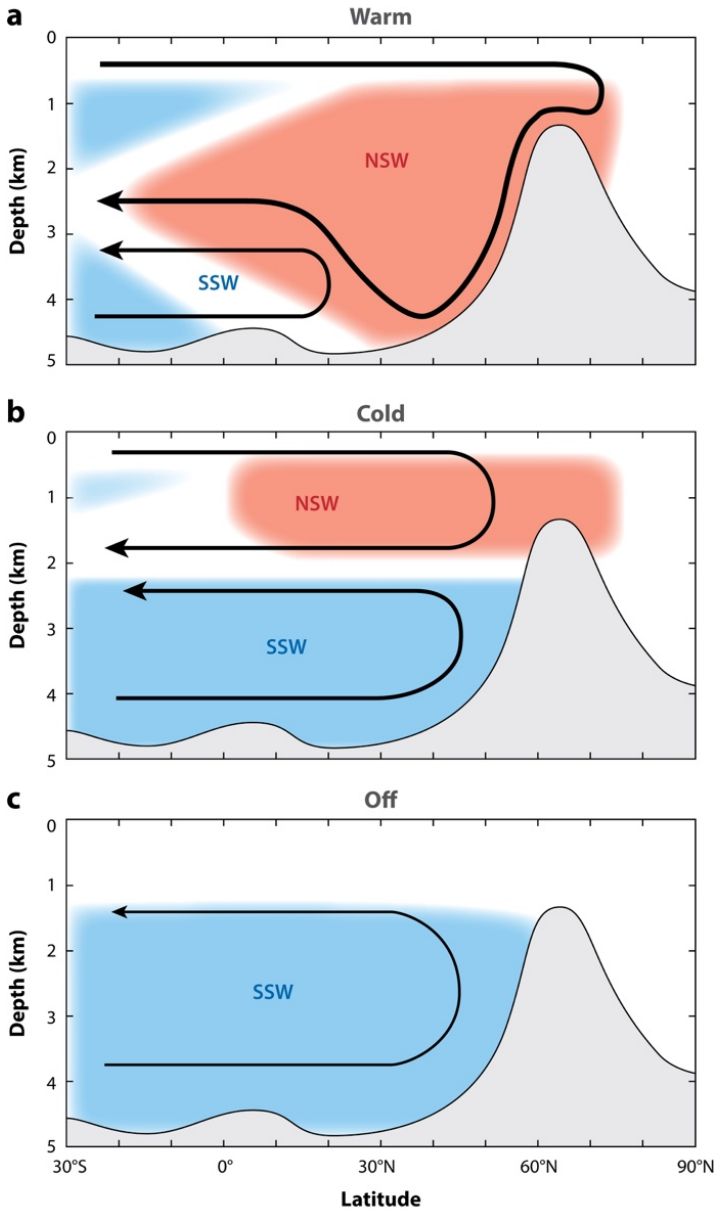

Figure 2.6. Conceptual model of overturning circulation in (a) the warm circulation mode, (b) the cold circulation mode, and (c) the off mode. The extent of northern sourced water masses (NSW) is shown in red. The extent of southern sourced water mass (SSW) is shown in blue. See text for further details (Lynch-Stieglitz, 2017).

Dansgaard-Oeschger Events

The most prominent features of glacial/interglacial climate variability are Dansgaard-Oeschger (D-O) events. These quasi-periodic warming events dominate the climate record for at least the past 120 kyr, and were identified from stable oxygen isotope studies of Greenland ice cores. D-O events are defined as a dramatic 5-10°C rise in atmospheric temperatures into an interstadial phase (Rahmstorf, 2002; 2006). This rapid warming occurs within, at most, a few decades, and is followed by a gradual, step-down cooling trend lasting several centuries. The D-O event ends with a final, rapid temperature drop into a stadial phase (e.g. Fig. 2.7). Synchronous, similarly

structured variability is observed in independent proxy records from all over the world, strongly suggesting that the D-O signal is global climate phenomenon (Clark et al., 2002).

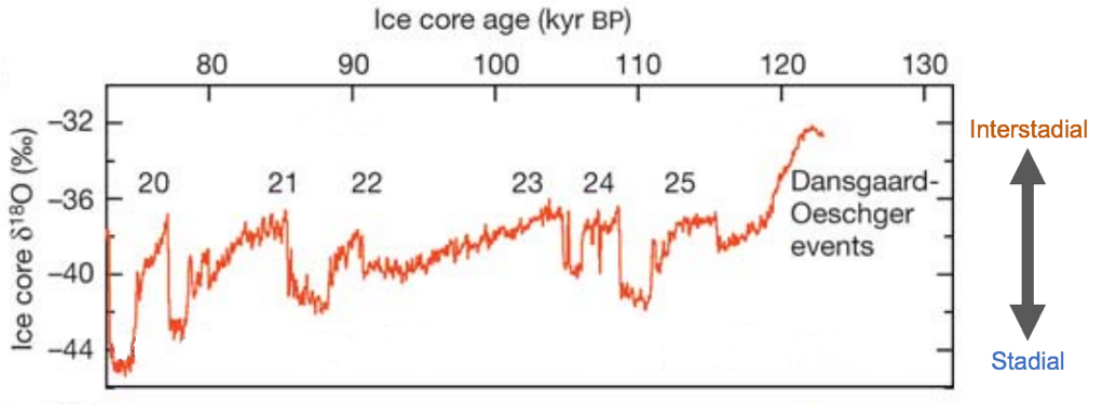

Figure 2.7. Stable oxygen isotope ($\delta^{18}O_{ice}$) record from North Greenland Ice Core Project (NGRIP) showing D-O events 20 through 25 dating from between ~85-115 kyr BP (Modified from NGRIP members, 2004).

The exact mechanism behind D-O paced climate change is not fully understood, but the most commonly proposed explanations invoke changes in AMOC. Specifically, the previously mentioned latitude shifts in the location of deep water formation between the Irminger (stadial phase) and Nordic (interstadial phase) Seas (Rahmstorf, 2002). This hypothesis would explain many of the features of the global D-O signal including the 'bipolar see-saw' effect, in which there is an anti-phasing of warming and cooling in the Northern and Southern Hemispheres during a D-O event (EPICA community members, 2006). In the warm interstadial phase, when vigorous deep water formation occurs in the Nordic Seas, a great deal of heat is transported north across the equator and released into the subpolar and polar North Atlantic, thus promoting cooling in the Southern Hemisphere concurrent with warming in the Northern Hemisphere. During a cold stadial phase, on the other hand, the proposed shift in the location of deep water formation into the Irminger Sea implies a reduction in heat transport across the equator which allows heat to pool in the Southern Hemisphere while the Northern Hemisphere cools (Stocker & Johnsen, 2003).

Heinrich Events

Heinrich events are a second type of well-documented, abrupt climate change which are particularly common in the latter halves of glacial periods (Rahmstorf, 2002). They are associated with catastrophic shut downs of AMOC (Fig. 2.3.1). Heinrich events are identified in North Atlantic marine sediment cores as distinct, intermittent layers of coarse to very coarse

lithic grains which can only have been transported and deposited in the open ocean by icebergs (Heinrich, 1988; Bond et al., 1992)). Thus, Heinrich deposits are referred to in the literature as Ice Rafted Debris (IRD). Heinrich events are thought to be caused by massive, episodic purges of the Laurentide Ice Sheet during which as much as 10% of the ice sheet's total volume destabilized and slid into the North Atlantic. This amounts to an anomalous freshwater forcing of up to 0.1 Sv (Rahmstorf, 2002), enough to stop, or drastically reduce overturning circulation for up to several centuries.

Heinrich events are not observed in every D-O stadial. When they do occur, climate records indicate intense, large amplitude cooling in the North Atlantic region that exceeds non-Heinrich stadial temperatures (Rahmstorf, 2002). Greenland climate records, on the other hand, show that stadials were equally cold whether a Heinrich event occurred or not (Rahmstorf, 2002; Lynch-Stiglitz, 2017). This distinctive climate signature lends further support to the hypothesis that shifting open ocean convection locations drive D-O paced climate change. During a stadial phase, heat transport would be limited to lower latitudes south of Greenland. In this case, an additional reduction or shut down of overturning during a Heinrich event, would have little effect on already cold Greenland temperatures, while more southerly Atlantic regions whose climates are directly modified by heat transport in the upper branch of AMOC, would experience dramatic cooling.

North Atlantic Oscillation (NAO)

Another pattern of climate variability known to be particularly significant to wintertime climate variability in the Atlantic region is the NAO. Instrumental observations over the past 150 years have revealed that on decadal timescales the NAO displays persistent negative and positive index phases which appear to have profound consequences for North Atlantic climate trends (Hurrell, 1995). The NAO is usually expressed as an index of normalized sea-level pressure between the Iceland atmospheric low-pressure cell and the high-pressure cell centered over the Azores (Boessenkool et al., 2007). During a positive NAO index phase, these low- and high-pressure cells are stronger than usual which intensifies the westerly wind belt running between them, forcing the Atlantic storm belt to curve a little further north than usual (Vallis, 2012). This brings warmer, wetter winter weather to northwestern Europe while southern Europe remains cooler and drier than usual. During a negative NAO index phase, conditions are just the opposite with weaker than usual pressure cells causing the storm track to trend south

bringing the mild, wet winter weather to southern Europe while northern Europe remains cold and dry (Vallis, 2012).

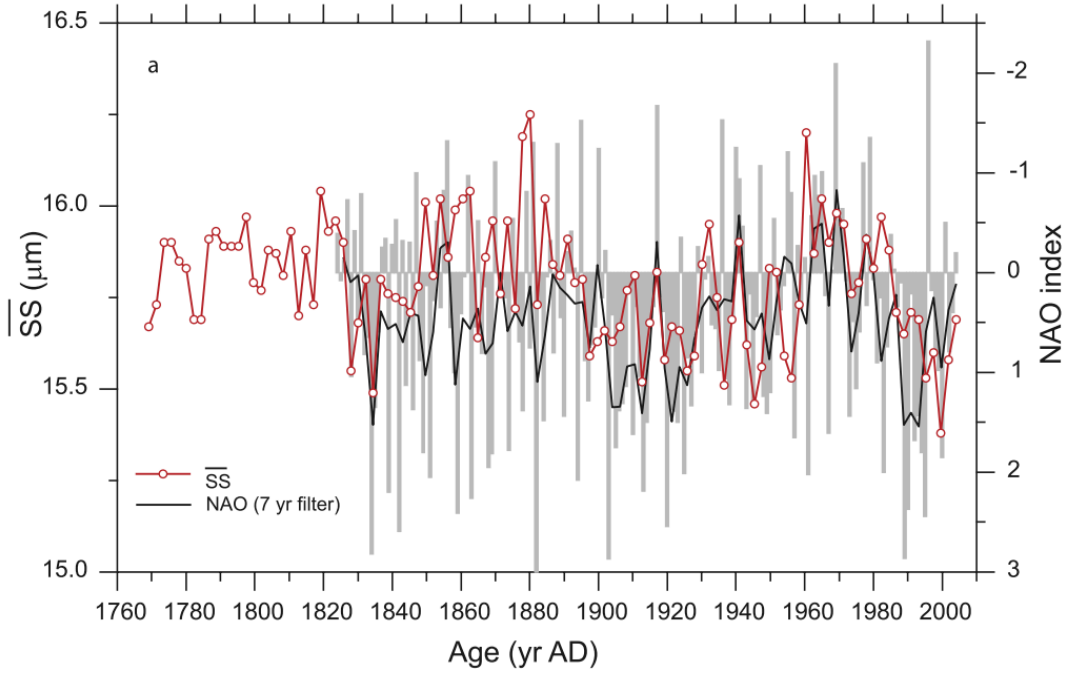

Figure 2.8. $\overline{SS}$ record from core RAPID-21-12B (red) plotted with NAO winter index over the past 270 years (gray bars, reversed scale). The black line is a 7-year smoothed NAO index. The ISOW flow speed, as recorded by $\overline{SS}$, displays a roughly inverse coverability with the NAO index (Boessenkool et al., 2007).

In a recent study, Boessenkool et al. (2007) analyzed grain size variability ($\overline{SS}$) over the past 230 years from a box-core recovered on the southern limb of Gardar Drift (RAPID-21-12B, 57°27 N, 27°54 W, 2630 m water depth), and found a previously unknown inverse correlation between the NAO index and ISOW flow speed (Fig. 2.8). This inverse relationship is especially evident in the NAO reversal from a persistent negative state during the 1960's to a strongly persistent positive state in the 1990's. During this reversal, $\overline{SS}$ values decrease suggesting a pronounced slowing of ISOW flow speeds. Boessenkool et al. (2007) also found a notable increase in the transport volume of relatively fresh, cold Labrador Sea Water (LSW) entering the Irminger and Iceland basins in the 1990's when the NAO was locked in a persistent positive phase. Boessenkool et al. (2007) attributed this increase to a period of exceptionally deep, vigorous open ocean convection following multiple high-NAO index winters with extremely cold conditions over Greenland and the Labrador Sea. This raises the intriguing possibility that variations in the volume and eastward extent of LSW and its subsequent entrainment into ISOW could alter downstream flow speeds and overall AMOC on an NAO-paced timescale (Thornally et al. 2013.)

Atlantic Multidecadal Oscillation (AMO)

One final mode of high-frequency climate change that has been tentatively linked to AMOC variability (Delworth & Mann, 2000; Knight et al. 2005) is Atlantic Multidecadal Oscillation. AMO is described by Kerr (2000) as a quasi-periodic, multi-decadal pattern of sea surface temperature variability centered over the North Atlantic. Oscillations between warm and cold periods in the range of 0.4°C last 65-80 years, and appear to have been a persistent feature of the climate system for a least the past 1500 years (Mjell et al., 2016). Furthermore, combined observational records of terrestrial and marine temperature anomalies suggest a coherent pattern of AMO-paced fluctuations over much of the northern hemisphere (Knight et al., 2005).

Kerr (2000) proposed the following driving mechanism for AMO variability: when AMOC is strong, more heat is delivered to high latitude deep water formation regions via warm, saline surface currents. This is a warm AMO mode. However, the increased heat accumulation eventually weakens buoyancy gradients making it harder for surface water to become dense enough to sink. Reduced deep water formation slows surface currents, and less heat is drawn into the North Atlantic bringing the climate into cold AMO mode. When AMOC is sluggish, the increased time between overturning events allows salt to accumulate in surface waters, which eventually become dense enough sink and restore vigorous deep water formation and northward heat transport, thus returning the climate to warm AMO mode.

Recently, Mjell et al. (2016) reconstructed AMO-paced fluctuations in a $\overline{SS}$ record from an intermediate depth core on the northern end of Gardar Drift (Core GS-144-09MC-D; 60°19 N, 23°58 W; 2018 m depth). Their record showed a strong correlation with the observational AMO temperature index; with periods of relatively strong ISOW vigor corresponding to warm Atlantic SST, and periods of reduced ISOW vigor corresponding to periods of cooler Atlantic SST. The Mjell et al. (2016) results demonstrate that at least one major branch of AMOC appears to vary in phase with Atlantic surface climate on AMO-paced timescales.

2.4 MIS 5e climate evolution: previous work

The mid to late Holocene (i.e. the past 7 kyr) has been characterized as a period of relative stability with regards to climate and ocean circulation. It was long assumed that such stability was a ubiquitous feature of warm, interglacial climates, including the LIG (GRIP members, 1993). However, a growing body of evidence coming from high resolution marine and

terrestrial climate proxy records is changing our perception of the LIG as a period of uniformly stable warmth and vigorous overturning, to one marked by multiple, transient cooling events and overturning instability.

The first evidence suggesting more variable LIG conditions came from the Greenland Ice Core Project (GRIP) (Dansgaard et al., 1993). The GRIP record displayed unexpected variability in the Eemian-aged layers of the ice core where high-frequency, high amplitude oscillations in the $\delta^{18}O_{ice}$ and Ca^{2+} concentration data signified multiple, prominent cooling events over central Greenland. Controversy arose when the Greenland Ice Sheet Project 2 (GISP2) (Grootes et al., 1993) failed to demonstrate coherent variability in the corresponding Eemian sequence in their near-by core. It was concluded that the ice layers near the base of GISP2 had been corrupted by folding and/or slippage, and it was later confirmed that all of the ice older than 110 kyr BP in both cores had been affected by ice tectonics (Adams et al., 1999). Nevertheless, the initial GRIP results had piqued the interest of the community, and sparked a flurry of detailed research aimed at testing their validity (Maslin & Tzedakis, 1996).

Early marine core studies along these lines show conflicting results. McManus et al. (1994) and Adkins et al. (1997), for example, study cores from the Feni Drift and the Bermuda Rise respectively, and find little to no evidence for climate variability during MIS 5e. Cortijo et al. (1994; 1999), on the other hand, find compelling evidence for a single significant cooling and freshening event in the middle of the MIS 5e benthic plateau in at least eight cores on a meridional transect following the path of the North Atlantic Gulf Stream (30°-72° N). Overall, the preponderance of this early evidence converges around this single "intra-Eemian cooling event" centered somewhere between 122-125 kyr BP (Adams et al., 1999). During this event surface water freshened and sea surface temperatures dropped by 2°- 4°C (Cortijo et al., 1999). In addition, a brief, but significant reduction in benthic $\delta^{13}C$ suggests a concurrent reduction in NADW ventilation (Maslin & Tzedakis, 1996). The general absence of IRD in peak MIS 5e sediments (McManus et al., 1994), makes it highly unlikely that the trigger for this observed freshening and coincident reduction in deep water formation was a Heinrich-like event. Rather, Cortijo et al. (1994) ascribe the freshwater flux to high interglacial sea levels which allowed an increased flux of relatively fresh North Pacific surface water to enter the Arctic Mediterranean through the Bering Strait, as well as to particularly high sea surface temperatures during the insolation maximum which enhanced evaporation and lead to increased precipitation at high

latitudes. Together these two sources of anomalous fresh water reduced surface water buoyancy and temporarily suppressed, but did not entirely stop, deep water formation in the Nordic Seas ~123 kyr BP ago.

More recently, an increasing number of high-resolution records are finding mounting evidence to support the idea of high-frequency, high-amplitude deep water variability throughout the LIG. For example, Bianchi et al. (2001) analyzed $\overline{SS}$ and $\delta^{13}C$ data on a pair of cores (3481 and 4760 m depth) located on the Blake Outer Ridge in the subtropical NW Atlantic basin. Both cores revealed an unexpected degree of near-bottom flow variability throughout the MIS 5e benthic plateau. The authors tentatively linked these fluctuations to variability in deep water convection, though the cores' locations, relatively far from any deep water source region, means that the entrainment of anomalously warm or fresh intermediate waters along the NADW flow path could also influence the downstream speed and/or depth of the boundary current independent of deep water production rates. Although the Bianchi et al. (2001) records found only limited evidence for a significant cooling event centered around 124 kyr, both cores did record a substantial deceleration in current speeds marking the end of the benthic plateau (~118 kyr), and a concurrent reduction in $\delta^{13}C$, especially in the deeper core. This correlation strongly suggests a shoaling of the boundary current and subsequent invasion of poorly ventilated SSW marking the end of the interglacial period.

Downcore IRD occurrence and shifting foraminiferal assemblages—especially the relative percentage of the polar, planktonic, sinistral-coiling species *Neogloboquarindrina pachyderma* (Nps%)—have been used in conjunction with $\delta^{13}C$ and/or $\overline{SS}$ to demonstrate a link between surface cooling events and deep ocean reorganization (Oppo et al., 2006; Galaasen et al., 2014; Deaney et al., 2017). Oppo et al. (2006) analyzed MIS 5 sediments in a core located on the Feni Drift, and showed that even very small IRD peaks (<10 lithic counts/g) were accompanied by reductions in $\delta^{13}C$ values. This correlation demonstrates a close relationship between ice rafting, cooling and freshening events, and deep ocean circulation changes. As mentioned, there is little evidence of widespread IRD deposits in the North Atlantic during the middle LIG period (120-124 kyr BP), however, there is strong evidence supporting continued delivery of IRD material well into the early LIG (130-124 kyr BP) (Oppo et al., 2006; Sanchez-Goni et al., 2012). The presence of IRD in the early interglacial suggests a prolonged period of ice retreat and associated meltwater flux coinciding with peak boreal summer insolation (Hodell et al.,

2009; Sanchez-Goni et al. 2012). Low $\delta^{13}C$ values and slow current speeds have also been observed at this time (Hall et al., 1998; Hodell et al., 2009) suggesting that the establishment of a vigorous, interglacial mode of deep water formation was delayed during the LIG until ~124 kyr BP.

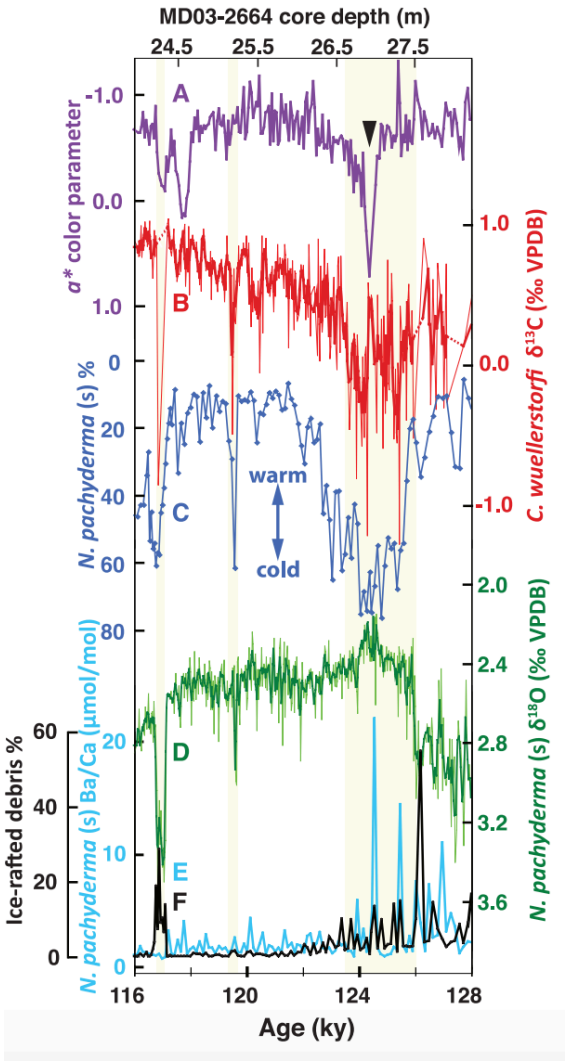

Figure 2.9. Climate proxy records for the peak MIS 5e section of core MD03-2664 (57°26 N, 48°36 W; 3442 m water depth). (A) Red-green color parameter, (B) *C. wuellerstorfi* δ13C with 3-point running mean, (C) NpS%, (D) *N. pachyderma* (s) δ18O with a 3-point running mean, (E) *N. pachyderma* (s) Ba/Ca, (F) IRD %. The yellow shading indicates periods of pronounced NADW reductions (Galaasen et al. 2014).

Galaasen et al. (2014), on the other hand, have suggested a different view of AMOC evolution during the early LIG. Their record from an intermediate depth core on the Eirik Drift (Fig. 2.9) shows an overall increasing, long-term $\delta^{13}C$ trend, suggesting that a strong NADW influence was re-established almost immediately after Termination II and persisted throughout the LIG. However, this apparent long-term, multi-millennial scale stability was repeatedly interrupted by transient $\delta^{13}C$ decreases, which indicate prominent short-term changes in bottom-water

chemistry were also a robust feature of the LIG world. The earliest part of the record is characterized by relatively stronger variability than the later part. The single largest negative $\delta^{13}C$ anomaly occurs at ~124 kyr BP suggesting a sudden incursion of poorly ventilated SSW due to a reduction in convection activity and/or a shoaling of the boundary current flowing over the core site. Coeval increases in IRD and N. pachyderma (s) percentages (Fig. 2.9) further support the previously mentioned idea that surface density gradients were repeatedly challenged during the early LIG by persistent delivery of residual icebergs and associated freshwater fluxes.

NADW appears to have stabilized after ~124 kyr BP, presumably because global ice volume had reached its peak interglacial minimum, and meltwater forcing in the sensitive deep water formation regions had finally ceased (Galaasen et al. 2014). However, rapid, centennial-scale variability remains a prominent feature of high-resolution records (e.g. Irvali et al., 2012; Galassen et al. 2014; Deaney et al., 2017) throughout the mid-MIS 5e period. Another prominent negative excursion, similar in magnitude to the 124-kyr BP anomaly, marks the end of this relatively stable period of steadily strengthening and deepening convection. This apparent cooling event, centered at ~120 kyr BP, is identifiable in all of the previously referenced proxy records, and appears to be a robust, regionally coherent event that signified the beginning of the end of the MIS 5e interglacial, followed by the steady climatic deterioration into MIS 5d stadial conditions. The mechanism behind the 120-kyr BP cooling is uncertain, but it is most likely that the type of warming and freshening related hydrologic changes suggested by Cortijo et al. (1994) played a critical role in increasing buoyancy and suppressing NADW towards the end of the LIG (Galaasen et al. 2014).

This has been a necessarily abbreviated accounting of the current research regarding MIS 5e circulation and climate evolution. It is clear that the literature remains somewhat equivocal. This is perhaps unsurprising given the inherent difficulty in resolving the spatial and temporal heterogeneity of geographically diverse climate signals. Nevertheless, the broader strokes are in place. While the original paradigm of a stable, vigorous mode of interglacial circulation appears to be true over multi-millennial time-scales, recent high-resolution proxy records are increasingly confirming a persistent pattern of short-term variability over this generally stable background trend as an equally robust feature of MIS 5e circulation. This thesis seeks to add

new data constraining physical flow changes in the eastern overflows and their relationship to deep water chemical changes of the type described above.

3. STUDY AREA

The mean sortable silt data presented in this thesis was generated from material collected at IODP Site U1304 (53°03.40'N, 33°31.78'W; water depth 3024 m). Site U1304 is located on the extreme southern end of the Gardar Drift, an elongated contourite accumulating on the eastern flank of the Reykjanes Ridge (Figs. 3.1 and 3.8). In this chapter I describe the geography, bathymetry, and oceanography that define this region, and play a crucial role in forming and directing the path of ISOW. Variability in the rate of formation and consequent flow speed of this important density current is the particular focus of this thesis.

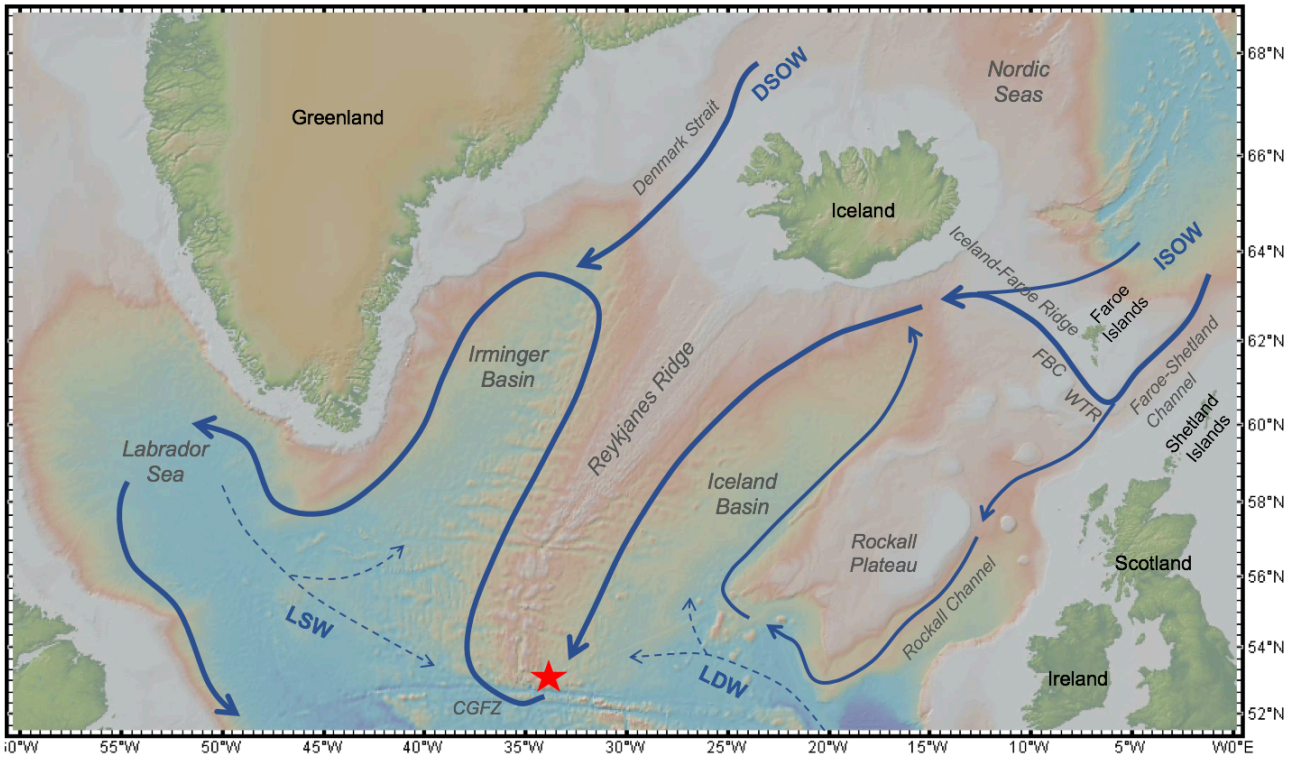

Figure 3.1. Bathymetric map over the core site and surrounding region. The location of Site U1304 is marked with a red star. The path of the primary overflow and deep water masses discussed in Chapter 3.3.2 is marked as blue arrows. Denmark Strait Overflow Water (DSOW) and Iceland-Scotland Overflow Water (ISOW) cross the sills of the Greenland-Scotland Ridge and then flow as Deep Western Boundary Currents centered at about ~2500-3000 m depth. Labrador Sea Water (LSW) bathes the Irminger and Iceland Basins at ~1300-2000 m depth (Bianchi & McCave, 2000). Lower Deep Water enters the northeastern North Atlantic from the southeast and bathes the abyssal Iceland basin below ~4000 m depth (Bianchi & McCave, 2000). Background map modified from GeoMapApp (2018).

3.1 Geographic setting: the Greenland-Scotland Ridge

The Reykjanes Ridge divides the North Atlantic sea bed south of Iceland into two narrow basins: the Irminger Basin to the west of the ridge, and the Iceland Basin to the east (Fig. 3.1). A third, narrower basin, the Rockall Channel, is separated from the Iceland Basin by a shallow marine structure known as the Rockall Plateau. These three basins are bounded to the north by the Greenland-Scotland Ridge (GSR), a continuous, submarine barrier which extends from East Greenland to Scotland, and completely isolates North Atlantic waters from Norwegian-Greenland-Iceland Sea waters (collectively known as the Nordic Seas) below a depth of 840 m (Hansen & Østerhus, 2000). Above this depth, water is exchanged between the North Atlantic and the Nordic Seas either as warm, north-flowing surface currents, or as cold, dense south-flowing intermediate waters which flow over the GSR through several discrete sills of different geometries and depths (Fig. 3.2.1). It is these dense overflow waters which are of primary interest here as they constitute the source waters for the globally important lower North Atlantic Deep Water.

3.2 Oceanographic setting: Nordic Seas overflows

West of Iceland, overflow waters pass through the Denmark Strait, a fairly wide sill with a maximum depth of ~620 m adjacent to the western Iceland shelf (Fig. 3.2). Once over the GSR, Denmark Strait Overflow Water (DSOW) follows the sea bed topography around the southern tip of Greenland into the Labrador Sea (Fig. 3.1). The Iceland-Faroe Ridge is the wide, shallow sill east of Iceland with depths ranging from ~420 m close to the eastern Iceland shelf to ~480 m nearer the Faroe Islands. Five highly variable overflow streams have been observed spilling over the Iceland-Faroe Ridge (Hansen & Østerhus, 2000). East of the Faroe Islands, the ridge topography is more complex. Overflow waters leave the southern Norwegian Sea through the Faroe-Shetland Channel (Fig. 3.1), and are then further funneled into the North Atlantic through the Wyville-Thomson Ridge and the Faroe Bank Channel. Overflow through the Wyville-Thomson Ridge (sill depth ~600 m) tends to pool in a deep gully between the Faroe Bank and a shallow structure just south of the sill known as the Ymir Ridge. Thus, overflow through this sill into the North Atlantic is intermittent and minor. The Faroe Bank Channel, on the other hand, is a deep, narrow sill (~800 m) which funnels overflow waters westward along the GSR to join those streaming over the Iceland-Faroe sills. Accumulated ISOW (i.e. the combined Iceland-Faroe Ridge and Faroe Bank Channel overflows) flows south as a coherent boundary current along the eastern flank of the mid-Atlantic ridge, crossing the ridge at the Charlie Gibbs

Fracture Zone (CGFZ) into the Irminger Basin where it eventually joins up with DSOW on its path towards the Labrador Sea (Fig. 3.1).

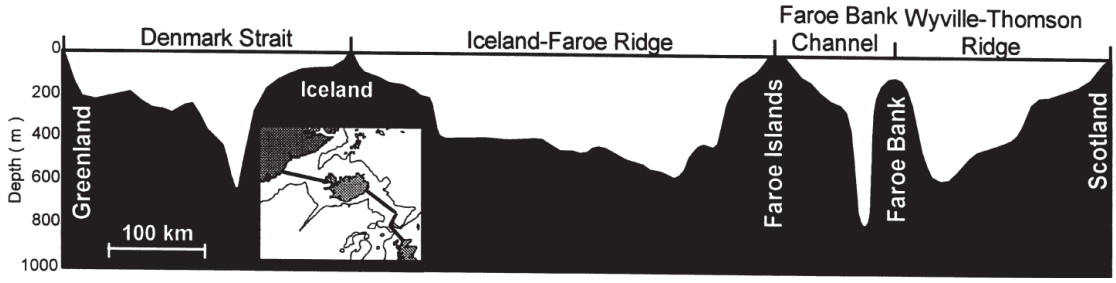

Figure 3.2. Depth profile across the Greenland-Scotland Ridge showing the overflow sills. The east-west transect of the profile is shown in the inset map (Hansen and Østerhus, 2000).

Roughly 6 Sv (1 Sv = 10^6 m^3/s) of water is exchanged between the Nordic and North Atlantic Seas over the GSR (Hansen & Osterhus, 2000). The cold, dense outflow of intermediate water masses spilling into the North Atlantic basin as density currents, is replaced by an equal volume of warm, salty water flowing northward into the Nordic Seas primarily as wind driven surface currents. Figure 3.3 illustrates how this exchange of water affects potential temperature and salinity profiles on either side of the ridge. The Atlantic side of the ridge is dominated by relatively warm, saline water (>5°C, >35.0 psu) down to ~1000 m depth, whereas the Nordic side is dominated by cold, low-salinity water (<0°C, ~34.9 psu) from ~500 m depth. Near-surface waters on the northeastern side of the ridge bear the same T-S signature as the Atlantic water and clearly indicate that North Atlantic surface currents penetrate far into the sub-polar region before cooling and sinking in the Nordic Seas interior. Likewise, a thin layer of cold, low-salinity Nordic Seas water is observed to hug the southwestern side of the ridge, indicating the presence of intermediate overflows as they spill into the North Atlantic basin and begin to mix with surrounding Atlantic waters. These waters meet at the tightly topographically bound Iceland-Faroe Front.

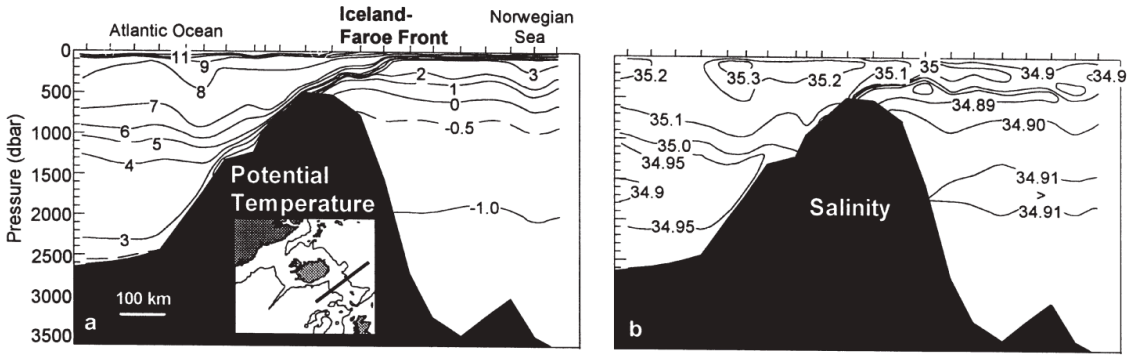

Figure 3.3. Potential (a) temperature and (b) salinity depth profiles for a transect crossing the Iceland-Faroe Ridge. The location of the transect is shown in the inset map (Hansen & Østerhus, 2000).

3.3 Hydrography

Large scale ocean circulation has two main components: circulation in the upper ~1000 m which involves wind-forced, predominantly horizontal Ekman transport of surface waters in basin-wide gyres; and circulation in the deep ocean which is primarily associated with the vertical sinking of cold, dense water masses at high latitudes, and their subsequent rise to the surface somewhere far from their source region (i.e. meridional overturning circulation) (Talley, 1996). Buoyancy forcing and the thermohaline processes that create the density gradients driving MOC have already been discussed in Chapter 2.1. Here I describe the major circulation pathways and water masses associated with surface and deep-water circulation in the North Atlantic and Nordic Seas.

3.3.1 Circulation

Broadly speaking, the two most prominent features of surface circulation in the North Atlantic are an anticyclonic, subtropical gyre spanning the basin between 15-45°N latitudes; and a cyclonic, subpolar gyre whose circulation is split by the GSR into two circulating centers, one south of Iceland recirculating in the Irminger Basin, and the other north of Iceland streaming through the Nordic Seas (Fig. 3.3.1) (Talley, 1996). The Gulf Stream emerges off the coast of southern Florida as a strong western boundary current for the subtropical gyre. It follows the North American coast northward as far as Cape Hatteras off the coast North Carolina where it begins to veer northeastward into the open Atlantic (Reid, 1994). East of Newfoundland, the current makes a sharp right turn and continues eastward across the basin as the North Atlantic Current (NAC). After crossing the mid-Atlantic ridge near the CGFZ, part of the NAC turns south to complete the subtropical gyre as the Canary and North Equatorial Currents. Another part veers north into the Iceland Basin where it bifurcates once again. One extension of the flow turns westward as the Irminger Current, forming the subpolar, cyclonic gyre circulating through the Irminger Basin. By convention, the part of the flow that continues northeastward through the Iceland Basin towards the Faroe Islands is still referred to as the NAC (Hansen & Østerhus, 2000). Thus, the northern rim of the subtropical gyre and southern rim of the subpolar gyre are connected through branching of the NAC, with the poleward boundary of the NAC separating warm Gulf Stream derived waters from colder water masses descending from the arctic (Talley, 1996; van Aken & Becker, 1996).

Surface inflow over the GSR and into the Nordic Seas has three separate branches that are not fully articulated in the over-simplified cartoon seen in Figure 3.4. One branch peels off the

Irminger Current, turning north to pass the ridge to the west of Iceland, then veering anticyclonically around Iceland as the North Icelandic Irminger Current. The NAC bifurcates just south of the Faroe Islands. One branch crosses into the southeastern Norwegian Sea over the Faroe-Shetland Channel, while the other crosses over the Iceland-Faroe Ridge. In the literature, these two branches are often lumped together as the Norwegian Atlantic Current (Hansen & Østerhus, 2000).

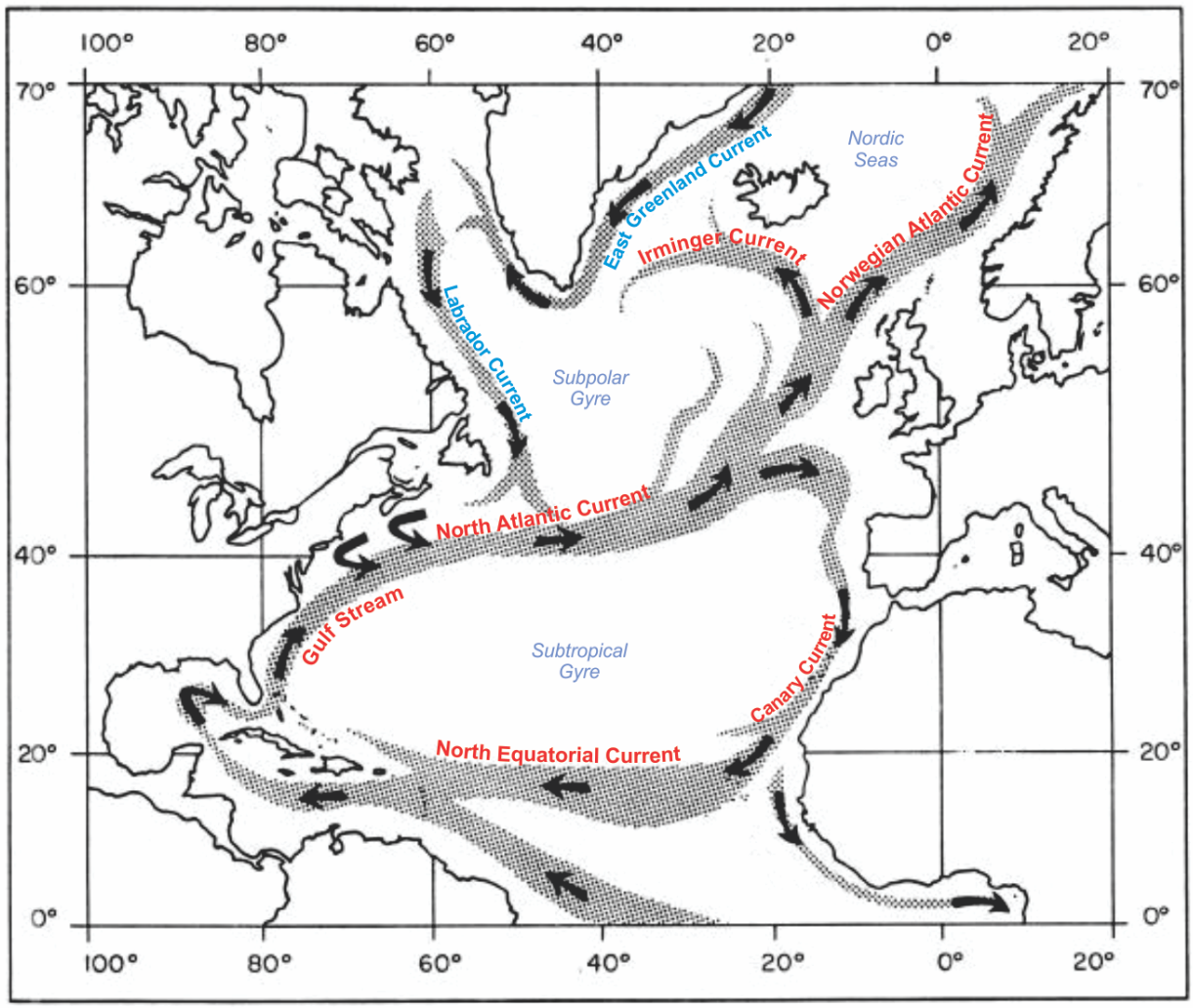

Figure 3.4. Simplified map showing the primary circulation pathways of surface currents in the North Atlantic and Nordic Seas. Warm, salty currents are labeled in red. Cold, fresher currents are labeled in blue. See text for further details, including some surface currents which are not labeled on the figure. Adapted from https://www.bigmarinefish.com/currents.html

In addition to the NAC there are two other minor source waters for inflows into the Nordic Seas (not pictured in Figure 3.4). A stream of relatively fresh, cold water entering the Arctic Ocean through the Bering Strait contributes about 1 Sv of inflow (Hansen & Østerhus, 2000). And a second, Atlantic sourced current, originating off the coast of southern Europe, flows northward

along the continental shelf, and enters the Norwegian Sea through the Faroe-Shetland Channel. This so-called Continental Slope Current is the warmest, saltiest water mixing in the Nordic Seas (Hansen & Østerhus, 2000).

As warm Atlantic inflow waters progress into the Nordic Seas and further into the Arctic, they release their heat and salt to the atmosphere and surrounding water, and are converted into a cold, salty water mass. Some of this mass sinks into the interior (Norwegian Sea Intermediate and Deep Water), and eventually returns to the Atlantic as dense, intermediate GSR overflows, while some returns as cold surface currents. About three quarters of the Nordic Seas inflow is balanced as the intermediate overflows discussed in Chapter 3.2, the remaining one-quarter occurs as the south flowing western boundary currents of the subpolar gyre (Hansen & Østerhus, 2000). The East Greenland Current is a shallow, relatively fresh surface current flowing south through the Denmark Strait. It acts as a major pathway for the export of polar-sourced freshwater (i.e. sea-ice and continental run-off) to the North Atlantic (Jakobsen et al., 2003). The Labrador Current joins the denser flow of intermediate water exiting the Labrador Sea, flowing south- and then westward under the NAC as a Deep Western Boundary Current (DWBC) carrying NADW into the lower latitudes (Talley, 1996).

3.3.2 Water masses

The Gardar Drift lies in the Iceland Basin along the eastern flank of the Reykjanes Ridge. Five distinct water masses have been identified within the Iceland Basin (van Aken & Becker, 1996; Bianchi & McCave, 2000). These five water masses are of particular interest here as they are likely components of the DWBC which flows NE—SW along the Reykjanes Ridge carrying and redistributing the sediments which accumulate to form the drift. Water masses are generally defined by maxima and minima in their density ranges, and are often illustrated in plots of potential temperature versus salinity, oxygen, or silica (Fig. 3.5). Because the classification of water masses in this manner is somewhat arbitrary, different authors have adopted different criteria and used different names to describe individual water masses. For convenience, I will use the names and properties plotted and defined by van Aken & Becker (1996), and later confirmed by Bianchi & McCave (2000), to describe the five water masses flowing over the Iceland Basin.

Surface waters (0—~500 m depth

The warm, saline waters in the near surface layer above the main thermocline are known as Subpolar Mode Water (SPMW). This water mass is ubiquitous throughout the subpolar gyre region, and is the same surface water entering the Nordic Seas through the NAC system. SPMW is thought to form locally as a result of deep, winter-time convection which may explain its wide range of characteristic hydrographic properties (4-14°C, 34.95-35.50 psu) (van Aken & Becker, 1996). SPMW tends to grow cooler and fresher as it moves from west to east across the Iceland Basin, a clear indication of progressive winter-time modification as it moves along the NAC path.

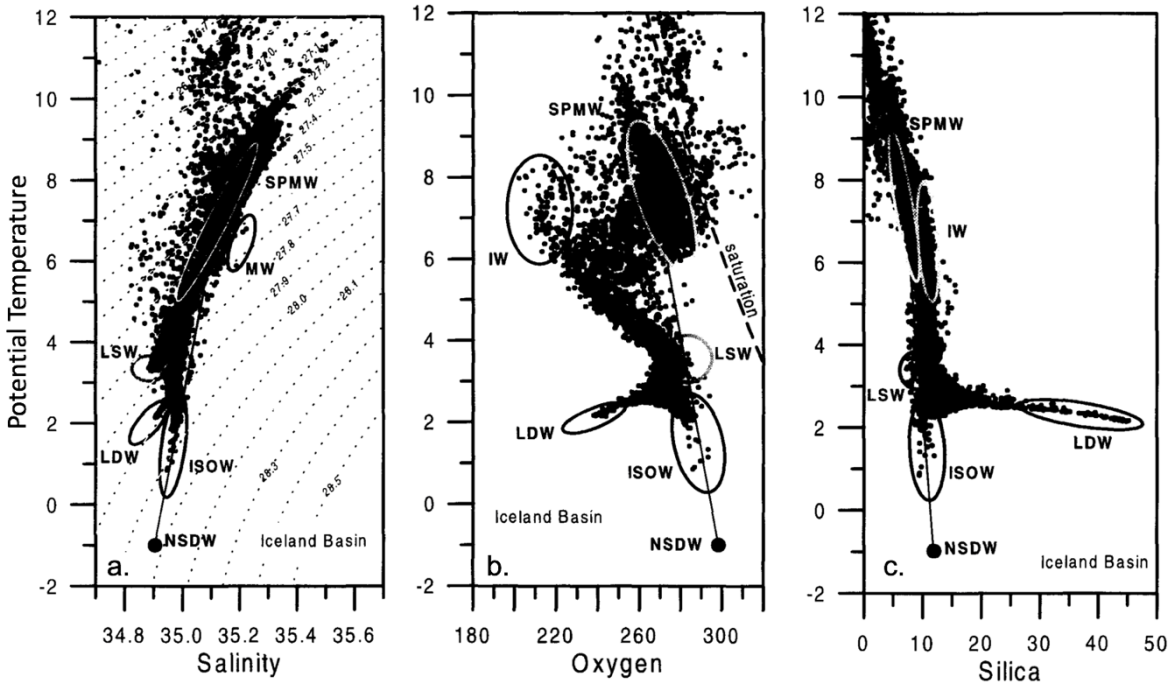

Figure 3.5. The five main water masses in the Iceland Basin as defined by T-S diagrams showing CTD results of (a) salinity, (b) oxygen, and (c) silica. The data for these plots was collected from 988 hydrographic stations which were analyzed between 1983-1991. The solid line represents the mixing line between Norwegian Sea Deep Water (NSDW) and the center of the SPMW ellipse (Adapted from van Aken & Becker, 1996).

Intermediate waters (500—2000 m depth)

The water mass below is an ambiguous mass tentatively labeled Intermediate Water (IW). This mass is identified as an oxygen minimum with relatively high silica values in the 6-8°C range (Fig. 3.5b and c). The origin of IW is uncertain, but its distinctive geochemical signature suggests that it may be the remains of aged Antarctic Intermediate Water advected into the subpolar gyre through the Gulf Stream and NAC pathway (Bianchi & McCave, 2000).

Labrador Sea Water (LSW) is the thick parcel of water which dominates the intermediate depths of the Iceland Basin. It is characterized as a salinity minimum (<34.90 psu between 3-3.5°C) with relatively high oxygen concentrations, especially compared to IW lying just over it (Fig. 3.5b). This distinctive geochemical fingerprint results from LSW's formation during deep winter convection in the Labrador Sea. Thus, the low salinity is due to LSW's source waters which include SPMW circulating into the Labrador Sea from the Irminger Sea, as well as cold, fresh Arctic water flowing south through the Canadian Archipelago; and its high oxygen content is due to the fact that it is a relatively young, recently ventilated water mass. From its source area, LSW spreads both southward as a component of NADW, and eastward into the Iceland Basin along the NAC pathway. Although LSW appears to interact directly with the shallower sediments of the Bjørn Drift (a small contourite located northwest of Gardar Drift, nearer the southern Icelandic Shelf), there is no indication that the LSW currently penetrates deep enough to reach the surface of the Gardar Drift sediments (Bianchi & McCave, 2000).

Deep waters (>2000 m depth)

Water overflowing the GSR sills between Iceland and Scotland, that is to say, over *both* the Iceland-Faroe Ridge and through the Faroe Shetland Channel, is collectively called Iceland Scotland Overflow Water. The mean flux of ISOW into the Iceland Basin is 3 Sv, with the bulk of that flux, 2-2.5 Sv, being NSDW flowing through the Faroe Bank Channel (Hansen & Østerhus, 2000). ISOW is a mixture of NSDW, SPMW, and LSW. The placement of the ISOW ellipse centered directly over the NSDW—ISOW mixing line on the T-S diagrams in Figure 3.5 demonstrates this relationship. Inside the Faroe-Shetland Channel, NSDW has been shown to have a typical T-S signature of -1°C, 34.90 psu (van Aken & Becker, 1996). Just below the sill, however, ISOW has typical T-S values of 2.5°C, 34.98 psu. The immediate warming and freshening of ISOW are indications of rapid modification and vigorous entrainment of ambient waters as the overflows plunge over the sills.

Lower Deep Water (LDW) is the deepest major water mass observed in the Iceland Basin. It is characterized as a cold, relatively fresh mass with low oxygen and high silica concentrations (Fig. 3.5b and c). These distinctive geochemical properties are a result of LDW's origins as a southern sourced water mass. Antarctic Bottom Water (AABW) is exceptionally cold, dense deep water which forms as a result of brine rejection over the Antarctic shelf in the Weddell Sea (Reid, 1994). AABW dominates the abyssal South Atlantic basins, and is advected

northward as a DWBC, eventually crossing the mid-Atlantic Ridge into the northeastern Atlantic through the Vema Fracture Zone at 11°N latitude. LDW is the modified remains of AABW as it presents in the abyssal North Atlantic with an increased T-S signature (2.24°C, 34.94 psu) due to progressive downward diffusion of heat and salt from overlying water masses during its long journey north (van Aken & Becker, 1996). Figure 3.6 shows a T-S diagram for Station 24 of the Bianchi & McCave (2000) study. Station 24 is located slightly to the east of Site U1304 on the southern Gardar Drift, and ~200 m deeper. In the plot, the presence LDW is inferred to be currently bathing the study site from the slight salinity decrease with respect to overlying ISOW.

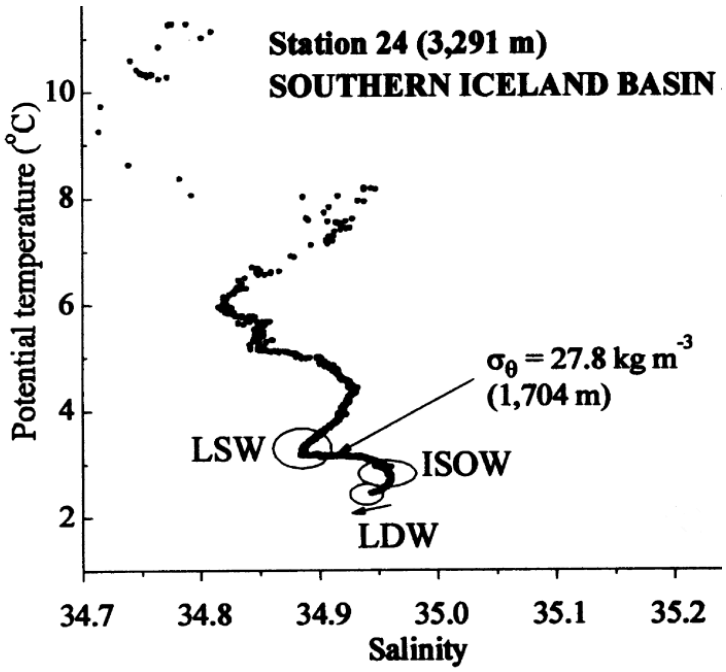

Figure 3.6. T-S plot for a study site near Site U1304 showing the influence of LDW inferred from a slight salinity decrease (Slightly modified after Bianchi and McCave, 2000).

Finally, although terms such as NADW and ISOW are often used in a general sense to refer to various aspects of the south-flowing, deep return branch of MOC, detailed hydrographic discussions such as this reveal them to have far more specific operational definitions. NADW, for example, is understood in generalized global overturning schematics (Fig. 2.3) to be the principal, south-flowing layer of high salinity Atlantic water centered between ~1500—4000 m depth. But NADW is actually a complex mixture of at least five major water masses including the Nordic Seas Overflow Waters, LSW, AAIW, AABW, and very high salinity Mediterranean Water which spills into the North Atlantic through the Straits of Gibraltar (Talley, 1996). These distinctive source waters intermingle in the subpolar and subtropical gyre regions, not becoming

fully homogenized into NADW until the south flowing DWBC current reenters the North Atlantic subtropics. Likewise, ISOW is most often used to refer generally to the NE—SW flowing density current formed by the eastern components of the Nordic Seas Overflow Waters. But more specifically ISOW is a modified version of NSDW, which has been freshened and warmed by the progressive entrainment of SPMW, LSW, and LDW along its flow path down the Reykjanes Ridge. Both the general and specific usages of these terms are equally correct depending on the context. For the present study and following discussion, it is the balance of these individual source waters which have the most impact on the rate and vigor of the density current's flow, and which is known to change on millennial time scales. Therefore, I will continue to use ISOW in its more general sense to refer to the *combined* eastern branch overflows.

3.4 Gardar Drift

As previously mentioned, IODP Site U1304 is located on the far southern end of Gardar Drift in a partially enclosed basin just north of the Charlie Gibbs Fracture Zone (Fig 3.7). The Gardar Drift belongs to a class of current controlled sediment bodies known as giant elongate contourites (Faugères et al., 1993; Wold, 1994; Stow et al., 2002). This type of contourite is particularly common in the North Atlantic where relatively wide, morphologically straightforward basins, and a large sediment supply from surrounding continental shelves provide the ideal conditions for the accumulation of large-scale, high-relief sediment drifts (Faugères et al. 1993). Elongate contourites form when the Coriolis force deflects dense, sediment laden overflow waters towards the western margin of the basin. The effect is to constrain and intensify the flow of the current, causing it to lose or gain competence as it follows topographical contours on its downstream path. Thus, elongate contourites are oriented parallel to their depositing current, and tend to reflect the geometry of the topographic barrier constraining them (Stow et al., 2002). In the case of Gardar Drift, it extends more than 1100 km down the eastern flank of Reykjanes Ridge, and lies almost directly under the core of ISOW whose mean NE—SW flow path is reflected in the crest of the drift. Bjørn Drift is accumulating under similar, though shallower, conditions just north of Gardar Drift on the upper ridge flank. The crests of the two drifts merge just south of 57°N latitude (Wold, 1994: Bianchi & McCave, 2000).

Observations from grain-size analysis carried out by Bianchi & McCave (2000) at 24 stations up and down the length of Bjørn and Gardar Drifts suggest that the core of ISOW is currently

centered between 2000-2600 m water depth, directly interacting with sediments only on the northern end of Gardar Drift. Site U1304, on the other hand, lies on the extreme southern end of the drift where low silt-clay ratios and relatively lower $\overline{SS}$ values suggest a much weaker flow regime. However, Bianchi & McCave (2000) also note that the non-migratory mudwaves observed in the sediments of the southern drift are consistently oriented at a 20° anti-clockwise angle with respect to the local topography which they suggest is evidence of a mean, contour-following flow (i.e. the continued influence of a DWBC as opposed to a local, down-slope flow directed towards the Maury Channel). The sediments that comprise the Gardar Drift are derived primarily from eroded terrigenous material from the Iceland-Faroe Ridge (Wold, 1994).

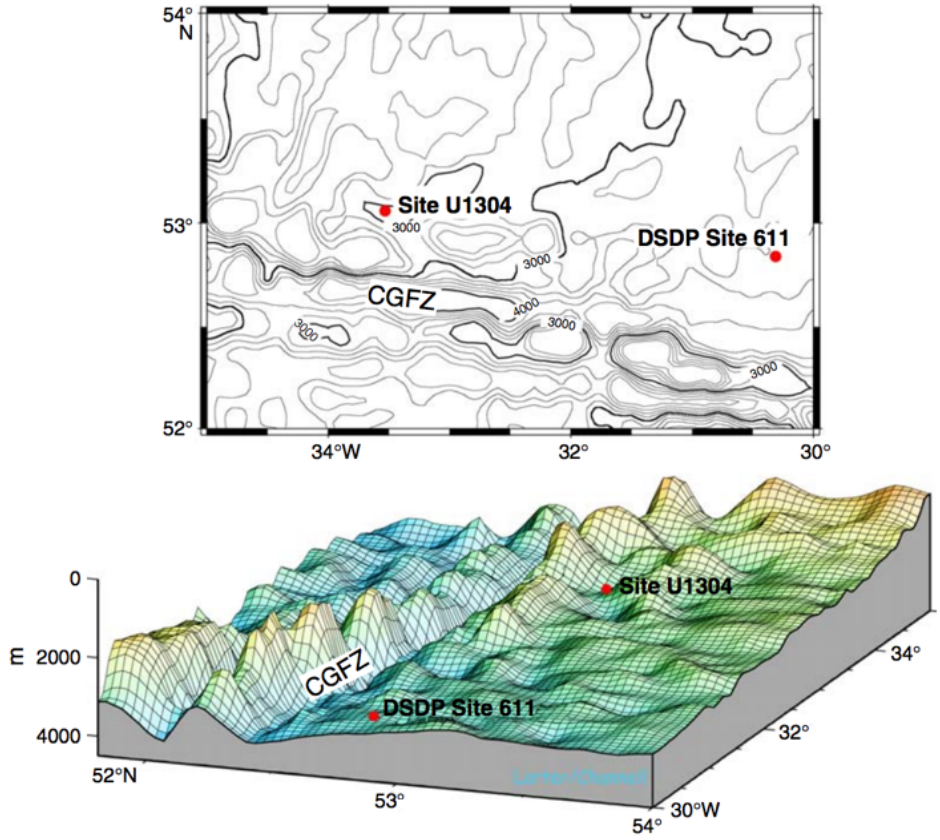

Figure 3.7. Topographic and bathymetric maps showing the location of Site U1304 on the southern Gardar Drift relative to Deep Sea Drilling Project Site 611 and the Charlie Gibbs Fracture Zone (CGFZ). Site 611 was drilled in 1983 and provides early evidence for continuous deposition of Gardar Drift since the Late Miocene (Wold, 1994) (Expedition 303 Scientists, 2006, and references therein).

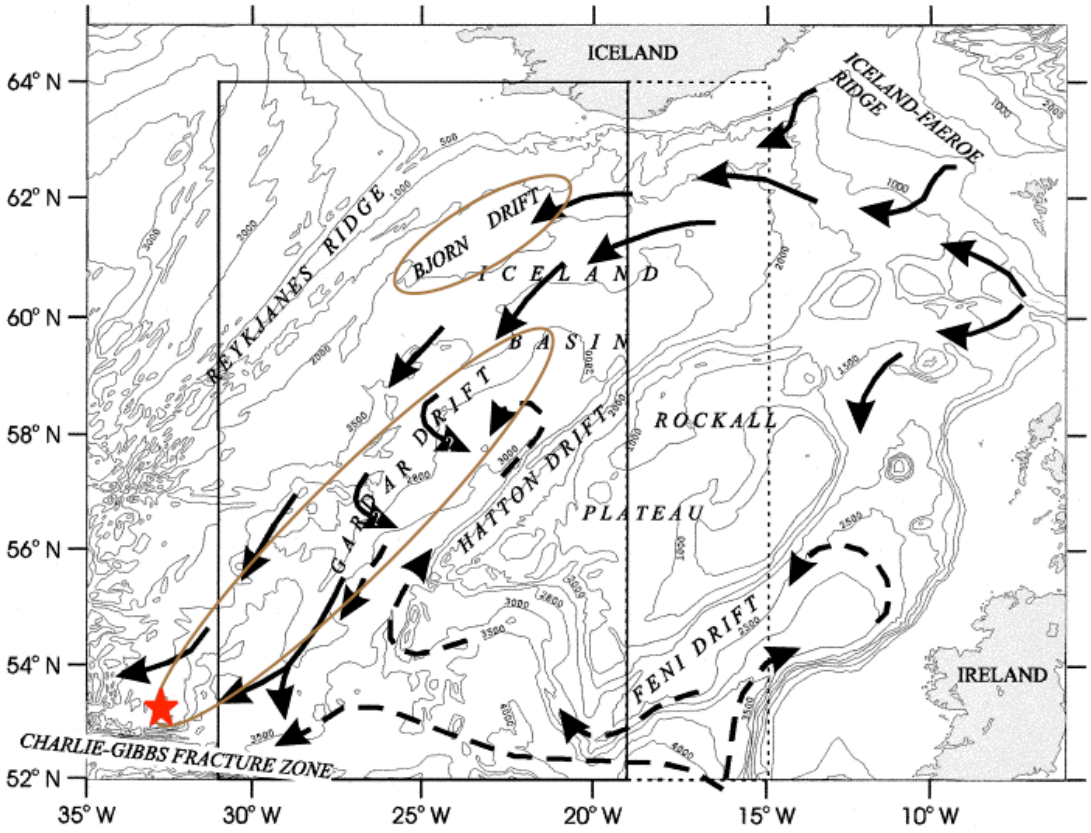

Figure 3.8. Bathymetric map of the northeast Atlantic region schematically showing the approximate extent of Bjørn and Gardar Drifts (brown ovals) in relation to the circulation pattern of ISOW (solid arrows) and southern sourced LDW (dashed arrows). The solid and dashed arrows delimit the study area for Bianchi & McCave (2000). Site U1304 is indicated by the red star (Adapted from Bianchi & McCave, 2000).

4. MATERIALS AND METHODS

In this chapter I present the theory and method behind the mean sortable silt ($\overline{SS}$) paleocurrent proxy, as well as a description of the materials and laboratory procedures used to generate the data presented in Chapter 5.

4.1 Core description

The sediment samples used to reconstruct the sortable silt record in this thesis were obtained from IODP Site U1304 (53°03.40'N, 33°31.78'W; water depth 3024 m), which was cored in October 2004 using an Advanced Piston Corer onboard the *R/V JOIDES Resolution* during IODP Expedition 303/306. The stated objective of Expedition 303/306 was to collect material that would help establish new high-resolution sedimentary archives of environmental conditions within the North Atlantic ice-rafted debris belt at a depth sufficient to monitor NADW properties (Expedition 303, 2006). A detailed description of the oceanographic and hydrographic conditions at Site U1304 was included in Chapter 3. This section will describe the core sediments from which my samples were taken.

Four cores (A-D) were drilled from Site U1304 yielding a correlated, composite depth of 263.8 m. The expedition report (Expedition 303 Scientists, 2006) describes the U1304 core sediments as primarily made up of interbedded diatom and nannofossil oozes with intervals of clay and silty clay. There is little to no evidence of mass-transport events (e.g. slumps and debris flows) in the sediment sequences, nor are redistributed silt and/or sand beds evident. The average sedimentation rate at Site U1304 is reported in the cruise report (Expedition 303 Scientists, 2006) to be ~15 cm/kyr, thus the composite core section is interpreted to represent ~1.8 Myrs of continuous, undisturbed pelagic deposition.

The diatom rich intervals are characterized as episodic and discontinuous, but present throughout the length of the core (Expedition 303, 2006). The diatom mats are composed primarily of the planktic, needle-shaped *Thalassiothrix longissima*, and are thought to form from rapid deposition of aggregated colonies when surface nutrients become depleted (Shimada et al. 2008). The occurrence of diatomaceous oozes in the deep North Atlantic is highly unusual. Similar mats have been documented within the MIS 5e sediments in Core EW9303-17 (57°N, 37°W, water depth 3233 m) approximately 270 nautical miles northwest of Site U1304. It is thought that these diatom populations are associated with migrations of the subarctic

convergence zone, or Arctic Front, where warm, saline water from the North Atlantic Current meets colder, fresher water originating from the East Greenland Current and Labrador Sea (Expedition 303 Scientists, 2006; Xuan et al. 2016). Additionally, the presence of these thick, relatively strong diatom mats tends to suppress bioturbation and resuspension of underlying sediments, thereby preserving the integrity of the depositional archive, and allowing for confidence in a high-resolution record.

4.2 Mean sortable silt

The mean grain size of the coarse to medium terrigenous silt fraction (63 —10 μm) is a well-established physical proxy for the relative speed of deep sea currents. This section will review the theory and method behind the mean sortable silt ($\overline{SS}$) paleocurrent proxy, which uses the degree to which down core fines are size-sorted to infer relative changes in the intensity of bottom flows, with coarser grains indicating relatively faster depositing currents. When combined with complimentary flow rate and water mass proxies (e.g. $\delta^{13}C$ or magnetic susceptibility), $\overline{SS}$ data provide paleoceanographers with a reliable method of reconstructing temporal and spatial variations in deep ocean circulation patterns over geological time.

4.2.1 Theory and basis

The theory and method behind the mean sortable silt paleocurrent proxy evolved from the observation that terrigenous grain-size distributions show a distinct minimum between about 8—10 μm (Fig. 4.1) (McCave and Hall, 2006). The break in the distribution at ~10 μm is interpreted as a critical shift in particle behavior. Specifically, charge imbalances acting on platy clay particles, as well as van der Waals forces acting on fine silts cause particles in this <10 μm size fraction to begin to behave cohesively under depositional conditions, causing them to clump together as aggregates. On the other hand, particles larger than 10 μm tend to behave noncohesively, and are deposited as individual grains in response to decreasing shear stress and current speed.

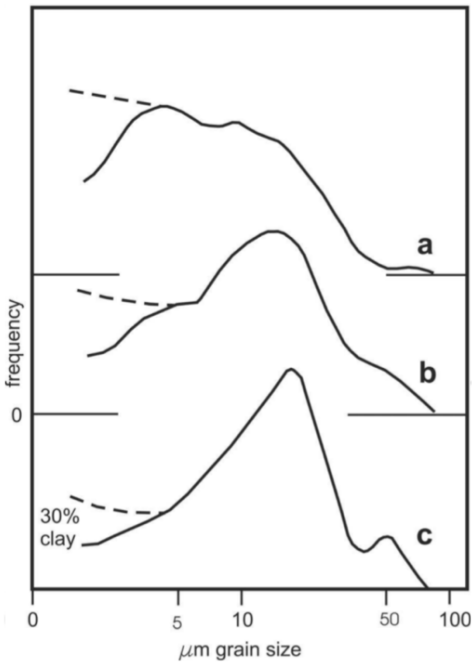

Figure 4.1. Size distributions of sediment from Nova Scotian rise under (a) slow flow: <5 cm/s, (b) moderate flow: 5-10 cm/s, and (c) strong flow: 10-15 cm/s (McCave and Hall, 2006).

The pronounced mode in the >10 μm fraction which appears under increasing flow speeds (Figs. 4.1b and c) is a clear indication of the influence of current-controlled size sorting, with the peak of the mode narrowing and shifting to coarser grains as flow speeds increase. While the more diffuse distribution evident under slow current conditions (Fig. 4.1a) indicates a more pelagic settling pattern with little to no size sorting.

Figure 4.2 further demonstrates the shift in particle behavior in the < 10 μm fraction, this time within the context of critical erosion limits. The curve shows the amount of shear stress needed to move sediment decreasing steadily down to ~10 μm where there is a sudden, sharp increase. This increase in erosional stress is due to the cohesive nature of fine silt and clay which requires more force than non-cohesive material to be moved.

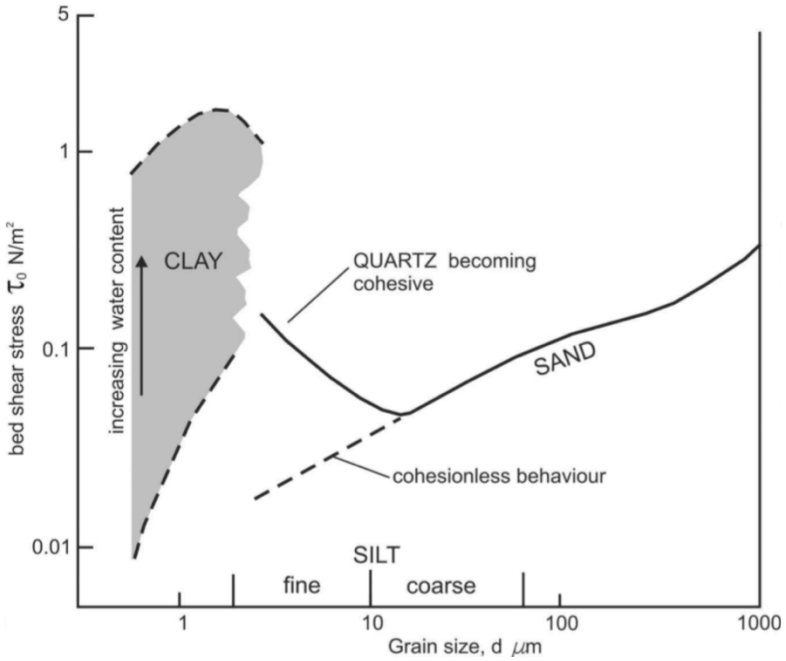

Figure 4.2. Critical erosion curve demonstrating cohesive behavior increasing below 10 μm (McCave and Hall, 2006).

The significance of the theoretical and experimental evidence shown in Figures 4.1 and 4.2 is that only sediment in the 10—63 μm fraction can reasonably be assumed to respond as individual grains to hydrodynamic changes in the current, while finer material tends to be deposited as aggregates. Thus, it is the coarser 'sortable silt' fraction that is considered the most sensitive tracer of the speed of the depositing current, while the fine silt fraction (2—10 μm) is discounted during analysis because these grains were more likely to have been deposited as aggregates with similar settling velocities as larger individual grains (McCave, 2008).

Size sorting occurs as a result of selective deposition primarily based on settling velocity (McCave, 2008). Some variables which determine settling velocity are the size, shape, and density of grains and aggregates, as well as the viscosity of the fluid in which they travel. During deposition, grains and aggregates of similar settling velocity fall through the boundary layer—the region of flow near the bed where speed decreases logarithmically due to drag forces with the bed. Many aggregates will be broken up by the intense turbulence near the bed, causing some component particles to be ejected back into suspension while others become trapped in the viscous sublayer. The viscous sublayer is the region of flow nearest the bed were flow is laminar, speed approaches 0 cm/s, and viscous forces dominate. Because the viscous sublayer will reject some component grains while retaining others, there is a substantial overlap in the grain-size population of any given deposit. While there will be a pronounced mode in the distribution related to the speed of the depositing current, the overall fine-grained sediment distribution is generally poorly sorted due to the effects of aggregation (McCave and Hall, 2006). This is another reason that it is important to eliminate the cohesive (<10μm) fraction during analysis. Because clay and fine silts make up such a relatively large percentage of the overall composition of a deposit (Fig 4.3.), their inclusion skews the distribution towards the fines, and clouds the current sorted mode, which may lead to an interpretation of the depositing current being slower than it actually was.

4.2.2 Sediment supply and contourites

Sediment is delivered to the deep ocean either via downslope, gravity driven processes such as turbidity currents and debris flows along the continental margins, or by pelagic settling from the surface (McCave and Hall, 2006). Once there, intermittently strong bottom currents running transversely across topographic contours, resuspend and further transport the sediment until the current slows and deposition, largely controlled by settling velocity, occurs. Thus, an initially unsorted sediment package is progressively size-sorted through repeated resuspension, transportation, and deposition events along the path of geostrophic boundary currents.

Sediment focusing under long-term boundary currents produces contourites—large-scale drifts of fine-grained material which are typically 100's of km long, several 10's of km wide, and often >1 km thick (McCave, 2008). Sediment accumulation on such drifts is typically 5-20 cm/kyr, but can locally can be much higher. This sedimentation rate is well above the background pelagic accumulation rate of <2 cm/kyr. Because they are the products of bottom current activity, by definition the sediment grainsize record contained within contourites hold

a record of how the strength of the current has varied over time. This record, along with their high rate of sediment accumulation make contourites ideal targets of study for paleoceanographers who need records containing continuous, abundant accumulation of marine sediment in order to reconstruct detailed climate records with high temporal resolution (McCave, 2008).

Figure 4.3, from McCave and Hall's (2006) extensive review of the sortable silt proxy method, shows the hypothetical composition of an idealized contourite deposit, as well as the estimated speed of the depositing current. It should be noted that the limits on critical deposition and erosion speeds in drift deposits are poorly constrained, and $\overline{SS}$ itself has not yet been convincingly calibrated (McCave and Hall, 2006; McCave et al., 2017), so the flow speeds presented here are, at best, theoretical estimates.

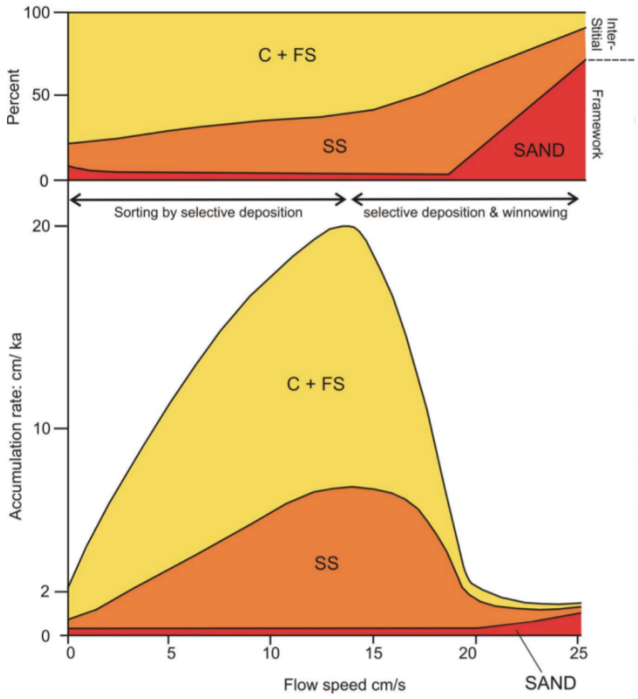

Figure 4.3. Hypothetical composition of drift material, showing increasing accumulation rate with increasing flow speed. Yellow fields indicate clay (C) and fine silt (FS). Orange fields indicate sortable silt (SS). Red fields indicate sand (McCave and Hall, 2006).

At 0 cm/s a pelagic rate of 2 cm/kyr is assumed. Accumulation increases with increasing flow speed up to a peak, here chosen as 13cm/s, after which, accumulation sharply drops off due to the current becoming strong enough to begin selectively eroding (winnowing) fines away, leaving coarse, sandy lags behind. Figure 4.3 further demonstrates that clay and fine silt (<10μm) are by far the largest portion of the drift composition. The sand fraction present in

contourite drifts is mostly foraminifera sand (McCave, 2008), and does not become mobile until flow increases to between 20-25 cm/s. These speeds are uncommon in bottom currents making sorted sand drifts relatively rare in the deep ocean. In short, sand and gravel sized material are essentially immobile at deep sea current speeds and are assumed to be a result of vertical flux, while the silt and clay fractions, which make up the bulk of the drift material are carried and sorted by lateral flux, that is, geostrophic currents.

4.2.3 $\overline{SS}$ Calibration

As mentioned, the $\overline{SS}$ proxy has not yet been definitively calibrated, so it can only offer information about the *relative* changes in current speed, not the exact magnitude of change. The method assumes a linear relation between $\overline{SS}$ and bottom current speed, with a given change in grain size corresponding to an absolute shift in flow speed. Some preliminary studies by, for example, Thornally et al. (2013) using long-term current-meter data near the seafloor, along with nearby core-top $\overline{SS}$, have convincingly demonstrated this linear relationship (Fig. 4.4a), which they furthermore used to infer flow speeds for individual sites. But little progress has been made in establishing a universal calibration applicable to all sites. Recently, McCave et al. (2017) made a first attempt at a universal $\overline{SS}$ calibration using current-meter and core-top data from widely dispersed locations and depths throughout the Atlantic Basin.

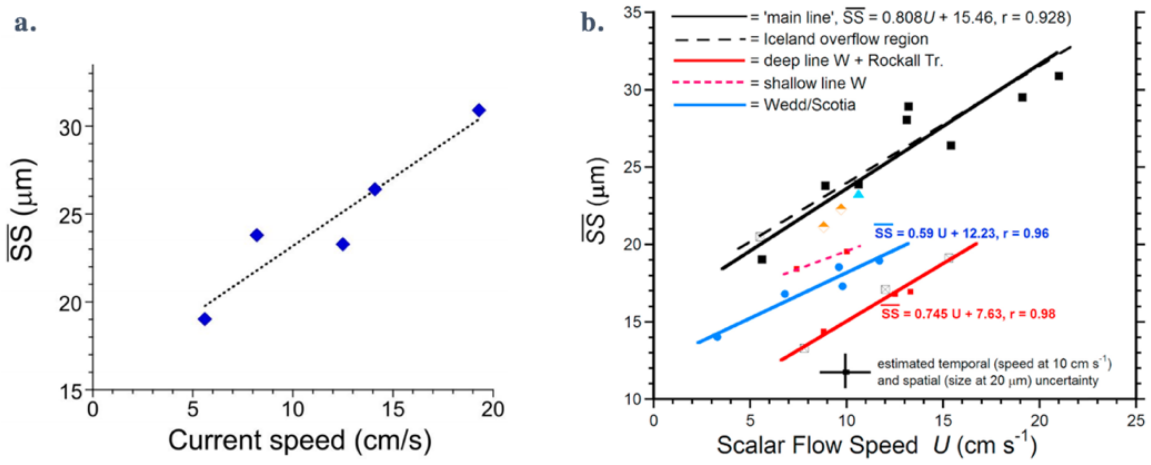

Figure 4.4. (a) Core-top $\overline{SS}$ calibration for the north Ireland Basin (Thornally et al. 2013). (b) Core-top $\overline{SS}$ calibration for multiple depths and locations. Sub-parallel slopes for all locations suggests an absolute sensitivity of $\overline{SS}$ to flow speed (McCave et al. 2017).

The strong linear relationship was upheld for all sites, but there appears to be location specific offsets (Fig. 4.4b) which may be the result of progressive downstream fining of deposits as

coarser grains are deposited from the stream early along the transport path. However, the similarity of the slopes between each of the McCave et al. (2017) datasets suggest an absolute sensitivity of $\overline{SS}$ to changes in flow speed which may eventually be applied to calibration.

4.2.4 Particle Measurement

There are several different types of instruments available to carry out sortable silt analysis in the laboratory, each of which measure grain size according to fundamentally different techniques and principles. Two examples that are well suited to the analysis of marine muds are the Sedigraph and the Coulter Counter. The Sedigraph uses Stoke's Law regarding drag force acting on a sphere falling through a viscous fluid (i.e. settling velocity). It measures the grain size distribution of a sample in suspension by passing an X-ray beam through it to count the rate at which particles fall through the beam. The Coulter Counter, on the other hand, is an electroresistance size analyzer in which particles are suspended in an electrolyte solution, and then pulled through an aperture where they displace their own volume of solution. In this way, the number and volume (i.e. size) of particles held in suspension is counted. The primary difference between these two instruments is that whereas the Sedigraph counts the whole size distribution settling through its x-ray beam, the Coulter Counter operates using a defined detection window, counting only those particles which are roughly 2-50% the size of the diameter of the aperture used for analysis (McCave and Hall, 2006). If the Coulter Counter is set to detect particles between, for example, 8 to 100 μm, it essentially ignores all of the finest silt and clay which may be a substantial portion of the size distribution, thus yielding a coarser mean size. Nevertheless, studies comparing results of the two instruments (e.g. Bianchi et al., 1999; McCave et al. 2017) show very good agreement between them, so their results are considered reliable and easily comparable. The machine used to produce the data for this thesis is the Beckman Coulter Multisizer™ 3 Coulter Counter®. It was chosen because it is relatively easy to operate, requires smaller amounts of sample for each run, and, as mentioned above, has been shown to yield reliable, accurate results. The analytical precision of the Multisizer 3 Coulter Counter is reported at 1-4% (Bianchi et al., 1999).

4.3 Chronology

In order to glean more detailed information about the rate and duration of flow speed changes, it is helpful to plot down core $\overline{SS}$ variability against age as well as depth. This practice also allows for easier comparison with other records for the purposes of later discussion. For

convenience, I have chosen to use the age model previously established for Site U1304 by Galaasen et al. (2014). The Galaasen et al. (2014) model was, in turn, based on the age model for Marine Isotope Stage (MIS) 5e established by Shackleton et al. (2002, 2003). Using benthic $\delta^{18}O$ data from sediment core MD95-2042 (37°48' N, 10°10' W; water depth, 3146 m), and correlating it to radiometric (U-series) age estimates of coral terraces that grew during the LIG sea level high stand, Shackleton et al. (2002, 2003) defined the "MIS 5e plateau" as the period of low, relatively constant benthic $\delta^{18}O$ values beginning at 128.0 kyr BP and ending 116.1 kyr BP. Galaasen et al. (2014) adopted these and several additional radiometrically determined dates as calibration points, and matched them to the benthic $\delta^{18}O$ signal from Site U1304. Two additional calibration points Galaasen et al. (2014) used are at 135.0 kyr BP and 113.0 kyr BP. The first, 135.0 kyr BP, marks the mid-point of the transition between high glacial and low interglacial benthic $\delta^{18}O$ values. This point, in the middle of the deglaciation, marks the end of MIS 6 and the beginning of MIS 5e. The final calibration point is at the mid-point of the transition from low, interglacial benthic $\delta^{18}O$ values to relatively higher values. It marks the beginning of the MIS 5d stadial at 113.0 kyr BP.

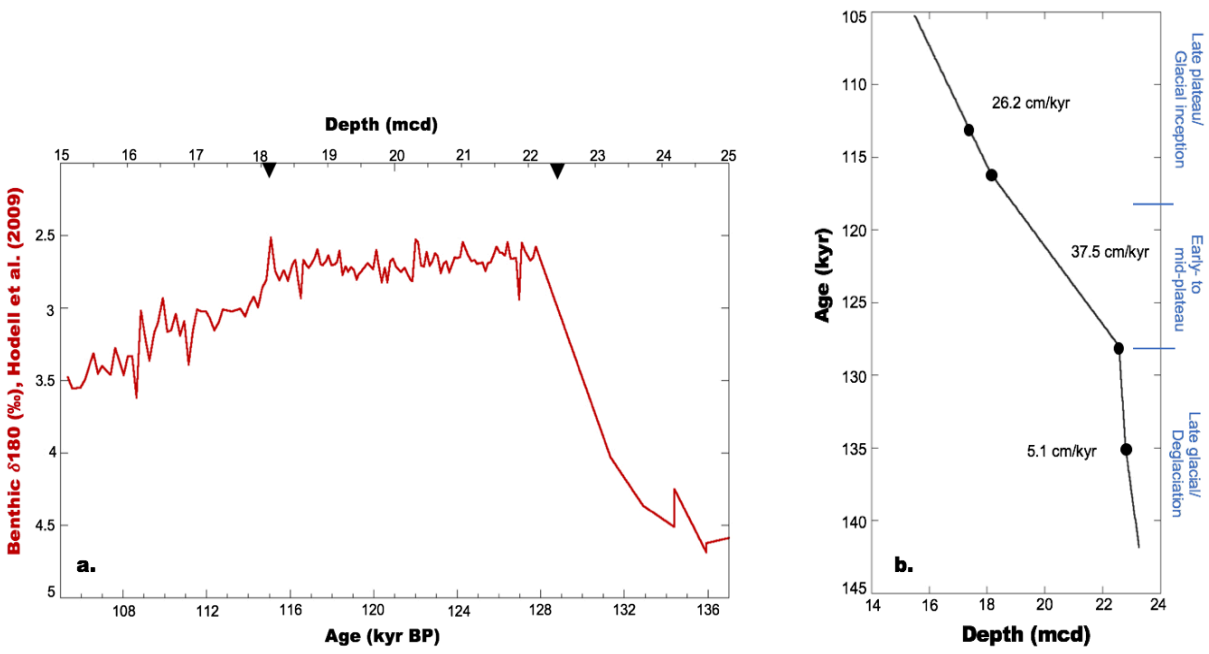

Figure 4.5. (a) Revised age model after Galaasen et al. (2014), showing the Site U1304 benthic $\delta^{18}O$ record from Hodell et al. (2009) plotted against age (kyr BP) and meters composite depth (mcd). The black triangles indicate the depth in the core which corresponds to the beginning and end of the MIS 5e benthic plateau, 22.56 and 18.12 mcd respectively. (b) Depth (mcd) versus age (kyr BP) plot for Site U1304 showing tie points (black dots) used in the revised age model, and sedimentation rates.

4.4 Laboratory Methods

All laboratory work for this thesis was done at EARTHLAB (Earth Surface Sediment Laboratory) at the Department of Earth Science, University of Bergen. The work was carried out over a 7-month period, from October 2017 to May 2018.

4.4.1 Sample Selection

As stated in Chapter 1.2, one of the primary objectives of my thesis is to produce a high resolution $\overline{SS}$ record spanning the peak of the last interglacial when average summer temperatures were high and global ice volume was at its lowest (Otto-Bleisner et al., 2006). To this end, the interval of core U1304A spanning the early-to mid- MIS 5e $\delta^{18}O$ plateau (from 22.54 to 19.3 mcd in Fig. 4.5b) was sampled every 4 cm (82 samples). Although the mean interglacial sedimentation rate at Site U1304 was reported by the cruise report (2006) as 40 cm/kyr, the refined age model above results in a sedimentation rate of 37.5 cm/kyr giving an average sampling resolution of 106 years for this interval.

Additional samples were acquired at a reduced resolution from the transitional periods into and out of the main plateau (i.e. deglaciation and glacial onset). Ten samples from the interval spanning the late MIS 5e plateau and early glacial onset (from 18.9 to 15.5 mcd) were sampled every 40 cm. The refined age model yields a sedimentation rate of 26.2 cm/kry giving a mean sampling resolution of ca. 1500 years for this section. Likewise, the late glacial/deglacial interval (from 23.23 to 22.57 mcd) was sampled at 22 cm intervals (four samples). The refined age model for this interval results in a sedimentation rate of 5.1 cm/kyr giving a sampling resolution of roughly 4,300 years. It is interesting to note here, that the calculated sedimentation rate for the deglacial interval is significantly lower than the mean sedimentation rate of 15 cm/kyr presented in the expedition report (Expedition 303 Scientists, 2006). Possible reasons for this significantly reduced sedimentation rate will be discussed in Chapter 6.

4.4.2 Sample Preparation

The process of preparing sortable silt samples for analysis involves a sequence of chemical digestion baths to remove biogenic carbonate and silica. It is a time-consuming process due to the necessity of allowing sediment solutions to resettle up to 24 hours between each step. The standard laboratory protocol when preparing sediment samples for sortable silt for analysis was laid out by McCave et al. (1995). Given the known presence of diatom mats at Site U1304 (Ch.

4.1), and the likelihood of a biogenic opal content >>5%, extra steps were added to ensure the removal of all biogenic silica. Biogenic components tend to carry a species-specific size mode which may mask the current sorted mode of the terrigenous material (McCave and Hall, 2006), therefore it is critical that as much of the biogenic signal as possible be removed before analysis.

The bulk fine fraction samples were delivered to me already wet sieved with the coarse, >63 μm fraction removed. The first step, then, was to crush each sample with a mortar and pestle in order to homogenize the mud and break up any large clumps or aggregates that may have formed during drying time after wet sieving. Between 3 to 3.5 g of each sample was then measured into conical flasks and treated twice with a 1 M acetic acid solution in order to dissolve any biogenic carbonate. The decarbonated samples were then rinsed with deionized water and left to settle. To remove biogenic silica, the samples were treated with a 2 M sodium carbonate ($NaCO_3$) solution and placed in a water bath at 85°C for 5 hours. During this time each sample was vigorously stirred three times in order to stimulate silica dissolution.

Because half of my samples were taken from an interval of the core (above 20.5 mcd) identified by Hodell et al. (2009) as being particularly diatom rich, extra $NaCO_3$ baths were necessary. Smear slides of randomly selected samples were prepared before and after each bath, and the percentage of silica content was assessed through microscopic examination (Figs. 4.6 a-d). After three $NaCO_3$ baths, all but the most refractory silica in the diatom-rich samples had been removed, and visual inspection of the smear slides showed silica content to be generally <5%, though a few large needles clearly remained in some cases. All samples taken from above 20.74 mcd were treated with three $NaCO_3$ baths, and all samples below were treated with two baths. After desilication, the samples were rinsed twice with deionized water in order to fully neutralize the sodium carbonate solution, then transferred into 60 mL Nalgene bottles and suspended in a 0.2% Calgon solution. Samples were stored in a refrigeration unit until ready for analysis.

4.4.3 Grain Size Analysis

Once the chemical digestion process was completed for all samples, I was able to begin analysis with the Coulter Counter. My samples were run in random order over the course of several weeks. Each sample was run a minimum of three times, though some were run four to six times if the precision within the sample replicates appeared to be poor, >1μm. To ensure complete disaggregation, the samples were agitated on a rotating carousel for 24 hours, and then treated

in an ultrasonic bath for 3 minutes immediately prior to analysis. The Coulter Counter's aperture size was set for 140 µm with a minimum sizing threshold of 8 µm, and a total of 70 000 particle counts per run. In addition, the program was set to export the mean value of the differential volume of all particles counted. This is the number reported in Table A.1 of the Appendix. Prior to each testing session, a 20 µm latex bead standard was run to ensure the instrument was functioning properly. There were no obvious problems with the functionality of the Coulter Counter during the course of my analysis.

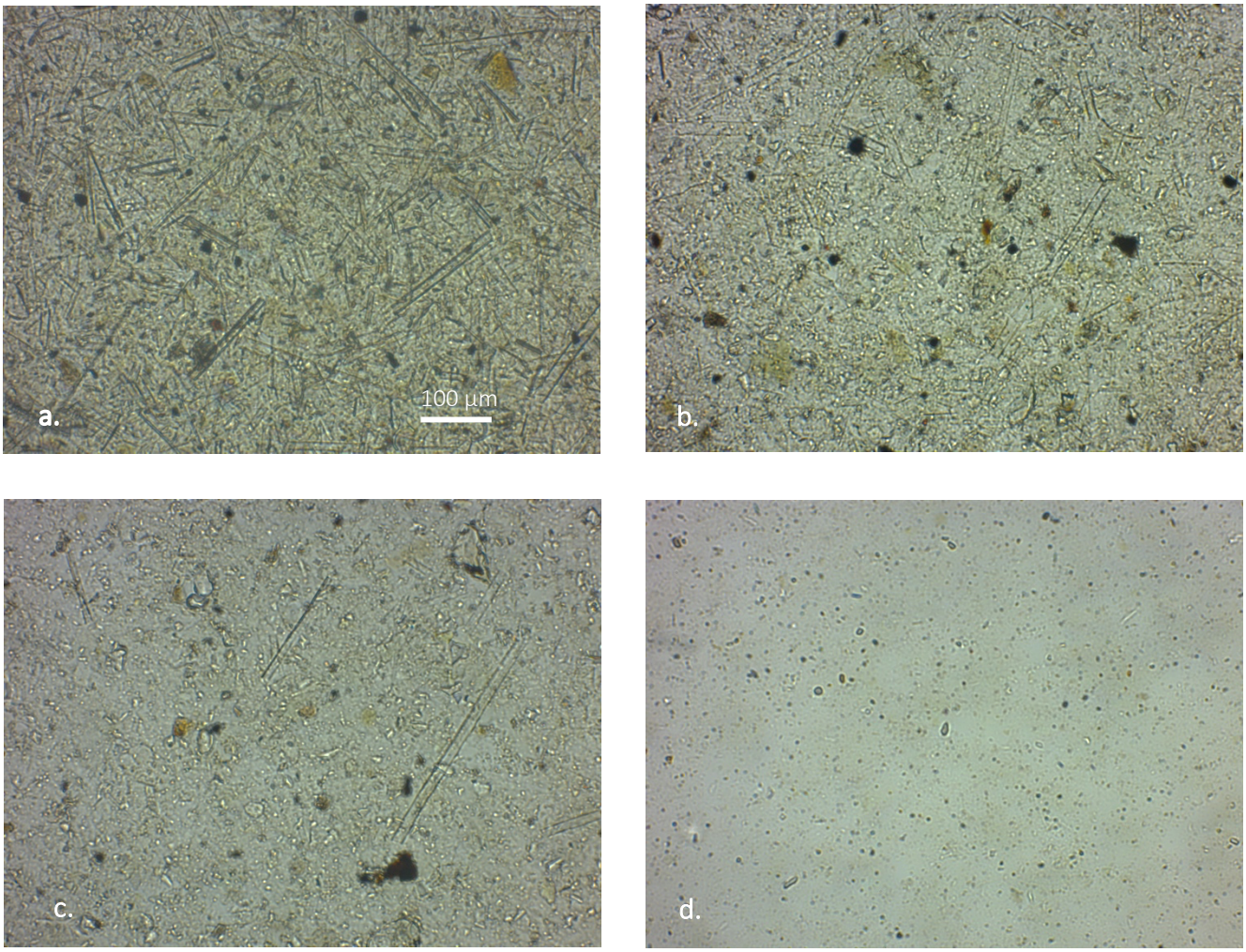

Figure 4.6. The progressive dissolution of biogenic silica. This sample, 2H-4, 76-78 cm (19.78 mcd) was randomly selected from within the diatom-rich interval identified by Hodell et al. (2006). (a) Before desilication, diatom spicules dominate the field of view. The relative volume of biogenic silica is estimated at >25%. (b) After the first $NaCO_3$ bath, spicules appear finer and more fractured, but the relative volume is still >10%. (c) After the second $NaCO_3$ bath, the relative volume of silica appears to be <5%, but several very large spicules capable of skewing the current sorted size distribution remain. (d) After the third $NaCO_3$ bath, biogenic silica has been satisfactorily eliminated, though some samples (not shown) did show some refractory silica remained even after three chemical digestion baths. All images were taken with a 40x objective lens.

For each run, the Coulter Counter's beaker was filled to a predetermined level with fresh electrolyte solution (Isoton®). Then between 100 to 300 mL of sample was drawn from the Nalgene bottles using a pipette and added to the Isoton. The amount of sub-sample added varied because some samples, particularly those in the diatom-rich interval, were more diluted than others, and required a larger sub-sample size to achieve the desired suspended sediment concentration—ideally 2%. During analysis, particles are held in suspension for the duration of each run by a glass stirrer submerged in the electrolyte. Care must be taken to ensure that the stirrer speed is high enough to prevent settling but not so high as to cause turbulence and bubbles to develop. Small bubbles drawn down into the solution may be pulled into the aperture and counted by the machine as a particle, thus skewing the size distribution towards the heavy end, and masking the true current sorted mean. Bubble entrainment posed a particular challenge during analysis. Especially early on, many runs had to be stopped and restarted upon noticing bubbles had developed half-way through the count. However, through experimentation, I found that keeping the stirrer speed at 42, and allowing all bubbles to clear the beaker before adding the subsample to the electrolyte adequately suppressed bubble entrainment. After each run was complete, the beaker was rinsed with electrolyte, and the process was repeated.

4.5 Sources of Error

I will address the analytical and statistical uncertainties associated with the $\overline{SS}$ data in Chapter 5. Here I present potential sources of error associated with the preparation and handling of the samples before and during analysis.

- Each step in the chemical digestion process required the removal of supernatant liquid using a vacuum aspirator. During this procedure it was difficult to avoid losing some sample fines to the vacuum as the liquid level over the sediment fell. Although the sediment lost was likely clay from the finest fraction (<10 μm), and the amount lost was miniscule compared to the overall sample, it is impossible to be certain exactly what was removed. Given the small amount that was lost it is unlikely that this in an important source of error.
- Even after three sodium carbonate baths, persistent diatom spicules remained in some samples. Because the spicules were very large relative to the current sorted sediment, any significant amount of refractory silica (i.e. large enough to influence the results) would have been clearly identifiable in the coarse end of the distribution curves of the

raw data. No such signal was observed in the raw analytical data, even for those samples where precision between replicates was poor. Therefore, it is unlikely that refractory diatoms were a factor in my results. However, my experience suggests that the standard preparation procedure (McCave et al. 1995) for the removal of biogenic opal may be inadequate for sites where diatom abundances are known to be high, and that future studies might find it beneficial to look for stronger, more efficient methods of opal removal. At a minimum, my findings show that careful post cleaning assessment using smear slide observations should be recommended as a prerequisite for $\overline{SS}$ studies on biogenic opal bearing sediments.

- Lack of experience in running the Coulter Counter may also have contributed to poor precision in the sample replicates. Early efforts to control bubble entrainment meant that the stirrer speed was adjusted often during measurement. This inconsistent stirrer speed may have had some consequence for the mean value of some replicates. However, this would only have been an issue in the first two days of testing, and since samples were run multiple times in random order, the potential error is likely minimal. No systematic offsets were observed between the mean of the analyses run on those days versus those replicates run later.
- A final potential source of error is variability in the timing and depth of subsampling with the pipette. The Nalgene bottles were shaken by hand just prior to each subsampling, but because sediment begins to settle instantly, any variability in the time it took to collect the sample, or the depth at which it was drawn, could have altered the mean grain size of the subsampled sediment. However, the variations due to sampling variability are included in, and contribute to the empirical analytical uncertainty determined from the replicates.

5. RESULTS

In this chapter I present the results of the mean sortable silt grain size analysis, as well as a new, multi-proxy record of concurrent changes in dynamical and chemical water mass properties over Site U1304 during the study period. The raw data behind the $\overline{SS}$ graphics in this chapter are included in Appendix A.

5.1 $\overline{SS}$ results for Site U1304

Figure 5.1 shows the results of the $\overline{SS}$ analysis plotted against core-depth. The data points (red, green, purple, and orange symbols) are the results of the individual measurements for each sample, while the solid blue line is the arithmetic average of all measurements for each sample. All samples were measured at least three times, while some samples were measured four to six times where reproducibility was poor (i.e. where values varied more than 1 µm from each other). All replicates are included in the calculations for sample means (solid blue line) and standard deviation. Thus, the error bars attached to the average values indicate the standard error calculated for the complete data set. Here the average standard deviation is ±0.71 µm, while the average standard error is ±0.41 µm for the first three replicates (see Appendix B for calculation).

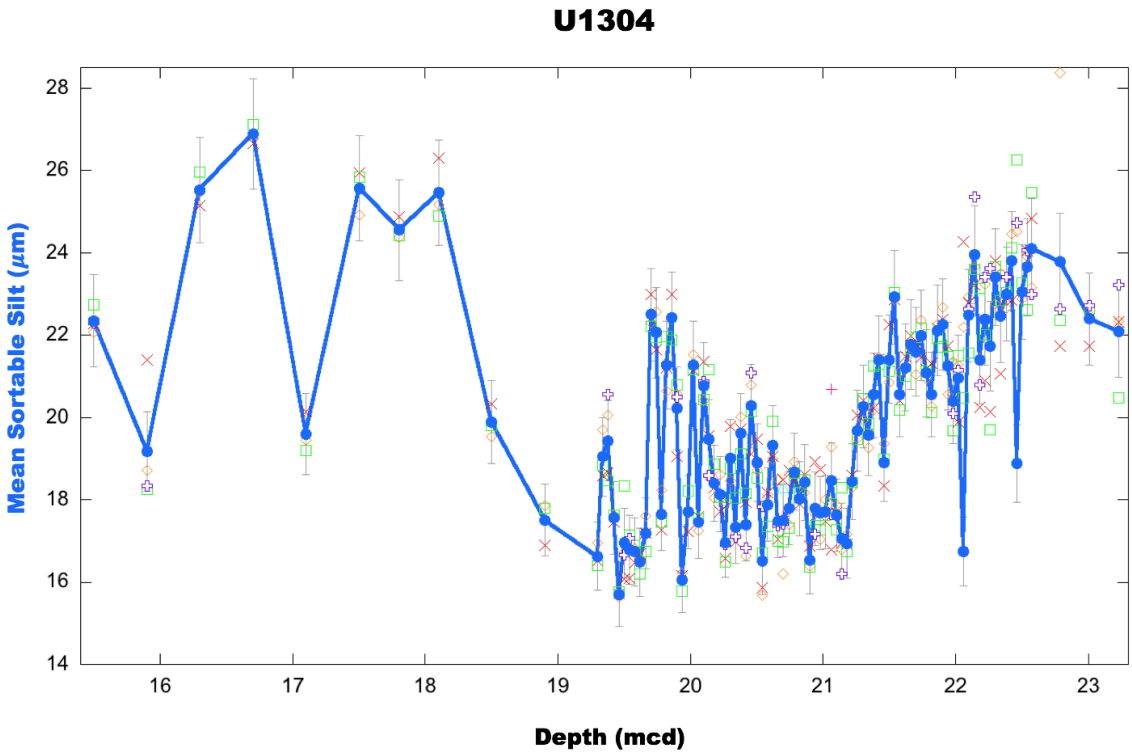

Figure 5.1. Mean sortable silt results for Site U1304 plotted against meters composite depth (mcd). The solid blue line is the arithmetic average of the sample replicates. See text for further explanation.

Reproducibility in the first three sample measurements is generally acceptable with the data spread mostly contained within the error bars. However, some obvious outliers are evident at the top and bottom of the core (i.e. those intervals corresponding to the transitions into and out of the peak MIS 5e benthic $\delta^{18}O$ plateau). In general, more samples from this interval required extra replicates in order to improve precision in the measurements. Since the oscillations in the record are larger than the calculated error, and show a consistent, coherent pattern, it is likely that the $\overline{SS}$ changes reflect flow speed variability over the site rather than noise or random fluctuations.

Figure 5.2 shows the results of the $\overline{SS}$ grain size analysis again, but in this figure the measurement averages (light blue) have been smoothed with a three-point running average (dark blue) in order to highlight lower frequency variability and emphasize the broader trends in the signal. As explained in Chapter 4.2, the $\overline{SS}$ paleocurrent proxy is loosely a qualitative proxy which relates information about *relative* changes in current speed through time; it has not yet been calibrated, and cannot assign an absolute magnitude to down core grain size variability. The median value of the $\overline{SS}$ grain size for this record is 20.0 µm (dashed line). Thus, $\overline{SS}$ values above this median reflect relatively vigorous flow, and $\overline{SS}$ values below reflect relatively sluggish flow.

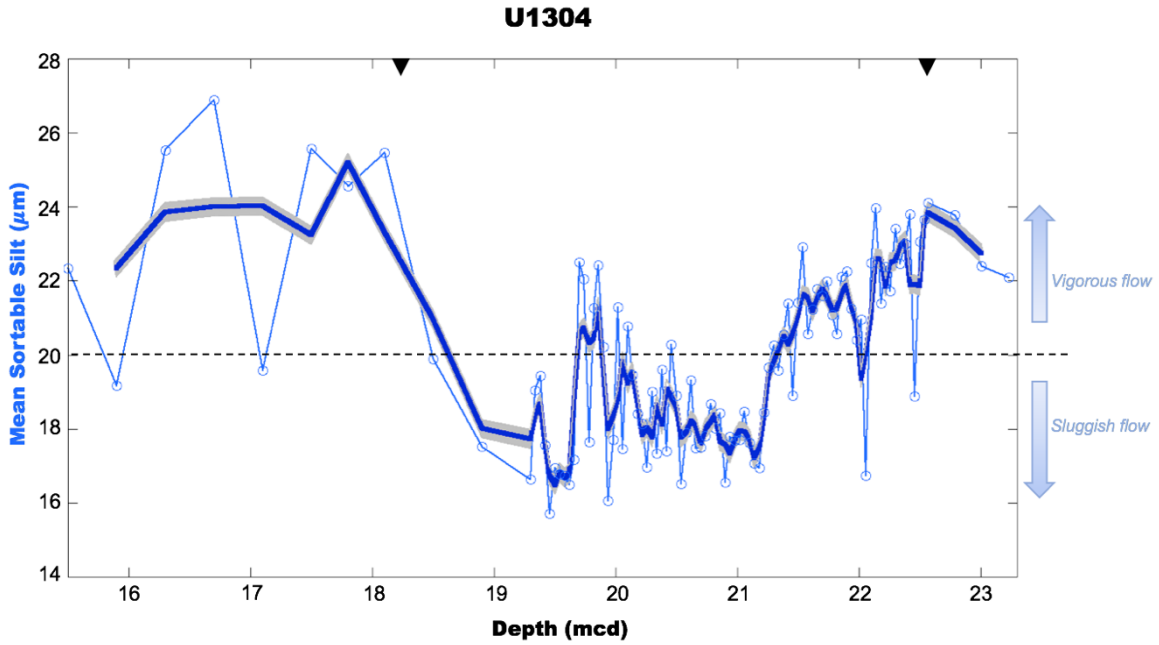

Figure 5.2. Mean sortable silt variability at Site U1304 plotted against depth. The light blue line is the arithmetic average of all sample measurements, while the thicker, dark blue line is a 3-point running average of the mean. The grey reflects the standard error of the running average, here ±0.24 µm. The dashed line indicates the average median value, 20.02µm. The black arrows indicate the interval corresponding to the beginning and end of the benthic $\delta^{18}O$ MIS 5e plateau, 116.1 and 128.0 kyr BP respectively.

Figure 5.3 shows a blow-up of the record between the black arrows in Figure 5.2. This interval corresponds to the benthic $\delta^{18}O$ plateau at Site U1304 (Fig 5.2.1) which defines the MIS 5e interglacial (Shackleton et al. 2002, 2003). As discussed in Chapter 4.4.1, I have further divided the MIS 5e into three sub-intervals in order to facilitate interpretation and discussion of the data. These sub-intervals are: the early interglacial (22.56 to 21.18 mcd, ~128—124 kyr BP); the middle, or peak interglacial (21.18 to 19.34 mcd, ~124—119 kyr BP); and the late interglacial (19.34 to 18.12 mcd, ~119—116 kyr BP).

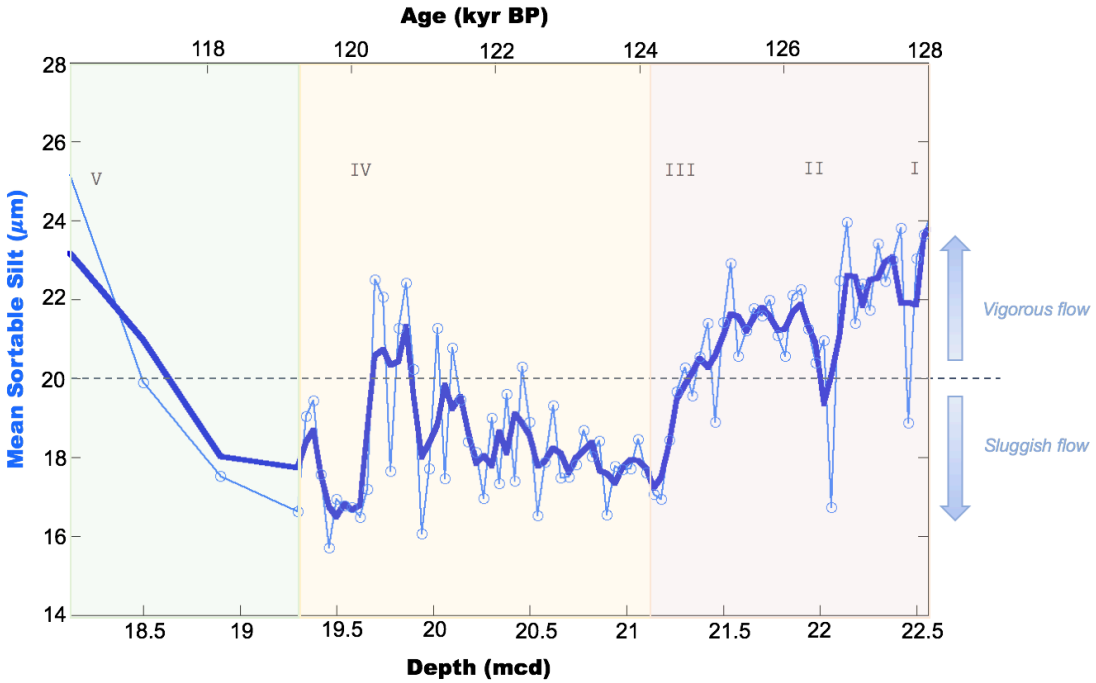

Figure 5.3. Close-up of the interval between the black arrows in Figure 5.1.2 showing mean sortable silt variability at Site U1304 during MIS 5e benthic plateau, plotted against both depth and age. The light blue line is the arithmetic average of all sample measurements, while the thicker, dark blue line is a 3-point running average of the mean. The shaded regions correspond to early- (orange), peak- (yellow), and late- (green) interglacial plateau. The Roman numerals denote exceptional excursions in the $\overline{SS}$ signal. See text for details.

There are only four data points from the lowest studied section of the core (22.57 to 23.23 mcd, not included in Figure 5.3), and sampling resolution is only ~4300 years (Ch. 4.4.1) which is not high enough to resolve any abrupt, short-term variability. Nevertheless, Figures 5.1 and 5.2 would suggest that flow speed was relatively vigorous and increasing at Site U1304 throughout this interval corresponding to deglaciation, and leading into the early interglacial.

The overall trend of relative flow speed in the interval corresponding to the early interglacial (22.56 to 21.18 mcd, shaded orange in Figure 5.3) is characterized by steady deceleration. Here, sampling resolution is high (~106 years), and a pattern of persistent, centennial-scale variability superimposed over the generally declining trend is plainly evident. The $\overline{SS}$ variability between adjacent data points is generally less than 2.0 μm, however, there are three notably larger, abrupt decelerations and recoveries. The first two excursions (marked I and II on Figure 5.3) are roughly similar in magnitude—4.2 μm and 5.7 μm respectively—and last the same amount of time—8 cm from deceleration to recovery, or, given a sedimentation rate of 37.5 cm/kyr (Fig. 4.5b), ~200 years. The third excursion (marked III on Figure 5.1.3) is characterized as an abrupt deceleration without recovery. Mean grain size falls rapidly by 3.3 μm during excursion III, then begins a slow steady incline into the middle interval of the studied core section.

The overall trend in the mid-interval section corresponding to peak interglacial warmth (21.18 to 19.34 mcd, shaded yellow in Figure 5.3) is one of steady acceleration in relative flow speed. The same pattern of persistent, centennial-scale variability superimposed over the broader trend continues. However, here the duration of each oscillation from deceleration to recovery is longer—16 cm, or ~430 years. Additionally, the magnitude of variability between adjacent data points is larger than it was for the early interglacial interval, and appears to increase gradually with time. For example, a typical centennial-scale oscillation early in this interval (20.94 to 20.86 mcd) shows an increase in mean grain size of 1.9 μm, while one from near the end of the interval (19.94 to 19.86 mcd) shows an increase of 6.4 μm. This latter oscillation is the single largest in the record, and may be considered an exceptional excursion in its own right, except that it fits well within the general trend of increasingly high magnitude flow speed variability observed throughout this interval. This is especially evident in the three-point running average of the signal, which, by removing some of the uncertainty associated with individual measurements, tempers the seeming extremism of the oscillation.

The peak interglacial trend towards increasing flow speed which began at 21.18 mcd, abruptly ends at 19.70 mcd (marked as excursion IV on Figure 5.3) with a 5.3 μm fall in mean grain size. From here, flow speed falls further, and mean grain size reaches a minimum of 15.7 μm at 19.46 mcd. There is one last minor oscillation (19.46 to 19.30 mcd) before flow speed begins to steeply accelerate through the late interglacial (shaded green in Figure 5.3) and into the

interval corresponding to glacial inception (i.e. the transition into benthic $\delta^{18}O$ substage MIS 5d).

The final, distinctly steep transition in the $\overline{SS}$ record (marked V on Figure 5.3) occurs at the end of the late interglacial interval (18.90 to 18.10 mcd). Here mean grain size is observed to increase 8μm over 80 cm, or, assuming a sedimentation rate of 26.2 cm/kyr for this interval (Fig. 4.3.2), ~3000 years. Because of diminished sampling resolution in this uppermost studied section of the core, it is impossible to resolve the same degree of variability observed in the early- and middle- interglacial intervals. However, Figures 5.1 and 5.2 suggest that some degree of millennial-scale variability persisted, while the general trend was one of relatively stable vigorous flow. $\overline{SS}$ values reach maxima during this interval (26.9 μm at 16.70 mcd), and even the few resolved negative excursions in flow speed are, in general, relatively higher during this transitional climate phase than they were during the peak interglacial (Fig. 5.2).

In summary, the $\overline{SS}$ results for Site U1304 reveal significant flow speed variability over the site throughout the last interglacial period. The long-term trends spanning the entire studied interval are best highlighted by a three-point running average of the mean (Figs. 5.2 and 5.3). At the beginning of the MIS 5e interglacial plateau (128 kyr BP), flow speed is relatively vigorous, but gradually decelerates over the course of ~4000 years. After a precipitous decline at ~124 kyr BP, flow speed gradually recovers, accelerating for ~4000 years through the peak of the interglacial plateau. At ~120 kyr BP, a second steep decline causes flow speed to slow to its most relatively sluggish speed before rapidly accelerating at the end of the MIS 5e interglacial, and remaining relatively vigorous as climate conditions deteriorate into colder, MIS 5d stadial conditions. A persistent pattern of abrupt, centennial scale variability is superimposed over these longer trends, with short-term oscillations tending to increase in both duration and magnitude towards the peak of the interglacial.

5.2 A new multi-proxy record for Site U1304

One of the primary objectives of this thesis is to reconstruct deep ocean circulation changes over Site U1304 during the last interglacial. To that end, I have presented here a new $\overline{SS}$ record for the site. However, on its own, the $\overline{SS}$ proxy is limited in what it can reveal about the combined variability of the water column properties and circulation patterns over the site. $\overline{SS}$ is a physical proxy that provides valuable information about relative changes in the speed of deep

ocean currents through time. But, for example, where $\overline{SS}$ results may infer flow rate changes, they cannot tell us whether it was the same water mass that sped up or slowed down. Nor can they reveal any information about changes in the chemical properties of the water itself. For that, $\overline{SS}$ results must be paired with a geochemical proxy from the same core that can provide additional information about temporal changes in the chemistry and/or distribution of water masses over the site. Thus, in order to further constrain the information about flow speed changes provided by the new $\overline{SS}$ record, I now combine my $\overline{SS}$ data with existing data from Hodell et al. (2009), and present a new, multi-proxy reconstruction of both flow speed variability and water mass properties over Site U1304 during the LIG. Benthic $\delta^{18}O$ from the same Hodell et al. (2009) record is included as a means of graphically illustrating the change in ocean chemistry that define the beginning and end of the MIS 5e interglacial.

5.2.1 A brief overview of the $\delta^{13}C$ proxy

$\delta^{13}C$ of dissolved inorganic carbon (DIC) is the most common proxy used to reconstruct large-scale, deep-water circulation patterns and water mass geometry. $\delta^{13}C$ refers to the ratio of the two dominant stable carbon isotopes dissolved in sea water ($^{13}C/^{12}C$). This ratio is essentially 'recorded' by foraminifera when they use dissolved CO_2 to build their calcite shells.

The primary mechanisms causing whole-ocean $\delta^{13}C$ variability are the take up and release of isotopically light carbon by marine organisms, and the mixing of water masses along their flow path (Curry and Oppo, 2005). The two principal water masses that form in the Atlantic basin are North Atlantic Deep Water (NADW) and Antarctic Bottom Water (AABW). These water masses obtain their unique, preformed $\delta^{13}C$ signatures through different processes. The ultimate source of NADW is the warm, saline surface currents flowing poleward out of the subtropics. Plentiful biological productivity in these waters leave them stripped of nutrients and strongly enriched in $\delta^{13}C$ by the time they arrive at the arctic where they lose heat and become dense enough to sink. AABW, on the other hand, derives from upwelling processes in the Southern Ocean where nutrient-rich, $\delta^{13}C$-depleted bottom-waters arrive at the surface, and almost immediately become dense enough to sink again through heat loss and brine rejection without enough time for biological activity or sea-air CO_2 exchange to alter its strongly depleted $\delta^{13}C$ signature (Duplessy et al 1988).

In summary, NADW tends to have geochemical signature which is nutrient poor but ^{13}C enriched (i.e. high $\delta^{13}C$ values), while AABW tends to be enriched in nutrients but depleted in ^{13}C (i.e. low $\delta^{13}C$ values). By analyzing $\delta^{13}C$ as preserved in benthic and planktonic foraminifera, these unique signatures can be used to reconstruct changes in the presence and distribution of NADW and AABW through time.

5.2.2 Deep water flow speed and chemical properties at Site U1304

The composite section of Site U1304 analyzed by Hodell et al. (2009) (24.52 to 15.47 mcd) corresponds to the MIS 6 through MIS 5d intervals, roughly the same interval covered by my $\overline{SS}$ data. The Hodell et al. (2009) study cites an average sampling frequency of ~125 years throughout the entire studied section, providing a high-resolution reconstruction of down core variability in water mass properties for the period. Hodell et al.'s (2009) results of the oxygen ($\delta^{18}O$) and carbon ($\delta^{13}C$) isotope analysis for the epi-benthic foraminifera, *Cibicidoides wuellerstorfi*, are shown together with my $\overline{SS}$ results in Figure 5.4.

Benthic $\delta^{18}O$ (Fig. 5.4a) reaches a distinct glacial maximum (4.85‰) near the end of MIS 6 before rapidly decreasing across the MIS 6/5e transition. MIS 5e is defined by the beginning and end of a near constant interglacial $\delta^{18}O$ low value of ~2.60‰. This distinct plateau persists for nearly 5 m of the core section before rising sharply by 0.3‰, then beginning a generally steady increase into MIS 5d.

The benthic $\delta^{13}C$ signal from Site U1304 (Fig. 5.4c) is characterized by persistent, centennial-scale variability. However, some coherent trends are discernable. The late glacial/deglacial interval (~134 to 128 kyr BP) shows a particularly strong pattern of high frequency, high magnitude variability. After a brief trend of increasing maxima between ~130 to 129 kyr BP, $\delta^{13}C$ begins to decrease into the MIS 5e benthic plateau. This trend towards lower $\delta^{13}C$ values throughout the early interglacial (128 to 124 kyr BP) mirrors the similarly timed decreasing trend in $\overline{SS}$. In addition, the first two strong, negative excursions in the $\overline{SS}$ signal (marked I and II in Fig. 5.3) are coeval with two distinct $\delta^{13}C$ minima (-0.14 and -0.30 ‰) during this interval.

At ~124 kyr BP, $\delta^{13}C$ increases sharply from 0.16‰ to 1.02‰. This rapid increase in the presence of ^{13}C-enriched water over Site U1304 coincides with a rapid deceleration of flow speed over the site (excursion III on Fig 5.3). While $\delta^{13}C$ values remain relatively stable

(~0.5‰) until the end of MIS 5e (116.1 kyr BP), the $\overline{SS}$ trend is characterized by much more variability during this time. The steady increase in flow speed observed between ~124 and 119 kyr BP is not reflected in the $\delta^{13}C$ record, and while both signals decrease at ~119 kyr BP, the magnitude of the fall is drastically different. $\overline{SS}$ reaches its minimum value at this time and remains relatively low for ~1500 years, while $\delta^{13}C$ dips briefly to 0.09 ‰ and recovers within ~200 years.

At the MIS 5e/5d transition, $\delta^{13}C$ drops sharply by 0.8‰ (down to -0.3‰), but rapidly recovers. $\overline{SS}$, on the other hand, accelerates steeply and steadily over the MIS 5e/5d transition, and remains relatively high. There is a generally increasing trend in $\delta^{13}C$ during MIS 5d, and the signal reaches its maximum value (1.2‰) near the end of the studied interval.

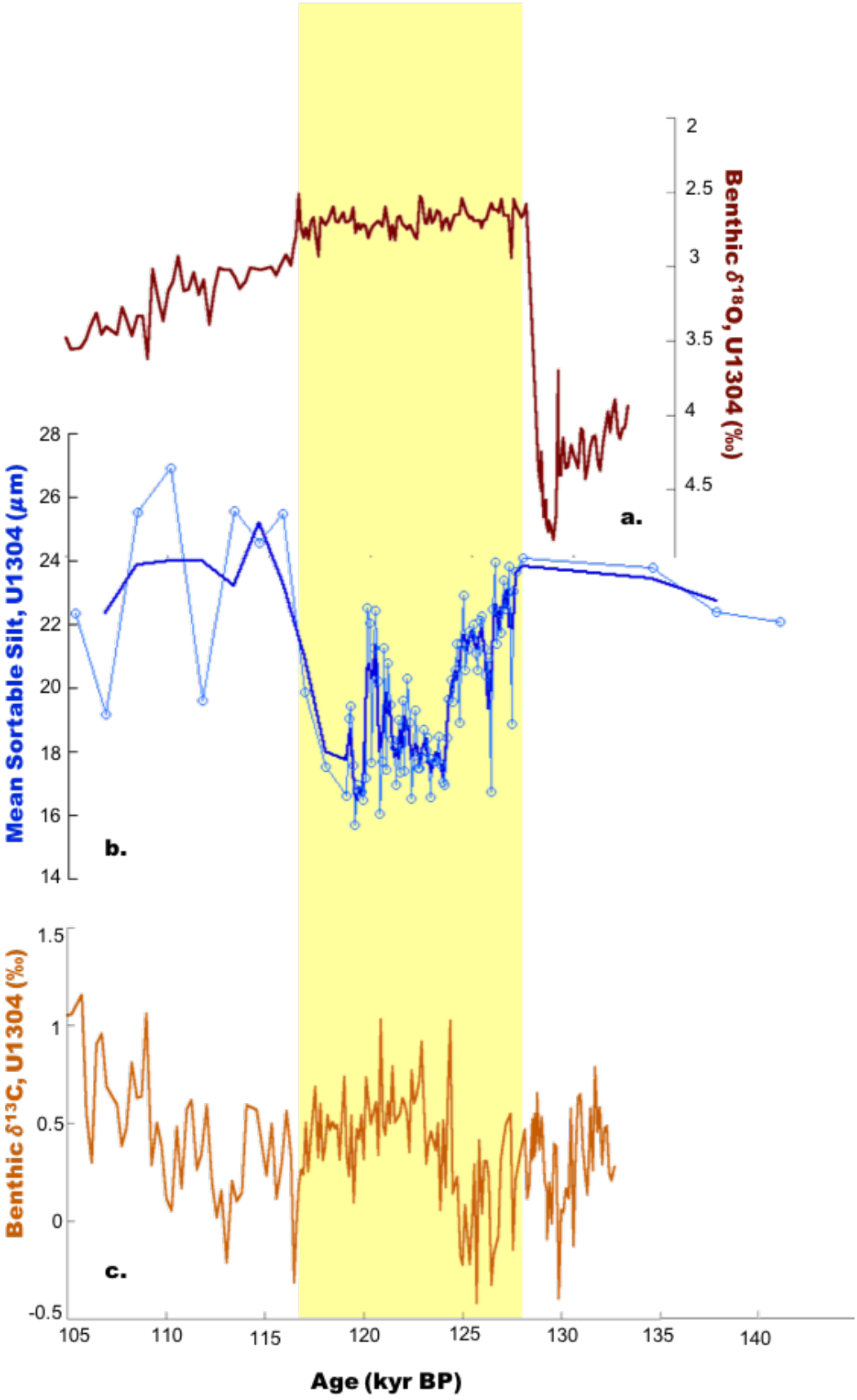

Figure 5.4. (a) Benthic $\delta^{18}O$ results for Site U1304, adapted from Hodell et al. (2009). (b) Mean sortable silt results for Site U1304 (this study) (c) Benthic $\delta^{13}C$ results for Site U1304, adapted from Hodell et al. (2009). The yellow field indicates duration of the benthic $\delta^{18}O$ MIS 5e plateau, 128.0 and 116.1 kyr BP.

6. DISCUSSION

In order to highlight periods of coherent variability in the deep water proxies, I have overlain the new sortable silt record for Site U1304 with Hodell et al.'s (2009) benthic $\delta^{13}C$ record in a single graph (Fig. 6.1). The most notable features of the new $\overline{SS}$ record are the two prominent plateaus of very high values preceding and postdating the peak interglacial interval. Between these plateaus, the $\overline{SS}$ signal is characterized by two gradual, but unambiguously opposite long-term trends indicating first a deceleration (decreasing grain size), and then an acceleration (increasing grain size) of bottom flow. Compared to $\overline{SS}$, $\delta^{13}C$ shows a tendency towards larger magnitude, short-term variability, but the maxima and minima $\delta^{13}C$ values appear to remain relatively similar over the long-term. These features of the new record will be the focus of the following discussion. I will explore possible reasons for the relatively high current speed during the glacial intervals, as well as discuss the significance of the apparent decoupling of the $\overline{SS}$ and $\delta^{13}C$ signals during the peak interglacial. I will conclude with some reflection on how my new data, highlighting changes in deep ocean circulation, further constrains and in some ways confirms our current understanding of climate evolution during the last interglacial.

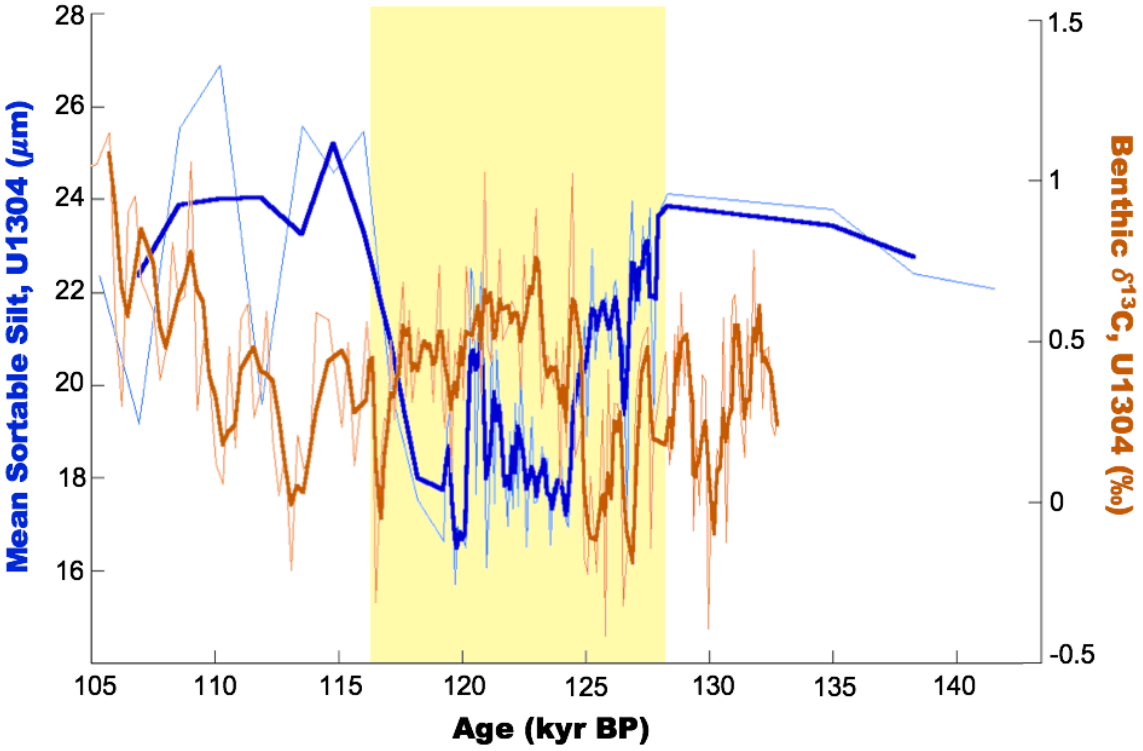

Figure 6.1. Mean sortable silt results (blue) overlain with benthic δ13C (orange) (Hodell et al., 2009) highlighting coincident trends and fluctuations in the proxies. The yellow field indicates duration of the benthic $\delta^{18}O$ MIS 5e plateau, 128.0 and 116.1 kyr BP.

6.1 Anomalously high deglacial and early glacial flow speed

As the primary focus of this thesis is to further constrain interglacial bottom current variability, the bulk of my data is concentrated in that interval. However, the high $\overline{SS}$ values which characterize the transitional climate intervals are such a striking feature of the final record, that some consideration must be given to their significance. Broadly speaking, the conclusions from a long catalogue of previously published paleocurrent studies employing the $\overline{SS}$ proxy agree on a consistent temporal pattern of relatively slower bottom current speeds during cold intervals and faster current speeds during warm intervals (e.g. Hall et al., 1998; Bianchi & McCave, 1999; Hall & McCave, 2000; Evans et al., 2007; Hodell et al., 2009; Deaney et al., 2017). For this reason, my results showing high early glacial and deglacial flow speeds at Site U1304 are somewhat unusual. These results are even more anomalous when viewed in light of the generally low $\delta^{13}C$ associated with the high glacial $\overline{SS}$ values in the new record (Fig. 6.1).

As previously discussed (Chapter 2.6), there are multiple studies documenting that a cold, glacial mode of ocean circulation is characterized by suppressed formation or shoaled deep-water (Fig. 2.6b). The reduced density of this glacial water mass results in slower bottom currents, reduced penetration of well ventilated, high $\delta^{13}C$ northern sourced water into the deep Atlantic, and a relatively stronger influence of poorly ventilated, low $\delta^{13}C$ southern sourced LDW bathing the North Atlantic. Theoretically then, this glacial circulation state should be identifiable in deep ocean sediment archives as coeval minima in $\overline{SS}$ and $\delta^{13}C$ proxies signifying sluggish or shoaled glacial bottom currents, and an increased contribution of southern sourced water to the abyssal North Atlantic. Instead, the new U1304 record is characterized by very high $\overline{SS}$ occurring with relatively low $\delta^{13}C$ minima at points in the record that would typically be associated with sluggish, southern sourced water. What could have caused this apparent decoupling?

If the new record is taken at face value, the observed low $\delta^{13}C$ would imply that Site U1304 is influenced by poorly ventilated LDW during the deglacial, and that the high $\overline{SS}$ values are recording an accelerated LDW current over the site. This scenario would further imply that the canonical idea of strongly reduced and/or shoaled glacial ISOW production was associated with a strong increase in not only the volume but also the speed of southern sourced LDW entering the North Atlantic. However, given the fact that Site U1304 is not located anywhere near a direct pathway of northward flowing LDW (Fig 3.1), this scenario is highly unlikely to explain

the observed record. Even if we try to rationalize the high $\overline{SS}$ as an artefact of topographical focusing of the current as it enters the CGFZ, it is hard to imagine how such an exceptionally accelerated flow could be so localized in both space and time. If topographical focusing were a factor, observed current speeds would be consistently high at this location, regardless of the climate state or the origin of the water mass. Thus, in order to explain the anomalously high $\overline{SS}$ plateaus, we must consider the possibility that this portion of the record is not recording the local current speed, but may instead be a source-related signature.

The use of the $\overline{SS}$ proxy assumes a number of boundary conditions at the core site. For example, there must be a constant source of terrigenous sediment located far enough away from the site for a current sorted signal to develop. Additionally, the transporting and depositing current must maintain a relatively constant mean flow direction for the duration of the study period (Bianchi et al., 2001; Hass, 2002). Site U1304, and Gardar Drift in general, easily fulfill these basic criteria, at least during periods when the North Atlantic is dominated by northern sourced water (Chapter 3.4). However, because the $\overline{SS}$ proxy is particularly sensitive to contamination by external sediment sourced independently of variations in bottom currents (Manighetti & McCave, 1995a), another critically important framing condition in the use of $\overline{SS}$ data is that the core site remains relatively free of direct input of sediment from external depositional processes such as downslope mass movements (i.e. turbidites) and vertical flux (i.e. ice raft debris (IRD)). IODP Expedition 303/306 scientists (2006) did not report significant signs of redeposited sand or disturbed units in the U1304 cores, so mass movements are unlikely to have influenced the high $\overline{SS}$ signal in my record. IRD, on the other hand, has been observed in U1304 sediments in a number of previous studies (Hodell et al, 2009; Minth, 2009; Kuhs et al., 2014), and because it is a known contaminant of the $\overline{SS}$ signal on glacial/interglacial time scales (Hall and McCave, 2000; McCave and Hall, 2006), we must consider the possibility that the vertical flux of IRD grains from melting icebergs is the reason for the unusually high values observed in my deglacial and glacial inception aged samples.

In his seminal study on the subject of IRD deposition, Ruddiman (1977) identified a W-E latitudinal band—from 46° to 50° N—across the North Atlantic in which the observation of IRD material in marine sediments is generally concentrated. Although Site U1304 is located beyond the zone of maximum deposition (Fig. 6.2), its proximity to the northern edge of the Ruddiman Belt implies a strong possibility that at least intermittent IRD deposition at the site

is likely. Furthermore, IRD north of the Ruddiman Belt is well documented, and in some locations quite persistent due to the high availability of glacial sources (Bond & Lotti, 1995; Kuhs, 2014).

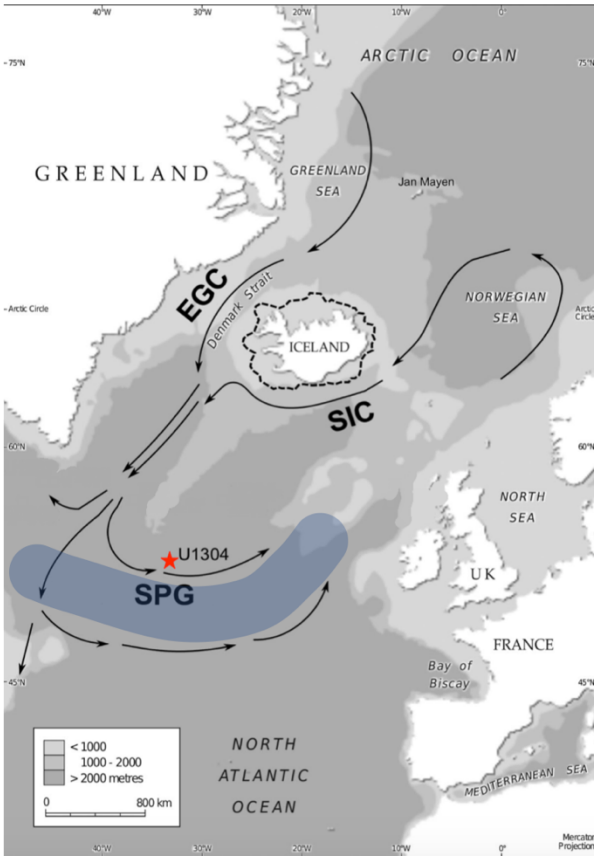

Figure 6.2. Bathymetric map showing the location of Site U1304 (red star) relative to the major iceberg trajectories (black arrows), drawn after Ruddiman (1977). The blue shading delimits the approximate extent of the Ruddiman Belt. The dashed line indicates the LGM extent of the Icelandic Ice Sheet. EGC, East Greenland Current; SIC, South Icelandic Current; SPG, Subpolar Gyre (Modified from Kuhs, 2014).

IRD percentages in sediments at Site U1304 are assessed by Minth (2009) and Kuhs (2014) for MIS 6 through the MIS 5e/5d transition. Based on visual inspection of the weight percent of the >150µm fraction, Minth (2009) concludes that, except for a large peak between 23.17 and 22.67 mcd which she attributes to Heinrich Event 11 (136-130 kyr BP) (Skinner and Shackleton, 2006), the majority of the coarse fraction in MIS 6 sediments is composed of biogenic carbonate (i.e. forminifera). IRD falls to < 5% of sample mass throughout the MIS 5e section, followed by a small peak (~6%) at 16 mcd. Minth (2009) associates this IRD peak to Cooling Event 24 (C24, 107 kyr BP) at the MIS 5e/5d transition. The primary focus of Kuhs' (2014) study was ice-rafted tephra during MIS 6. However, he did include the early MIS 5e interval in his data (Fig 6.3) which showed significant IRD peaks continuing after the start of the benthic $\delta^{18}O$ plateau, with a sharp decrease at 22.4 mcd (~127 kyr BP according to my age

model). Like Minth (2009), Kuhs' (2014) IRD counts were based on visual inspection of the >150 μm fraction, and, along with Nps% indicating the persistence of cold surface conditions beyond the deglacial interval, supporting the idea that IRD might have been a secondary source of sedimentation at U1304 during deglacial and glacial transitions during early and late MIS 5e respectively.

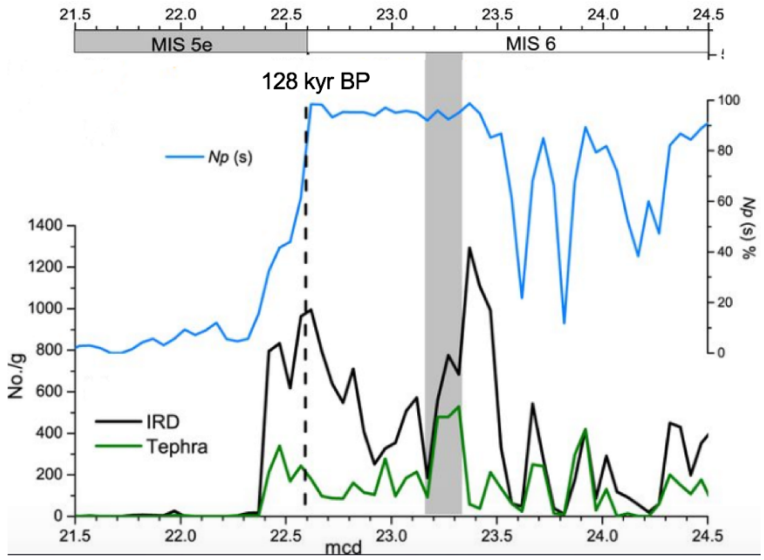

Figure 6.3. Selected proxy data for Site U1304 plotted against mcd, including NpS% (blue), IRD, grain counts per gram dry sediment (black), and tephra, grain counts per gram dry sediment (green). Stratigraphy based on Hodell et al. (2009). The shaded grey area denotes the study period for Kuhs (2014) (Modified from Kuhs, 2014).

The observed low deglacial sedimentation rate at Site U1304 may also support the hypothesis that secondary sediment sourcing is influencing the new $\overline{SS}$ record. According to my age model (Chapter 4.3), the deglacial sedimentation rate was significantly lower than the peak interglacial rate (5.1 vs. 37.5 cm/kyr respectively), as well as the mean sedimentation rate for the whole core (15 cm/kyr). The fact that deglacial and glacial conditions reduced rather than magnified the supply of sediment to the site suggests a significant reduction in lateral transport and sediment focusing by strong boundary currents, and strongly supports the hypothesis that lateral import of sediment by ISOW was reduced during this time. This possibility adds weight to the anomalous nature of my very high $\overline{SS}$ results. If lateral transport was largely eliminated due to a reduced and/or shoaled boundary current, then deglacial and glacial deposition must have been characterized as mostly pelagic. One possible way to explain the simultaneously low sedimentation rate and high $\overline{SS}$ results in the absence of a strong depositional current, is if that pelagic flux delivered a large amount of coarse silt from unsorted IRD.

Two studies which addressed the problem of IRD contamination in $\overline{SS}$ data: Manighetti and McCave (1995a) and Hass (2002), found little difference in their results when the IRD component was removed. Manigehtti and McCave (1995) first identified a core site whose sediments were inferred to represent a standard pelagic input for the region, then subtracted that signal from near-by core site data where sediment focusing had obviously been a factor. Hass (2002), on the other hand, reasoned that since sand cannot be moved by bottom currents, and that since the amount of silt in a sample is linearly correlated to the amount of sand, then the non-biogenic sand percentage of a given sample can be used as a proxy for the amount of IRD diluting the current-sorted part of the size distribution. The underlying assumption here is that the higher the IRD concentration in a sample is, the higher the $\overline{SS}$ value will be, and that by removing the equivalent of the sand percentage from the silt distribution, the true current-sorted signal will emerge. Although the methods in these two attempts at normalizing $\overline{SS}$ values by subtracting IRD from the signal are very different, the conclusions from both studies were equivocal. Little was gained from either exercise, and the effect of the normalization was to merely smooth the maxima and minima. The overall profile of each record remained the same. It is tempting to draw the conclusion from these studies that IRD contamination is ultimately not that critical in the interpretation of $\overline{SS}$ results. And indeed, McCave and Hall (2006) have suggested that flow speeds of ~10 cm/s would be able to easily sort and distribute IRD input of up to 10 cm/kyr. This is, unfortunately, a circular conundrum, because you need to know the flow speed of the current you are trying to infer before you can determine whether or not excessive IRD input has overprinted your current sorted signal.

Finally, it bears repeating that there are only four data points, with a sampling resolution of 4300 years, covering the entire late glacial and deglacial portion of my $\overline{SS}$ record. And just ten samples representing the late interglacial climate transition into MIS 5d. With this sparse sampling it is unclear how faithfully the variability within these intervals is captured by the existing record, nor how different the variability and values are from the higher resolution carbon isotope time series. Even so, the consistency and similarity in the profiles of the high $\overline{SS}$ shoulders are striking, and difficult to reconcile as solely changes in flow speed. Particularly considering the broad consistency of regional $\overline{SS}$ records indicating relatively low glacial current speeds. Since the possible IRD component remains difficult to fully account for, and cannot be ruled out as a contaminating influence on the anomalously high $\overline{SS}$ values, I cannot confidently conclude that those early and later portions of the record which are dominated by

anomalously high $\overline{SS}$ are accurately reflecting bottom current variability. Thus, for the remainder of the discussion I will focus on the peak interglacial interval where the bulk of the data lies, and which has little to no IRD influence.

6.2 Mid-plateau $\overline{SS}$ peak

The mid-interglacial portion of the record shows a steadily accelerating bottom flow starting just prior to 124 kyr BP and continuing for ~ 4 kyr through the middle of the MIS 5e benthic $\delta^{18}O$ plateau. This gradual trend towards larger $\overline{SS}$ is overprinted by centennial-scale oscillations which steadily increase in magnitude as flow speed ($\overline{SS}$) increases. The period of high bottom flow ends abruptly at ~120 kyr BP when $\overline{SS}$ falls 5.3 μm in roughly 100 years (marked excursion IV on Figure 5.3). After this rapid deceleration, current vigor does not immediately recover, but rather oscillates at a lower level for ~3 kyr before steeply accelerating into the previously discussed anomalously high glacial levels. $\delta^{13}C$, on the other hand, increases sharply at ~125 kyr from -0.2 to 1.0‰, and remains relatively high and stable for the remainder of the peak interglacial period. Once again there is an apparent decoupling of the tracers as $\overline{SS}$ accelerates while $\delta^{13}C$ remains relatively high and stable during this time period. However, in this case, the reason for the divergent trends is highly unlikely to be related to IRD contamination since global ice volume had reached a minimum during peak MIS 5e, and, as discussed above, IRD percentages in U1304 sediments remained near zero throughout the period.

The high and stable $\delta^{13}C$ values suggest that Site U1304 was fully bathed in newly ventilated, low nutrient, northern sourced water by the mid-plateau. This is consistent with previous findings indicating a strong interglacial circulation with vigorous deep water convection and strong boundary currents during the mid MIS 5e (Hall & McCave, 2000; Evans et al., 2006). Previous studies have observed a long-term increasing trend in preformed NADW $\delta^{13}C$ during the LIG (Fronval et al., 1998; Galaasen et al., 2014), and one would expect ISOW $\delta^{13}C$ values over Site U1304 to track closely with the end-member values of its source waters. In other words, in a circulation mode where ISOW was the dominant bottom water influence, $\delta^{13}C$ would be driven by the 'preformed' chemical composition of ISOW, while $\overline{SS}$ would indicate the vigor of ISOW flow over the core site. The generally high $\delta^{13}C$ values observed here are consistent with strong ISOW influence effectively 'saturating' this tracer. However, my $\overline{SS}$

record reveals significant variability in flow vigor occurred even during this interval of dominant ISOW influence. Thus, the observed decoupling in the $\overline{SS}$ and $\delta^{13}C$ records for this section can most likely be explained by $\delta^{13}C$-saturation in the source water, concurrent with increasing vigor of ISOW.

6.2.1 Comparisons with previously published records

In Chapter 2.4 it was suggested that an apparent peak in current speed centered around 120 kyr BP, immediately followed by a significant and abrupt deceleration, is a robust feature of the sedimentological data from multiple cores throughout the northeast North Atlantic. The new record for Site U1304 is consistent with the pattern observed in these previously published records. Given the apparent structural similarity between mine and multiple other $\overline{SS}$ records, it is reasonable to conclude that the central part of the U1304 record (~124-120 kyr BP) is likely to be unambiguously reflecting bottom current variability over the core site. In general, the record implies that interglacial ISOW flow vigor rose gradually and peaked just prior to 120 kyr BP, after which it abruptly decreased. The subsequent minimum in flow at ~119 kyr BP is also associated with a minor decrease in benthic $\delta^{13}C$, suggesting that the ISOW flow was reduced to the point that lower nutrient, southern sourced water might have started to exert more influence at the core site at this time.

Hall et al. (1998) studied two cores at opposite ends of the path of NADW evolution. NEAP-18K (52°46 N, 30°20 W; 3275 m water depth) is located on the southern end of Gardar Drift, relatively close to the ISOW source region, while MD95-2036 (33°41 N, 57°34 W; 4462 m water depth) lies on the eastern Bermuda rise. Both cores are presently bathed by the lower component(s) of NADW. In spite of the geographical distance between the two cores, Hall et al. (1998) find unmistakable synchronicity in the major $\overline{SS}$ decelerations of the two records (events A, B, and C in Fig. 6.4). The timing of deceleration B in the Hall et al. (1998) study (118-120 kyr BP) matches well with both the timing and the magnitude of excursion IV (Fig 5.3) in the U1304 $\overline{SS}$ record. It is notable that, similar to my record, the deep chemical tracers in the Hall et al. (1998) study do not track with these strong fluctuations in near-bottom flow speeds. There is a brief dip in nutrients (Cd/Ca) and a more significant reduction in carbonate percentage on the more southern site coincident with deceleration B, but benthic $\delta^{13}C$ shows

only a slight decrease in value at this time, supporting the idea that bottom chemistry over Gardar Drift was largely unaffected by the flow deceleration at ~120 kyr BP.

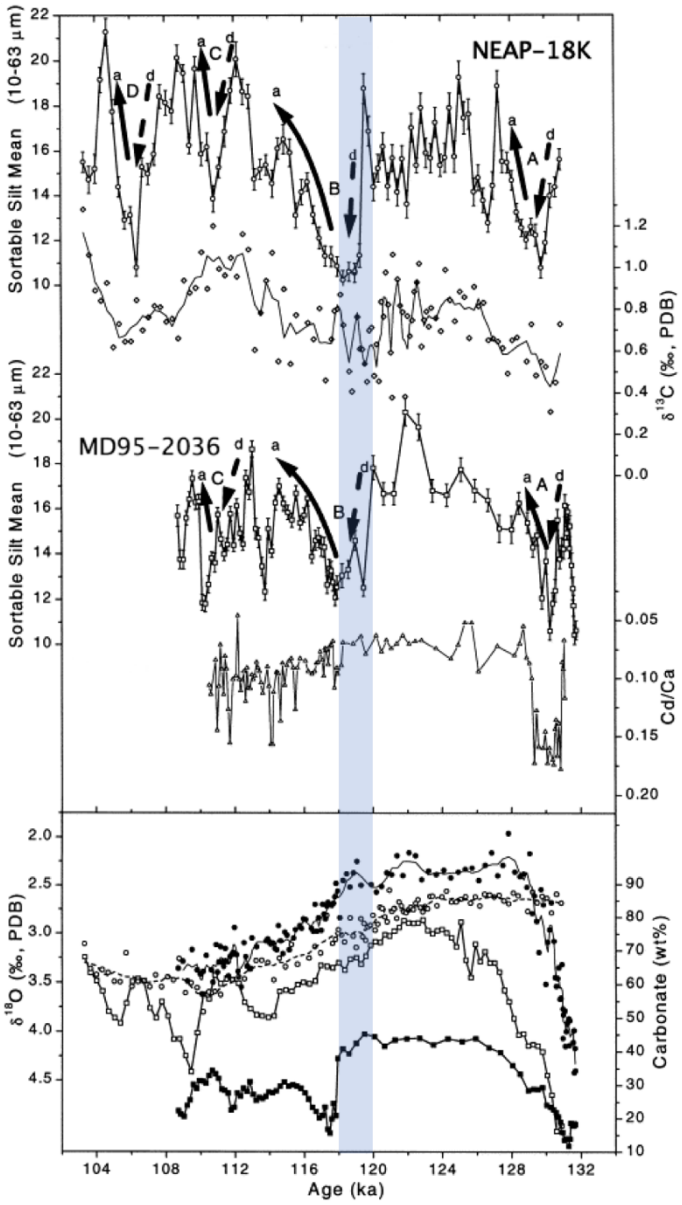

Figure 6.4. Proxy data for NEAP-18K and MD95-2036 plotted against age. Upper panel: $\overline{SS}$ and bethic $\delta^{13}C$ (*C. wuellerstorfi*) for NEAP-18K; $\overline{SS}$ and benthic Cd/Ca ratios for MD95-2036. Lower panel: benthic δ18O and < 63 µm carbonate percentage for NEAP-18K (open circles and squares) and for MD95-2036 (closed circles and squares). Shaded blue region highlights the mid-MIS 5e cooling event (Modified from Hall et al. 1998).

Deaney et al.'s (2017) $\overline{SS}$ record for ODP Site 983 on the northern end of Gardar Drift (60°48 N, 23°68 W; 1984 m water depth) also shows a distinctive peak just prior to ~120 kyr BP followed by a rapid deceleration (Fig. 6.6). The long-term trends in the Deaney et al. (2017) $\overline{SS}$ record track well with orbital trends as recorded by benthic $\delta^{18}O$ (i.e. smaller grain size and

slower currents during the glacial period, larger grain sized and faster currents during the interglacial). However, like Site U1304, a significant amount of both centennial- and millennial-scale variability is evident even during the peak flow interval of the interglacial. The abrupt decrease in current speed, which starts ~121 kyr BP in the Site 983 record, is marginally less steep than those recorded in the NEAP-18K and U1304 cores. This makes sense as the location of Site 983, on the northern end of Gardar Drift, places it much more directly and consistently in the path of the Iceland-Scotland overflows. Whereas NEAP-18K and U1304 are far down on the drift where decreases from strong overflow intensity and flow axis depth are expected to be felt first (Langehaug et al. 2016).

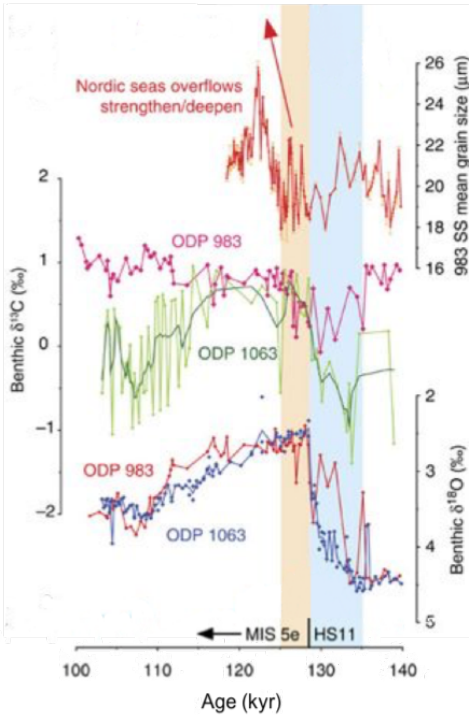

Figure 6.6 Proxy data for ODP Sites 983 and 1063 (33° N, 57° W—on the Bermuda Rise; 4584 m water depth). $\overline{SS}$ for Site 983; benthic foraminiferal $\delta^{13}C$ and $\delta^{18}O$ for both sites (Modified from Deaney et al. 2017).

By comparing these published proxy records with the new $\overline{SS}$ record for Site U1304, a clear picture of coherent flow speed variability during the peak LIG begins to emerge for sites located along the Gardar Drift. The clearest observable trends in these records are a general increase in flow speed starting at ~124 kyr BP, a peak in flow just prior to ~120 kyr BP, and a rapid deceleration directly following this peak. Given the apparent similarity in timing and magnitude

of these trends, it appears that flow speeds became progressively stronger along the entire axis of the high velocity ISOW core through the course of the peak interglacial. The increasing trend is observed to be strongest at the shallower, more northern site (983) because it is more directly monitoring overflow intensity. However, the current eventually becomes strong and dense enough to influence the deeper, more southerly sites as well. At ~120 kyr BP the signal over all three sites decreases when the current abruptly shoals, most likely due to a precipitous decrease in overflow density and/or vigor. In a recent modelling study, Langehaug et al. (2016) confirmed the link between Gardar Drift bottom flow and ISOW. This study found that 76% of the variance in the simulated bottom current velocity could be explained by changes in the volume transport and density of the Faroe-Shetland Channel overflows, with the density contrast between the overflow and the ambient water playing the largest role in determining the downstream velocity. In addition, the Langehaug et al. (2016) study found a high correlation between flow velocity and the thickness of the simulated current, strongly suggesting that when overflow density is high, the volume transport over the sill is also high. Conversely, when overflow density is low, less dense overflow water crosses the sill. This finding supports the suggestion by Bianchi et al. (2001) that the shoaling of the boundary current observed as far downstream as the Blake Outer Ridge was related to reduced convective activity in the Nordic Seas. Thus, a sudden, drastic reduction in convection intensity and/or buoyancy loss is also a possible explanation for the abrupt and coherent shoaling observed in mine and other the Gardar Drift records.

What drives changes in buoyancy and convection intensity? In a recent study, Lohmann et al. (2015) simulated ISOW variability during the last millennium, and found a positive correlation between strong overflows and high Nordic Seas surface temperatures and salinity. In other words, Lohmann et al.'s (2015) results suggested that positive salinity anomalies are associated with strongly increased Nordic Seas convection. Conversely, convection intensity decreases when surface temperatures drop and/or surface waters freshen. In this way, my results showing a steady increase and strong decrease in overflow could potentially be related to increased and decreased convection intensity respectively. Such continued modulation of the convection density and flux of the Nordic Seas overflows during the mid-interglacial, presents a significant challenge to our understanding of interglacial circulation based on chemical tracers being generally vigorous and stable. A priori, it is unclear what could have caused the kind of pronounced freshening necessary to cause such a strong disruption to deep water convection in the middle of an interglacial climate. In general, stable benthic $\delta^{18}O$ records from this period

demonstrate that global ice volume, which was at a minimum, did not experience any significant change prior to the ~120 kyr BP event (Cortijo et al., 1994). And, since insolation was waning at this time (Rasmussen et al., 2003; Cortijo et al., 1999), the kind of catastrophic ice sheet melt and iceberg delivery that suppressed vigorous deep water formation during the early LIG is unlikely. In the absence of large cyrospheric related freshwater inputs, two possible sources of excess freshwater in the Nordic Seas are: an increase in the delivery of relatively fresh North Pacific surface water via the Bering Strait potentially due to increased sea level and/or anomalous Ekman transports, or regional changes in the balance of precipitation and evaporation (Cortijo et al., 1994). Regardless of the exact drivers, it appears that a major source of deep water to the global overturning ("conveyor") circulation varied significantly during the peak of the last interglacial period when conditions were warmer and sea level was slightly higher (Otto-Bleisner et al. 2006). This raises the possibility for future changes in variability since, in the broadest sense, it suggests that past deep circulation continued to be sensitive to buoyancy forcing in the deep water formation region even during times of generally strong overturning. Models project significant warming and freshening in the high latitude North Atlantic by 2100 due to changes in evaporation and precipitation (IPCC, 2013). Studies based on models and proxy data have both suggested that a strong decrease in overturning is plausible due to future freshening and warming (Galaasen et al., 2014).

The new U1304 $\overline{SS}$ record produced for this thesis is currently one of the highest resolution records of bottom current variability spanning the peak LIG. Figure 6.7 shows a close-up view of the period of flow acceleration spanning 118-125 kyr BP. It emphasizes the high degree of both short (centennial) and long (multi-millennial) term variability that occurs even when overturning circulation is thought to have been stable and vigorous. Figure 6.7 also highlights the fact that as bottom flow speed increased so did the magnitude of centennial-scale variability. Each short-term oscillation lasts approximately 200 years, and the magnitude of each oscillation increases by a factor of about three over the course of ~4000 years. The high and stable $\delta^{13}C$ values during the period of peak flow (Fig. 6.1) confirm that ISOW is strong and remains the dominate water mass over Gardar Drift through the interval. This geochemical stability strongly suggests that the observed short-term fluctuations in current strength are transient, and do not affect the steady-state circulation regime long enough for deep water carbon chemistry to change significantly. It is interesting to note that these centennial scale flow speed transients share a similar structure and pacing to the multi-decadal to centennial scale variability observed

by Mjell et al. (2016) in late Holocene $\overline{SS}$ records for the Gardar Drift, which were found to share a strong correlation with high frequency AMO climate variability (Chapter 2.3). It is also intriguing that the maximum magnitude of these oscillations occurs during the period of high flow speed. While there could be multiple explanations for such behavior, perhaps the simplest and most consistent with the interpretation provided above, is that the largest variability in local flow speed is only possible when the main axis of strong ISOW is proximal to the site (i.e. during times of high/dense overflow). Ultimately, additional sites further up the drift and at different depths are necessary to test this hypothesis. In addition, higher sedimentation rate sites and more densely sampled timeseries are necessary to fully characterize the exact frequency and magnitude of short-term variability at Site U1304 since Mjell et al. (2016) found that even with sedimentation rates of 77 cm/kyr, it was necessary to sample every 0.5 cm in order to robustly capture and reproduce decadal-scale $\overline{SS}$ variability. Nevertheless, my new $\overline{SS}$ record provides some of the first evidence that this style of high-frequency circulation variability, with the potential to affect the climate system on decadal to multi-decadal time scales, persisted during the last interglacial.

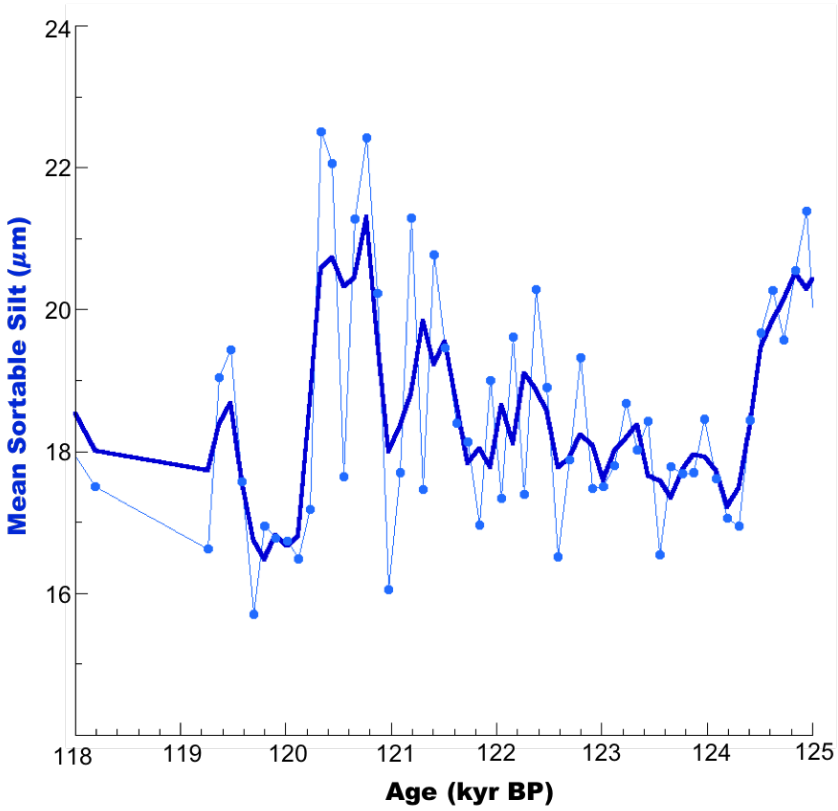

Figure 6.7. Mean sortable silt results for Site U1304 for the period of flow acceleration (~120 to 124 kyr BP) during the peak MIS 5e interval. The light blue line is the arithmetic average of all sample measurements, while the dark blue line is a 3-point running average of the mean.

6.3 MIS 5e climate evolution

As we have seen, the combined deep ocean flow speed and nutrient proxies from IODP Site U1304 document a strong, well-established NADW influence throughout the MIS 5e benthic plateau (as recorded by stable, relatively high δ13C) coincident with highly variable ISOW strength over the site. Furthermore, this pattern is consistent with other records from the Gardar Drift (Hall et al., 1998; Deaney et al., 2017), as well as other overflows (i.e. DSOW (Galaasen et al., 2014), and NADW (Bianchi et al., 2001). Such relatively large and persistent changes in overturning vigor (as implied by the observed long-term trends in overflow variability), suggest a causal link to variability in the amount of warm, saline waters exchanged between the North Atlantic and Nordic Seas. Such variability in heat transport could, in turn, potentially influence regional climate (Rahmstorf, 2006).

Generally high benthic $\delta^{13}C$ values (Galaasen et al., 2014) as well as favorable benthic foraminiferal assemblages at sites located to the north and south of the Iceland-Scotland Ridge (Rasmussen et al, 2003) indicate that convection in the Nordic Seas started as soon as the main phase of deglaciation (Termination II) ended. High latitude, northern hemisphere summer insolation was approaching a maximum (~127-128 kyr BP (Cortijo et al., 1999)), and geochemical tracers indicate that sea surface temperatures in the northeast North Atlantic were also high at this time (Bauch & Kandiano, 2007). In spite of these favorable conditions, we have seen that ISOW along the Gardar Drift remained relatively weak during the early LIG—at least as compared to the mid interglacial. A possible reason for the delay in the establishment of vigorous interglacial style convection in the Nordic Seas has been shown by analyzing downcore changes in planktonic foraminifera assemblages (Rasmussen et al, 2003; Van Nieuwenhove et al., 2011). These studies show cooler, fresher surface conditions persisting north of the ridge well into the peak interglacial period due to prolonged input of melt water from the Saalian ice sheet. The extended period of freshwater forcing held the polar front in its more southerly position following the crest of the Iceland-Scotland Ridge, and restricted the path of the inflowing NAC to a narrow corridor east of the Faroe Islands, and along the Norwegian coast. The reduced advection of warm, salty Atlantic waters combined with excess fresh water from melting ice increased buoyancy and suppressed the vigorous overturning of surface waters during the early LIG (Rasmussen et al., 2003).

The portion of the new $\overline{SS}$ record for Site U1304 that correlates to the early LIG is too ambiguous to either confirm or contradict the picture of constant but weakly variable overflow activity observed in the previously mentioned Gardar Drift records. On the one hand, the chemical and dynamical tracers at U1304 occasionally covary at this time in such a way that it appears deep circulation is responding coherently to transient fluctuations in overflow strength (especially for the excursions marked I and II on Figure 5.3). But on the other hand, the uncertainty regarding secondary sediment sourcing, especially at the beginning of the period, cannot be reconciled, and the reliability of this portion of the record remains unclear.

Starting at ~127 kyr BP, sea surface temperatures in the Nordic Seas began to rise (Rasmussen et al., 2003). Shifting planktonic foraminifera assemblages suggest that a more modern style of interglacial surface circulation was established; the polar front retreated, and strong inflows of warm, salty Atlantic water entered the southeastern Norwegian Sea in the manner we see today (Bauch & Kandiano, 2007). This period corresponds roughly to the middle Eemian in northwest Europe, where terrestrial records indicate that the warming of the Nordic Seas initiated a more temperate, marine climate with relatively cooler summers and wet, mild winters (Rasmussen et al., 2003). In marine records, this period corresponds to the mid-MIS 5e benthic plateau, when sedimentological records throughout the North Atlantic, including the new U1304 $\overline{SS}$ record, show steadily accelerating flow speeds which signify vigorous overturning and progressively strengthening and/or deepening bottom currents. The timing of this LIG thermal maximum in the Nordic Seas appears to contrast with that of the Holocene. For the LIG, optimal oceanic conditions were delayed by about 3000 years (Rasmussen et al., 2003) relative to the northern hemisphere summer insolation maximum, whereas the Holocene thermal optimum and concomitant peak flow speeds (~7 kyr BP (Thornally et al., 2013)) occurred more or less in step with peak summer insolation. The reason for this delay in the establishment of fully hypsithermal interglacial circulation during the LIG is, as already mentioned, the prolonged melting history of the Saalian ice sheet, which was much larger than the Weichselian ice sheet, and therefore had a more profound impact on deglacial water mass evolution (Van Nieuwenhove et al., 2011).

The new $\overline{SS}$ record for U1304 is broadly consistent with this picture of generally strengthening and intensifying overturning circulation during the mid-MIS 5e. The observation that the magnitude of centennial-scale variability at U1304 also gradually increases during this interval

may also further validate this idea. Shallower, up-drift sites like Site 983 are more consistently in the path of the bottom current, and therefore are well situated to directly monitor overflow intensity. However, deep cores like U1304, which are located at the end of their drifts, are only in the direct path of the bottom current when overflows are very intense, and are dense enough to sink deep into the water column. Such deep, distant cores are therefore good locations to observe transient variability when currents are strong, because minor changes to overturning density will cause the downstream current to detach from the sea bed at the most distant sites first (Langehaug et al, 2016). Thus, Site U1304 was able to capture both the long-term increase in overturning intensity which built gradually as surface conditions in the Nordic Seas became increasingly favorable to deep convection, as well as the shorter-term variability due to more transient fluctuations in overflow density.

The LIG thermal optimum appears to have ended with the sudden decrease of ISOW density and the subsequent dramatic reduction in flow velocity at ~120 kyr BP. It is the single most coherent event in the combined Gardar Drift sediment records (i.e. Site U1304 (current study); NEAP-18K (Hall et al., 1998); and Site 983 (Deaney et al., 2017)), and similar reductions have been observed in proxy records throughout the North Atlantic region at this time (e.g. Cortijo et al., 1994; Hall & McCave 2000; Bianchi et al., 2001; Oppo et al., 2006; Henderson, 2009). The estimated timing of this event, depending on the resolution of the record and the accuracy of its underlying age model, varies by up to 3 to 4 kyr between locations. Thus, it cannot be ruled out that the approximately similar timing of the flow reduction observed in the Gardar Drift records at ~120 kyr BP may be pure coincidence. Limitations in the accuracy and comparability of existing age models, particularly within the MIS 5e benthic $\delta^{18}O$ plateau, make precise correlations between events difficult. Nevertheless, there appears to be strong empirical evidence showing a large, regionally significant deceleration event that matches the shape and magnitude of the abrupt reduction in current speed that occurred at ~120 kyr BP over Site U1304. In all cases, the deceleration event occurs well within the phase of low ice volume (i.e. during the benthic $\delta^{18}O$ plateau), providing further evidence of significant overflow variability even during periods of apparent interglacial stability.

As mentioned above, both benthic $\delta^{13}C$ and $\delta^{18}O$ along the Gardar Drift remained essentially stable during and after the event, with only a minor increase in $\delta^{13}C$ at the southern sites. Observations from deep water sites in the Southern Ocean (Govin et al., 2009) demonstrate a marked change in deep chemistry (i.e. reduced $\delta^{13}C$) starting at ~120 kyr BP reflecting

enhanced convection over the Antarctic shelf, and subsequent northward expansion of Antarctic Bottom Water (AABW). Thus, possibly explaining the apparent slight increase in the influence of southern sourced LDW at Gardar Drift just prior to the MIS 5e/5d transition. Surface proxies from the northeast North Atlantic, on the other hand, indicate that the mid-MIS 5e deceleration was accompanied by significant surface cooling. For example, Hall et al. (1998) note a decrease in the abundance of the warm water species, *N. pachyderma* (d.) from 35% to <5%, and a 0.65‰ increase in planktonic $\delta^{18}O$ values. These data suggest that the decrease in flow speed over the NEAP-18K site was coincident with a regional sea-surface cooling by as much as 2 to 3°C. Other studies (Rasmussen et al., 2003; Bauch & Kandiano, 2007; Irvalı et al., 2012) have reported similar reductions in temperate foraminiferal assemblages and increases in planktonic $\delta^{18}O$ at this time. The concomitant occurrence of changes in circulation vigor and surface hydrography at such geographically disparate sites strongly implicates variability (decreases) in deep water formation as the mechanism for the regional cooling event centered around 120 kyr BP.

The data that has been presented here documents significant reductions in flow speed with the previously observed freshening and cooling of surface waters. Thus, bottom current behavior, as recorded by the dynamical $\overline{SS}$ proxy, appears to be consistent with the idea that climate cools when deep ocean circulation slows. Models have repeatedly shown that climate is cold when circulation is low, because a reduction in deep water production would have an attendant decrease in northward heat transport, eventually leading to cooling in the North Atlantic (Barker at al., 2011; Bakker et al., 2015). Put in the broadest possible way, it appears from these results that circulation drives climate change. The inherent contradiction in this statement is that cooling causes denser surface waters which should, in turn, cause an increase in overturning circulation. Yet models show that cooling is associated with freshening, and that salinity fluctuations are driving circulation intensity (Langehaug et al., 2016). Given that a similar climate-circulation relationship is observed in paleo records, the climate driver behind decreased circulation must ultimately be freshening driven by hydrological and/or cryospheric changes associated with cooler climates. It has been suggested that reduced insolation levels during the mid-MIS 5e would have caused cooler northern hemisphere summer temperatures (Rasmussen et al. 2003). Cooler summer temperatures combined with a proposed net positive mode for NAO atmospheric circulation at this time (Bauch & Kandiano, 2007) would bring more moisture into the Nordic Seas, and promote the growth and spread of sea ice. Thus, the

trigger for the abrupt reduction in bottom current activity observed at ~120 kyr BP, may have been anomalous freshening of the Nordic Seas surface waters due to the melting of sea ice. The documentation of a significant mid-MIS 5e flow speed deceleration in the new U1304 $\overline{SS}$ record adds weight to its significance as a major regional event which may have marked, if not the end of the last interglacial period, then at least the beginning of the end.

7. CONCLUSION

The LIG is often invoked as an analogue for the future climate state. This comparison is imperfect as high-latitude warmth during the LIG was naturally driven by an orbitally induced, seasonal and regional insolation anomaly rather than anthropogenically driven CO_2 increase. Nonetheless, the emerging picture of enhanced circulation variability during the peak LIG is instructive of a possible future scenario for deep water formation in a warming climate. For example, my results showing a major reduction in deep circulation vigor in the middle of the LIG implies that the density and/or strength of the deep component of AMOC continues to be sensitive to atmospheric and/or freshwater forcing in warm climates. One possible source of anomalous freshwater input during the LIG was episodic melting of the Greenland Ice Sheet which was recorded as multiple, extensive melt layers observed in the Eemian section of the NEEM ice core (NEEM community members, 2013). Since enhanced freshwater flux into the Nordic, Labrador, and Irminger Seas as a result of Greenland Ice Sheet melt is also expected to weaken AMOC in the near future (Böning et al., 2016), constraining the impact of these freshwater disturbances on circulation in the past may help us improve our predictions for the future.

The primary objective of this thesis has been to determine the nature and magnitude of ISOW variability during the last interglacial period. My new $\overline{SS}$ based reconstruction of temporal variability in the relative speed of the deep boundary current over the southern Gardar Drift broadly conforms with the pattern of persistent high-frequency, high-magnitude variability observed in other high-resolution records from the region. Low sampling resolution and the strong possibility of sourcing contamination preclude confident analysis of the part of the new record covering the transitional intervals into and out of the MIS 5e benthic $\delta^{18}O$ plateau. However, the peak interglacial interval demonstrates coherent centennial and multi-millennial scale variability in overflow intensity throughout the period of peak flow. Covariability in the physical and chemical proxies during the LIG seems to be strongest for short-term oscillations, while over the long-term, $\delta^{13}C$ remains relatively high and stable. This juxtaposition of high, stable $\delta^{13}C$ with significantly variable $\overline{SS}$ observed during the period of peak LIG flow, further highlights the value of $\overline{SS}$ data in reconstructing the true nature of deep ocean circulation in warm climate regimes. In cores like U1304, where the chemical proxy is near saturation during periods of strong flow, only the kinetic tracer yields meaningful new information about the strength of bottom flow, and ultimately, of potential overturning variability. And thus,

strengthens our growing understanding of the LIG as a period marked by relatively high overturning instability and change relative to the Holocene (Tzedakis et al., 2018).

Given the obvious complications surrounding my results from the transitional climate intervals, there may be limited value in pursuing further resolution from this part of the record, at least at this site. Instead, a more profitable avenue of future research may be to improve the temporal resolution of sampling through the mid-interglacial in order to more accurately resolve and characterize decadal to multi-decadal variability during peak warmth. However, since the maximum LIG sedimentation rate at Site U1304 is 40 cm/kyr and the core has already been processed and cut at 2 cm intervals, the highest achievable temporal resolution would be 50 years per sample. Mjell et al. (2016) required half-centimeter sampling from a site with a maximum sedimentation rate of 77 cm/kyr to achieve sub-decadal resolution (~7 years per sample). Therefore, it might not be possible to fully characterize high-frequency, AMO-period variability in the LIG at this site. New, higher sedimentation rate sites should be located and studied in order to determine how multi-decadal variability in the overflow varied in response to warmer than present conditions, and to more fully characterize deep circulation evolution (in both strength and geometry) through the LIG.

REFERENCES

Aagaard, K. & Carmack, E.C. (1989) The role of sea ice and other fresh water in the Arctic circulation. *Journal of Geophysical Research: Oceans, 94*(C10), 14485-14498.

Aagaard, K., Swift, J.H., & Carmack, E.C. (1985). Thermohaline circulation in the Arctic Mediterranean Seas. Journal of Geophysical Research: Oceans, 90(C3), 4833-4846.

Adkins, J.F., Boyle, E.A., Keigwin, L., & Cortijo, E. (1997). Variability of the North Atlantic thermohaline circulation during the last interglacial period. Nature, 390(6656), 154-156.

Andrews, J.T. (2000). Icebergs and iceberg rafted detritus (IRD) in the North Atlantic: facts and assumptions. Oceanograph, 13(3), 100-108.

Barker, S., Knorr, G., Edwards, R.L., Parrenin, F., Putnam, A.E., Skinner, L.C., Wolff, E., & Ziegler, M. (2011). 800,000 years of abrupt climate variability. Science, 334(6054), 347-351.

Bakker, P., Govin, A., Thornalley, D., Roche, D., & Renssen, H. (2015). The evolution of deep-ocean flow speeds and δ13C under large changes in the Atlantic overturning circulation: Toward a more direct model-data comparison. Paleoceanography, 30(2), 95-117.

Bauch, H., & Kandiano, E. (2007). Evidence for early warming and cooling in North Atlantic surface waters during the last interglacial. Paleoceanography, 22(1) N/a.

Bianchi, G.G., Hall, I.R., McCave, I.N., & Joseph, L. (1999). Measurement of the sortable silt current speed proxy using the Sedigraph 5100 and Coulter Multisizer IIe: Precision and accuracy. Sedimentology, 46(6), 1001-1014.

Bianchi, G.G., & McCave, I.N. (1999). Holocene periodicity in North Atlantic climate and deep-ocean flow south of Iceland. Nature, 397(6719), 515-517.

Bianchi, G.G., & McCave, I.N. (2000). Hydrography and sedimentation under the deep western boundary current on Björn and Gardar Drifts, Iceland Basin. Marine Geology, 165(1), 137-169.

Bianchi, G.G., Vautravers, M., & Shackleton, N.J. (2001). Deep flow variability under apparently stable North Atlantic deep water production during the Last Interglacial of the subtropical NW Atlantic. Paleoceanography, 16(3), 306-316.

Boessenkool, K., Hall, I., Elderfield, H., & Yashayaev, I. (2007). North Atlantic climate and deep-ocean flow speed changes during the last 230 years. Geophysical Research Letters, 34(13), N/a.

Bond, G.; Heinrich, H.; Broecker, W.; Labeyrie, L.; Mcmanus, J.; Andrews, J.; Huon, S.; Jantschik, R.; Clasen, S.; Simet, C. (1992). Evidence for massive discharges of icebergs into the North Atlantic ocean during the last glacial period. Nature, 360(6401): 245–249.

Bond, G., & Lotti, R. (1995). Iceberg discharges into the North Atlantic on millennial time scales during the last glaciation. Science, 267(5200), 1005-1010.

Broecker, W.S. (1991). The great ocean conveyor. Oceanography, 4(2), 79-89.

Böning, C., Behrens, E., Biastoch, A., Getzlaff, K., & Bamber, J. (2016). Emerging impact of Greenland meltwater on deepwater formation in the North Atlantic Ocean. Nature Geoscience, 9(7), 523-527.

Clark, P.U., Pisias, N.G., Stocker, T.F., & Weaver, A.J. (2002). The role of the thermohaline circulation in abrupt climate change. Nature, 415(6874), 863-869.

Cortijo, E., Duplessy, J.C., Labeyrie, L., Leclaire, H., Duprat, J., & Van Wearing, T.C.E. (1994). Eemian cooling in the Norwegian Sea and North Atlantic ocean preceding continental ice-sheet growth. Nature, 372(6505), 446-449; 446-446.

Cortijo, E., Lehman, S., Keigwin, L., Chapman, M., Paillard, D., & Labeyrie, L. (1999) Changes in Meridional Temperature and Salinity Gradients in the North Atlantic Ocean (30°–72°N) during the Last Interglacial Period. Paleoceanography, 14(1), 23-33.

Curry, W.B., Duplessy, J.C., Labeyrie, L.D., and Shackleton, N.J. (1988). Changes in the distribution of δ13 C of deep water ΣCO2 between the Last Glaciation and the Holocene. *Paleoceanography, 3*(3), 317-341.

Curry, W., & Oppo, D. (2005). Glacial water mass geometry and the distribution of δ13C of ΣCO2 in the western Atlantic Ocean. *Paleoceanography, 20*(1), PA1017.

Dahl-Jensen, D., Albert, M., Roeckmann, T., Zheng, J., & NEEM community members. (2013). Eemian interglacial reconstructed from a Greenland folded ice core. 489-0836.

Dansgaard, W., Johnsen, S.J., Clausen, H.B., Dahl-Jensen, D., Gundestrup, N.S., Hammer, C.U., Hvidberg, C.S., Steffensen, J.P., Sveinbjørnsdottir, J.P., Jouzel, J., & Bond, G. (1993). Evidence for general instability of past climate from a 250-kyr ice-core record. Nature, 364(6434), 218-220.

Deaney, E.L., Barker, S., & van de Flierdt, T. (2017). Timing and nature of AMOC recovery across Termination 2 and magnitude of deglacial CO2 change. Nature Communications, 8, 14595.

Delworth, T., & Mann, M. (2000). Observed and simulated multidecadal variability in the Northern Hemisphere. Climate Dynamics, 16(9), 661-676.

Delworth, T. L., Clark, P. U., Holland, M., Johns, W. E., Kuhlbrodt, T., Lynch-Stieglitz, J., Morrill, C., Seager R., Weaver, A. J., and Zhang, R. (2008). "The potential for abrupt change in the Atlantic Meridional Overturning Circulation." In: *Abrupt Climate Change*. A report by the U. S. Climate Change Science Program and the Subcommittee on Global Change Research, U. S., Geological Survey, Reston, VA: 258-259.

Dickson, R.R., & Brown, J. (1994). The production of North Atlantic Deep Water: Sources, rates, and pathways. Journal of Geophysical Research: Oceans, 99(C6), 12319-12341.

Duplessy, J., Shackleton, N., Matthews, R., Prell, W., Ruddiman, W., Caralp, M., & Hendy, C. (1984). 13C Record of Benthic Foraminifera in the Last Interglacial Ocean: Implications for the Carbon Cycle and the Global Deep Water Circulation. *Quaternary Research, 21*(2), 225-243.

Duplessy, J.C., Shackleton, N.J., Fairbanks, R.G., Labeyrie, L., Oppo, D., and Kallel, N. (1988). Deepwater source variations during the last climatic cycle and their impact on the global deepwater circulation. *Paleoceanography, 3*(3), 343-360.

Elliot, Labeyrie, & Duplessy. (2002). Changes in North Atlantic deep-water formation associated with the Dansgaard–Oeschger temperature oscillations (60–10 ka). Quaternary Science Reviews, 21(10), 1153-1165.

Ellison, C., Chapman, M., & Hall, I. (2006). Surface and deep ocean interactions during the cold climate event 8200 years ago. Science (New York, N.Y.), 312(5782), 1929-32.

Evans, H., Hall, I., Bianchi, G., & Oppo, D. (2007). Intermediate water links to Deep Western Boundary Current variability in the subtropical NW Atlantic during marine isotope stages 5 and 4. Paleoceanography, 22(3), N/a.

EPICA Community Members, Barbante, C., Barnola, J.-M., Becagli, S., Beer, J., Bigler, M., . . . Wolff, E. (2006). One-to-one coupling of glacial climate variability in Greenland and Antarctica. Nature, 444(7116), 195.

Expedition 303 Scientists. (2006). Site 1304. In: Channell, J.E.T., Kanamatsu, T., Sato, T., Stein, R., Alvarez Sarikian, C.A., Malone, M.J., & the Expedition 303/306 Scientists. *Proc. IODP. 303/306*. College Station TX (Integrated Ocean Drilling Program Management International Inc.).

Faugères, J., Mézerais, M., & Stow, D. (1993). Contourite drift types and their distribution in the North and South Atlantic Ocean basins. Sedimentary Geology, 82(1-4), 189-203.

Fronval, T., Jansen, E., Haflidason, H., & Sejrup H.P. (1998). Variability in surface and deep water conditions in the nordic seas during the last interglacial period. Quaternary Science Reviews, 17(9), 963-985.

Galaasen, E., Ninnemann, U., Irvalı, N., Kleiven, H., Rosenthal, Y., Kissel, C., & Hodell, D. (2014). Rapid reductions in North Atlantic Deep Water during the peak of the last interglacial period. Science (New York, N.Y.), 343(6175), 1129-32.

Govin, A., Michel, E., Labeyrie, L., Waelbroeck, C., Dewilde, F., & Jansen, E. (2009). Evidence for northward expansion of Antarctic Bottom Water mass in the Southern Ocean during the last glacial inception. Paleoceanography, 24(1), N/a.

Greenland Ice-Core Project (GRIP) Members. (1993). Climate instability during the last interglacial period recorded in the GRIP ice core. Nature, 364(6434), 203-207.

Grootes, P.M., Stuiver, M., White, J.W.C., Johnsen, S., & Jouzel, J. (1993). Comparison of oxygen isotope records from the GISP2 and GRIP Greenland ice cores. Nature, 366(6455), 552-554.

Hall, I., & McCave. I.N. (2000). Palaeocurrent reconstruction, sediment and thorium focussing on the Iberian margin over the last 140 ka. Earth and Planetary Science Letters, 178(1), 151-164.

Hall, I., McCave, I.N., Chapman, M., & Shackleton, N. (1998). Coherent deep flow variation in the Iceland and American basins during the last interglacial. Earth and Planetary Science Letters, 164(1), 15-21.

Hansen, B., & Østerhus, S. (2000). North Atlantic–Nordic Seas exchanges. Progress in Oceanography, 45(2), 109-208.

Hass, H. (2002). A method to reduce the influence of ice-rafted debris on a grain size record from northern Fram Strait, Arctic Ocean. Polar Research, 21(2), 299-306.

Hátún, H., Sandø, A., Drange, H., Hansen, B., & Valdimarsson, H. (2005). Influence of the Atlantic subpolar gyre on the thermohaline circulation. Science (New York, N.Y.), 309(5742), 1841-4.

Heinrich, H. (1988). Origin and consequences of cyclic ice rafting in the northeast Atlantic Ocean during the past 130,000 years. Quaternary Res, 29, 143-152.

Henderson, S. (2009). *Tracking deep water flow on Eirik Drift over the past 160 kyr: Linking deep water changes to freshwater fluxes*. (Unpublished doctoral dissertation). Rutgers University. New Brunswick, NJ.

Hodell, D.A., Minth, E.K., Curtis, J.H., McCave, I.N., Hall, I.R., Channell, J.E.T., & Xuan, C. (2009). Surface and deep-water hydrography on Gardar Drift (Iceland Basin) during the last interglacial period. Earth and Planetary Science Letters, 288(1), 10-19.

Hurrell, J. (1995). Decadal trends in the North Atlantic Oscillation: Regional temperatures and precipitation. Science, 269(5224), 676.

Irvalı, N., Ninnemann, U., Galaasen, E., Rosenthal, Y., Kroon, D., Oppo, D., Kleiven, H., Darling, K.F., & Kissel, C. (2012). Rapid switches in subpolar North Atlantic hydrography and climate during the Last Interglacial (MIS 5e. Paleoceanography, 27(2), N/a.

Irvalı, N., Ninnemann, U., Kleiven, H., Galaasen, E., Morley, A., & Rosenthal, Y. (2016). Evidence for regional cooling, frontal advances, and East Greenland Ice Sheet changes during the demise of the last interglacial. Quaternary Science Reviews, 150, 184. IPCC, 2013: Summary for Policymakers. In: *Climate Change 2013: The Physical Science Basis. Contribution of Working Group I to the Fifth Assessment Report of the Intergovernmental Panel on Climate Change* [Stocker, T.F., D. Qin, G.-K. Plattner, M. Tignor, S.K. Allen, J. Boschung, A. Nauels, Y. Xia, V. Bex and P.M. Midgley (eds.)]. Cambridge University Press, Cambridge, United Kingdom and New York, NY, USA, pp. 1–30.

Keigwin, L.D., Curry, W.B., Lehman, S.J., & Johnsen, S. (1994). The role of the deep ocean in North Atlantic climate change between 70 and 130 kyr ago. Nature, 371(6495), 323.

Keigwin, L.D., & Lehman, S.J. (1994). Deep circulation change linked to HEINRICH Event 1 and Younger Dryas in a middepth North Atlantic Core. Paleoceanography, 9(2), 185-194.

Kerr, R. (2000). A North Atlantic climate pacemaker for the centuries. Science, 288(5473), 1984-1986.

Kleiven, H., Kissel, C., Laj, C., Ninnemann, U., Richter, T., & Cortijo, E. (2008). Reduced North Atlantic deep water coeval with the glacial Lake Agassiz freshwater outburst. Science (New York, N.Y.), 319(5859), 60-4.

Knight, J., Allan, R., Folland, C., Vellinga, M., & Mann, M. (2005). A signature of persistent natural thermohaline circulation cycles in observed climate. Geophysical Research Letters, 32(20).

Köhl, A., Stammer, D., & Cornuelle, B. (2007). Interannual to Decadal Changes in the ECCO Global Synthesis. Journal of Physical Oceanography, 37(2), 313-337.

Kuhlbrodt, T., Griesel, A., Montoya, M., Levermann, A., Hofmann, M., & Rahmstorf, S. (2007). On the driving processes of the Atlantic meridional overturning circulation. Reviews of Geophysics, *45*(2).

Kuhs, M., Austin, W., Abbott, P., Hodell, D., Davies, S. M., Pearce, N. J. G., & Wastegard, S. (2014). Iceberg-rafted tephra as a potential tool for the reconstruction of ice-sheet processes and ocean surface circulation in the glacial North Atlantic. Special Publication - Geological Society of London, 398(1), 141-155.

Langehaug, H., Mjell, T., Otterå, O., Eldevik, T., Ninnemann, U., & Kleiven, H. (2016). On the reconstruction of ocean circulation and climate based on the "Gardar Drift". Paleoceanography, 31(3), 399-415.

Lohmann, K., Mignot, J., Langehaug, H., Jungclaus, J., Matei, D., Otterå, O., Gao, Y.Q., Mjell, T.L., Ninnemann, U.S., & Kleiven, H. (2014). Using simulations of the last millennium to understand climate variability seen in paleo-observations: Similar variation of Iceland-Scotland overflow strength and Atlantic Multidecadal Oscillation. Climate of the Past Discussions, 10(4), 3255-3302.

Lynch-Stieglitz, J. (2017). The Atlantic Meridional Overturning Circulation and Abrupt Climate Change. Annual Review of Marine Science, 9(1), 83-104.

Marshall, J., & Schott, F. (1999). Open-ocean convection: Observations, theory, and models. Reviews of Geophysics, 37(1), 1-64.

Manighetti, B. & McCave, I.N. (1995a). Late Glacial and Holocene palaeocurrents around Rockall Bank, NE Atlantic Ocean. Paleoceanography, 10(3), 611-626.

Manighetti, B. & McCave, I.N. (1995b). Depositional fluxes, palaeoproductivity, and ice rafting in the NE Atlantic over the past 30 ka. Paleoceanography, 10(3), 579-592.

Maslin, M., & Tzedakis, C. (1996). Sultry last interglacial gets sudden chill. Eos, Transactions American Geophysical Union, 77(37), 353-354.

McCave, I.N. (2008). Size sorting during transport and deposition of fine sediments: sortable silt and flow speed. In: Rebesco, M., Camerlenghi, A. (Eds.) Contourites. Elsevier, Amsterdam, pp. 121-142.

McCave, I.N., & Hall, I.R. (2006). Size sorting in marine muds: Processes, pitfalls, and prospects for paleoflow-speed proxies. Geochemistry, Geophysics, Geosystems G³., 7(10).

McCave, I.N., Manighetti, B., & Robinson, G. (1995). Sortable silt and fine sediment size/composition slicing: Parameters for palaeocurrent speed and palaeoceanography. Paleoceanography, 10(3), 593-610.

McCave, I.N., Thornalley, D.J.R., & Hall, I.R. (2017). Relation of sortable silt grain-size to deep-sea current speeds: Calibration of the 'Mud Current Meter'. Deep-Sea Research Part I, 127, 1-12.

McManus, J.F., Bond, G.C., Broecker, W.S., Johnsen, S., Labeyrie, L., & Higgins, S. (1994). High-resolution climate records from the North Atlantic during the last interglacial. Nature, 371(6495), 326-329.

McManus, J.F., Francois, R., Gherardi, J.-M., Keigwin, L.D., & Brown-Leger, S. (2004). Collapse and rapid resumption of Atlantic meridional circulation linked to deglacial climate changes. Nature, 428(6985), 834-837.

Minth, E.K. (2009). *Multi-species stable isotope analysis of floraminifera at Site U1304 (Gardar Drift, North Atlantic) before, during, and after the last interglacial*. (Unpublished master's thesis). University of Florida. Gainesville, FL.

Mjell, T., Ninnemann, U., Eldevik, T., & Kleiven, H. (2015). Holocene multidecadal- to millennial-scale variations in Iceland-Scotland overflow and their relationship to climate. Paleoceanography, 30(5), 558-569.

Mjell, T., Ninnemann, U., Kleiven, H., & Hall, I. (2016). Multidecadal changes in Iceland Scotland Overflow Water vigor over the last 600 years and its relationship to climate. Geophysical Research Letters, 43(5), 2111-2117.

Moffa-Sanchez, P., Hall, I.R., Thornally, D.J.R., & Barker, S. (2015). Changes in the strength of the Nordic Seas Overflows over the past 3000 years. *Quaternary Science Reviews* 123, 134-143.

NEEM community members. (2013). Eemian interglacial reconstructed from a Greenland folded ice core. Nature, 493, 489-494.

North Greenland Ice Core Project Members. (2004). High-resolution record of Northern Hemisphere climate extending into the last interglacial period. Nature, 431(7005), 147-151.

Oppo, D., & Lehman, S. (1993). Mid-depth circulation of the subpolar North Atlantic during the last glacial maximum. Science, 259(5098), 1148-1152.

Oppo, D., and Curry, W.B. (2011). Deep Atlantic Circulation During the Last Glacial Maximum and Deglaciation. Unpublished manuscript.

Oppo, D., Horowitz, M., & Lehman, S. (1997). Marine core evidence for reduced deep water production during Termination II followed by a relatively stable substage 5e (Eemian. Paleoceanography, 12(1), 51-63.

Oppo, D., McManus, J., & Cullen, J. (2006). Evolution and demise of the Last Interglacial warmth in the subpolar North Atlantic. Quaternary Science Reviews, 25(23), 3268-3277.

Otto-Bliesner, B., Marshall, S., Overpeck, J., Miller, G., & Hu, A. (2006). Simulating Arctic climate warmth and icefield retreat in the last interglaciation. Science (New York, N.Y.), 311(5768), 1751-3.

Praetorius, S.K., McManus, J.F., Oppo, D.W., & Curry, W.B. (2008). Episodic reductions in bottom-water currents since the last ice age. Nature Geoscience, 1(7), 449-452.

Rahmstorf, S., (2006). Thermohaline Ocean Circulation. In: Encyclopedia of Quaternary Sciences, Edited by S. A. Elias. Elsevier, Amsterdam.

Rasmussen, T., Thomsen, E., Kuijpers, A., & Wastegård, S. (2003). Late warming and early cooling of the sea surface in the Nordic seas during MIS 5e (Eemian Interglacial). Quaternary Science Reviews, 22(8-9), 809-821.

Reid, J. (1994). On the total geostrophic circulation of the North Atlantic Ocean: Flow patterns, tracers, and transports. Progress in Oceanography, 33(1), 1-92.

Ruddiman, W. (1977). Late Quaternary deposition of ice-rafted sand in the subpolar North Atlantic (lat 40° to 65°N). Geological Society of America Bulletin, 88(12), 1813-1827.

Sanchez Goni, M., Bakker, P., Desprat, S., Carlson, A.E., Van Meerbeeck, C.J., Peyron, O., Naughton, F., Fletcher, W., Eynaud, F., Rossignol, L., & Renssen, H. (2012). European climate optimum and enhanced Greenland melt during the Last Interglacial. Geology, 40(7), 627-630.

Sarnthein, M., Winn, K., Jung, S.J.A., Duplessy, J.-C., Labeyrie, L., Erlenkeuser, H., & Ganssen, G. (1994). Changes in East Atlantic Deepwater Circulation over the last 30,000 years: Eight time slice reconstructions. Paleoceanography, 9(2), 209-267.

Skinner, L.C., & Shackleton, N.J. (2006). Deconstructing Terminations I and II: Revisiting the glacioeustatic paradigm based on deep-water temperature estimates. Quaternary Science Reviews, 25(23), 3312-3321.

Shackleton, N.J., Chapman, M., Sánchez-Goñi, M.F., Pailler, D., & Lancelot, Y. (2002). The Classic Marine Isotope Substage 5e. Quaternary Research, 58(1), 14-16.

Shackleton, N.J., Sánchez-Goñi, M.F., Pailler, D., & Lancelot, Y. (2003). Marine Isotope Substage 5e and the Eemian Interglacial. Global and Planetary Change, 36(3), 151-155.

Shimada, C., Sato, T., Toyoshima, S., Yamasaki, M., & Tanimura, Y. (2008). Paleoecological significance of laminated diatomaceous oozes during the middle-to-late Pleistocene, North Atlantic Ocean (IODP Site U1304). Marine Micropaleontology, 69(2), 139-150.

Stocker, T., & Johnsen, S. (2003). A minimum thermodynamic model for the bipolar seesaw. Paleoceanography, 18(4), N/a.

Stommel, H. (1961), Thermohaline Convection with Two Stable Regimes of Flow. Tellus, 13: 224-230.

Stow, D., Faugères, J., Howe, J., Pudsey, C., & Viana, A. (2002). Bottom currents, contourites and deep-sea sediment drifts: Current state-of-the-art. Geological Society, London, Memoirs, 22(1), 7-20.

Talley, L. (1996). North Atlantic circulation and variability, reviewed for the CNLS conference. Physica D: Nonlinear Phenomena, 98(2), 625-646.

Thornalley, D., Barker, S., Becker, J., Hall, I., & Knorr, G. (2013a). Abrupt changes in deep Atlantic circulation during the transition to full glacial conditions. Paleoceanography, 28(2), 253-262.

Thornalley, D.J.R., Blaschek, M., Davies, F.J., Praetorius, S., Oppo, D., McManus, J.F., Hall, I.R., Kleiven, H., Renssen, H., McCave, I.N. (2013b). Long-term variations in Iceland-Scotland overflow strength during the Holocene. *Clim.Past* 9 (5), 2073-2084.

Tzedakis, P., Drysdale, R., Margari, V., Skinner, L., Menviel, L., Rhodes, R., Taschetto, A.S., Hodell, D.A., Crowhurst, S.J., Hellstrom, J.C., Fallick, A.E., Grimalt, J.O., McManus, J.F., Martrat, B., Mokeddem, Z., Parrenin, F., Regattieri, E., Roe, K., & Zanchetta, G. (2018). Enhanced climate instability in the North Atlantic and southern Europe during the Last Interglacial. Nature Communications, 9(1), 4235.

Vallis, G. (2012). *Climate and the Oceans*. Princeton University Press.

Van Aken, H.M., & Becker, G. (1996). Hydrography and through-flow in the north-eastern North Atlantic Ocean: The NANSEN project. Progress in Oceanography, 38(4), 297-346.

Wold, C.N. (1994). Cenozoic sediment accumulation on drifts in the northern North Atlantic. Paleoceanography, 9(6), 917-941.

Xuan, C., Channell, J.E.T., & Hodell, D. (2016). Quaternary magnetic and oxygen isotope stratigraphy in diatom-rich sediments of the southern Gardar Drift (IODP Site U1304, North Atlantic). Quaternary Science Reviews, 142, 74-89.

Yu, L., Gao, Y., & Otterå, O. (2016). The sensitivity of the Atlantic meridional overturning circulation to enhanced freshwater discharge along the entire, eastern and western coast of Greenland. Climate Dynamics, 46(5), 1351-1369.

APPENDIX A: Raw data

Table A.1: Mean sortable silt measurements. The number reported here is the mean value of the differential volume of all particles counted for each run. Extra runs were carried out for samples where precision within the sample replicates was poor. The final column is the mean value of all runs in the sample.

mcd	Interval	Run 1	Run 2	Run 3	Run 4	Run 5	Run 6	Mean
15.50	Late plateau/	22.29	22.75	22.06	22.30			22.35
15.90	glacial inception		18.25	18.71	18.33			18.43
16.30		25.16	25.96	25.47				25.53
16.70		26.66	27.11	26.91				26.89
17.10		20.14	19.19	19.45				19.59
17.50		25.95	25.84	24.91				25.57
17.80		24.87	24.42	24.38				24.56
18.10		26.31	24.90	25.18				25.46
18.50		20.32	19.82	19.53				19.89
18.90		16.89	17.80	17.86	17.50			17.51
19.30	Early- to	16.52	16.42	16.96				16.63
19.34	mid-plateau	18.60	18.83	19.70				19.04
19.38		18.65	18.47	20.06	20.57			19.44
19.42		17.46	17.62	17.63				17.57
19.46		15.71	15.77	15.64				15.71
19.50		16.07	18.34	16.72	16.66			16.95
19.54		16.09	17.14	16.83	17.07			16.78
19.58		16.48	16.90	16.84				16.74
19.62		16.69	16.20	16.59				16.49
19.66		17.20	16.75	17.60				17.18
19.70		22.98	22.23	22.31				22.51
19.74		21.65	21.95	22.58				22.06
19.78		17.27	17.46	18.24				17.65
19.82		21.20	21.96	20.65				21.27
19.86		22.98	21.88	22.40				22.42
19.90		19.05	20.79	20.58	20.50			20.23
19.94		16.16	15.77	16.23				16.06
19.98		17.22	18.22	17.67				17.70
20.02		21.16	21.16	21.54				21.29
20.06		17.59	17.55	17.24				17.46
20.10		21.35	20.44	20.41	20.88			20.77
20.14		19.56	21.17	18.56	18.58			19.47
20.18		18.29	18.86	18.06				18.40
20.22		17.72	18.06	18.62				18.13

20.26		16.57	16.49	17.89	16.92			16.97
20.30		19.79	18.76	18.48				19.01
20.34		16.99	18.05	17.19	17.10			17.33
20.38		19.72	19.11	20.01				19.61
20.42		17.94	18.15	16.65	16.82			17.39
20.46		19.11	20.14	20.80	21.09			20.29
20.50		19.47	18.53	18.71				18.90
20.54		15.86	16.71	15.68	17.83			16.52
20.58		18.18	17.36	18.12				17.88
20.62		19.06	19.92	18.98				19.32
20.66		17.04	17.01	18.51	17.37			17.48
20.70		18.49	16.98	16.21	17.43	17.61	18.29	17.50
20.74		18.72	17.31	17.39				17.81
20.78		18.46	18.65	18.93				18.68
20.82		17.90	18.18	18.01				18.03
20.86		18.61	18.49	18.18				18.43
20.90		16.87	16.38	16.39				16.55
20.94		18.93	17.37	17.65	17.18			17.78
20.98		18.74	17.27	17.04				17.68
21.02		17.48	17.62	18.02				17.70
21.06		16.80	17.89	19.28	17.66			17.91
21.10		17.69	17.28	17.89				17.62
21.14		16.96	18.30	16.78	16.20			17.06
21.18		16.92	16.74	17.17				16.94
21.22		18.59	18.44	18.31				18.44
21.26		20.06	19.46	19.50				19.67
21.30		20.42	20.46	19.93				20.27
21.34		19.61	19.86	19.25				19.57
21.38		20.22	21.26	20.18				20.55
21.42		21.42	21.30	21.46				21.39
21.46		18.35	18.98	19.36				18.90
21.50		22.26	21.13	20.85				21.41
21.54		22.87	23.03	22.87				22.92
21.58		20.42	20.18	21.10				20.57
21.62		21.49	21.00	21.17				21.22
21.66		22.00	21.66	21.68				21.78
21.70		21.81	21.94	21.03				21.59
21.74		21.46	22.17	22.36				21.99
21.78		21.17	21.13	20.95				21.08
21.82		21.32	20.12	20.26				20.57
21.86		22.18	21.92	22.25				22.12
21.90		22.39	21.71	22.68				22.26

21.94		21.73	21.48	20.56				21.26
21.98		20.43	19.68	21.37	20.11			20.40
22.02		19.90	21.51	21.27	21.15			20.96
22.06		24.27	20.48	22.21				22.32
22.10		22.77	21.57	22.93	22.64			22.48
22.14		23.23	23.60	23.65	25.35			23.96
22.18		20.24	23.14	21.45	20.79			21.40
22.22		20.90	22.00	23.24	23.41			22.39
22.26		20.14	19.70	23.45	23.62			21.73
22.30		23.81	23.66	22.77				23.41
22.34		21.06	22.84	23.50				22.47
22.38		22.91	23.04	22.65	23.41	22.90		23.00
22.42		22.84	24.12	24.46				23.81
22.46			26.25	24.52	24.74			25.17
22.50		23.01	23.26	22.88				23.05
22.54		24.05	22.62	23.91	24.05			23.66
22.57	Late glacial/	24.84	25.46	23.16	22.98			24.11
22.79	deglaciation	21.74	22.37	22.63				22.25
23.01		21.73	22.63	22.52	22.72			22.40
23.23		22.33	20.47	22.35	23.21			22.09

APPENDIX B: Statistics

The standard deviation (STD) for the complete mean sortable silt data set was calculated using equation B.1.

$$STD = \sqrt{\frac{\sum(\bar{x} - x)^2}{N - k}}$$

Where, $\bar{x}$ is the mean value of all replicates in the interval, x is the value of each individual measurement, N is the total number of replicates (here N = 321), and k is the number of intervals with replicates (here k = 96).

The standard error of the mean (SEM) was calculated using equation B.2.

$$SEM = \frac{STD}{\sqrt{n}}$$

Where n is the number of replicates per interval. Here SEM was calculated with n = 3 since every interval has a minimum of 3 replicates included in the mean.

Thus, the standard deviation for the mean sortable silt data set is ±0.71 μm, and the standard error of the mean for the data set is ±0.41 μm.